

Designing stimuli-responsive materials via architectural anisotropy

Zur Erlangung des akademischen Grades einer
DOKTORIN DER INGENIEURWISSENSCHAFTEN (DR.-ING.)

von der KIT-Fakultät für Chemieingenieurwesen und Verfahrenstechnik
des
Karlsruher Instituts für Technologie (KIT)

genehmigte
DISSERTATION

von
M. Sc. Katharina Cu
aus Coesfeld

Erstgutachter: Prof. Dr.-Ing. Matthias Franzreb

Zweitgutachter: Prof. Dr. Jörg Lahann

Tag der mündlichen Prüfung: 29.06.2023

Dedication

I dedicate this thesis to my mum, dad, and sister. There are no words, which can nearly describe my gratitude towards you. I owe everything to you because you always believed in me and supported me in every possible way. You have taught me to be humble, to never give up, and to always work hard.

Mami, Daddy, you both came as immigrants to Germany without knowing one single word of German, and without knowing anyone. In a foreign country and as teenagers, you learned the language, pursued education, and built a home for us. Your hard work, bravery, and sacrifice allowed us to pursue our dreams. I was and am lucky to have a family that always supported me in everything I did, such as my multiple moves to the Netherlands or the US.

姐姐, you have paved the way for me in so many ways. As the oldest child, you had to figure things out first regarding school, university, and jobs. As younger sister, I could always ask for your advice, rely on your experience, and look up to you.

I love you all so much and thank you for your unconditional love and support!

Acknowledgements

First and foremost, I would like to thank my advisor Prof. Dr. Jörg Lahann, for giving me the opportunity to join his lab and become a part of his academic family. In 2018, I was doing my internship in Boston and would never have thought to meet my future Ph.D. advisor there. I attended his guest lecture and was instantly amazed by all the science his lab was working on. I am grateful to have worked with him, as he constantly pushed me to my limits to exceed them whenever I felt like I could not. He taught me to think outside the box to approach and execute new projects. His humble character, sharp wit, and scientific experience made me a better scientist.

During my Ph.D. I have been very fortunate to have two advisors. Therefore, I would also like to thank Prof. Dr. Matthias Franzreb, who adopted me into his academic family and group. He is one of the humblest people I got to work with and was always approachable whenever I needed advice or help, especially during the last stretch of my Ph.D. studies. Also, I will never forget the Palmspring seminars, filled with science, fun, and sore muscles from the hikes.

This work would not have been possible without the help of my collaborators. Therefore, I want to thank Dr. Stefan Heißler for performing Raman spectroscopy, Dr. Matthias Schowtzer, who taught and helped me with SEM, Bianca Posselt and Dr. Erik Strandberg for performing CD measurements, and Valentin Tschan and Dr. Klaus-Peter Weiss for helping and supporting me with the tensile tests of the silk fibers. Further, I want to thank Jonas Kaltenbach and Dr. Julia Süßmuth for their help and insights working with graphene and Frank Kirschhöfer for helping me in the analytics. I also want to acknowledge my students for their dedicated work and Sefkan Kendir, who always ensured a constant supply of 3D-printed frames for the PEGDA project, which I worked on with Marvin

Klaiber, who has been a great collaborator and friend. From the start of my Ph.D., Marvin always tried to help and troubleshoot with me even when he was busy. Writing our dissertations and going through this period together made the last stretch and writing way more fun and less lonely. Our walks and ramen lunches energized me for the next writing sessions, and I cannot wait to finish the remaining ramen! I also want to thank colleagues and lab members from the German and US side for making this a memorable journey and for all their constructive feedback and insightful discussions, especially Dr. Jeffery Raymond, whose knowledge of everything helped and guided me through my projects. Dr. Anvay Ukidve has also been a great contributor to this work and a friend through his insights and experience. I thank him for his patience and friendship, which kept me sane in many situations, and made me laugh. Further, I want to thank my former advisors and mentors, Prof. Samir Mitragotri and Prof. David Fernandez Rivas, for their continued mentoring and guidance whenever needed.

Lastly, special thanks go out to Dr. Angela Weiss, Astrid Biedermann, and Stefanie Sellheim-Ret for helping with all administrative matters at the Institute of Functional Interfaces (IFG).

Abstract

Stimuli-responsive materials have received significant interest for their ability to undergo a conformational change and alter their material properties in response to an applied stimulus. Poly(acrylic acid) (PAA), for instance, changes its molecular conformation when exposed to solutions of different pH influencing its mechanical properties, and swelling behavior. Fabricating stimuli-responsive materials, like PAA, with architectural inhomogeneities, opens up new opportunities to create material systems with enhanced or novel actuations.

This dissertation focuses on developing new stimuli-responsive materials by enabling actuation responses with the help of architectural anisotropy via electrohydrodynamic (EHD) co-jetting. The fabrication process further utilizes 3D jet writing of multicompartmental fibers, which allows for precise deposition in a controlled manner. Besides conventional grid-like scaffolds, more complex structures inspired by nature, can be fabricated and designed to guide the actuation. These controlled movements are attractive for various fields, which require fewer variables. Conventional microanalytical systems, for instance, suffer from mass transport limitations as their detectability and sensitivity highly rely on analyte diffusion within the sample. In this work, spiderweb-like scaffolds composed of bicompartmental PAA fibers were designed, which movement was triggered by a change in pH. The fibers draw their reconfigurability from their bicompartmental architecture. Upon exposure to neutral pH, both fiber compartments differentially swell and give rise to interfacial tension. This tension ultimately results in shape reconfiguration of the fiber network. The reconfigurable fiber network displays a 57-fold increase in analyte detectability and average transport efficiencies of $91.9 \pm 2.4\%$ of the placed microspheres, which mimic analyte. Moreover, this work demonstrated the ability of the reconfigurable network to successfully separate spheres with different surface properties with $95 \pm 3\%$ accuracy.

Similar to these PAA fibers, bicompartamental silk fibroin (SF)-graphene-nigrosine fibers were fabricated, which, in contrast, respond to light. The fibers, again, draw their reconfigurability from their bicompartamental architecture and move by a distance of 4.9- and 7.1-fold of their fiber diameter when triggered by NIR and green light, respectively.

Stretchable hydrogel scaffolds with various pore geometries for tissue engineering and vascularization were also investigated. Therefore, the 3D jet written scaffolds composed of poly(ethylene glycol diacrylate) (PEGDA) and PAA were characterized and tensile tested. Cell seeding of human adipose microvascular endothelial cells (HAMECs), and dental pulp stem cells (DPSCs) as support cells onto PEGDA-PAA scaffolds, showed a cell-friendly environment enabling further studies on vessel sprouting coupled with mechanical stimulation.

Overall, this work demonstrates unique material properties that can be influenced by chemical composition, anisotropic architecture, and environmental conditions. Especially combining materials with stimuli-responsive properties creates new materials with enhanced and novel actuations that have the potential to revolutionize a range of applications, from healthcare to energy to environmental monitoring.

Kurzzusammenfassung

Materialspezifische Eigenschaften charakterisieren und bestimmen die Reaktion der Materialien auf bestimmte Stimuli, beispielsweise bei erhöhter Temperatur oder basischem pH-Wert. Poly(acryl)säure (PAA) zum Beispiel ändert seine molekulare Konformation, wenn das PAA Lösungen mit unterschiedlichem pH-Wert ausgesetzt wird, was die mechanischen Eigenschaften und das Quellverhalten beeinflusst. Die Herstellung von stimulierend-responsiven Materialien wie PAA mit architektonischen Inhomogenitäten eröffnet neue Möglichkeiten, neue Materialsysteme mit ausgeprägteren Reaktionen oder neuartigen Funktionen zu schaffen.

In dieser Dissertation geht es um die Entwicklung neuer stimulierend-responsiver Materialien, die mit Hilfe architektonischer Inhomogenität, hergestellt mittels elektrohydrodynamisches (EHD) Co-Jettings, ihr Ansprechverhalten verbessern. Der Herstellungsprozess ermöglicht zudem das 3D Jet Writing der hergestellten Fasern, welches eine präzise und kontrollierte Faserablagerung ermöglicht. Neben konventionellen gitterartigen Gerüsten können auch komplexere, von der Natur inspirierte Strukturen hergestellt und zur Steuerung der Bewegung entworfen werden. Diese kontrollierten Bewegungen sind für verschiedene Bereiche attraktiv, wodurch die Variabilität verringert wird. Konventionelle mikroanalytische Systeme, beispielsweise, leiden unter den Einschränkungen des Massentransports, da ihre Nachweisbarkeit und Empfindlichkeit in hohem Maße von der Diffusion der Analyten in der Probe abhängen. In dieser Arbeit wurden spinnennetzartige Gerüste aus bikompartimentalen PAA-Fasern entwickelt, deren Bewegung durch eine pH-Änderung ausgelöst wurde. Die Fasern beziehen ihre Rekonfigurierbarkeit aus ihrer bikompartimentalen Architektur. Wenn PAA-Fasern einem neutralen pH-Wert ausgesetzt werden, quellen beide

Faserkompartimente unterschiedlich auf und erzeugen eine Grenzflächenspannung. Diese Spannung führt letztlich zu einer Rekonfiguration der Form des Fasernetzwerks. Das rekonfigurierbare Fasernetzwerk zeigt eine 57-fache Steigerung der Nachweisbarkeit von Analyten und eine durchschnittliche Transporteffizienz von $91,9 \pm 2,4$ % der platzierten Mikropartikeln, die den Analyten nachahmen. Darüber hinaus zeigte diese Arbeit die Fähigkeit des rekonfigurierbaren Netzwerks, Partikeln mit unterschiedlichen Oberflächeneigenschaften mit einer Genauigkeit von 95 ± 3 % zu trennen.

Ähnlich wie die PAA-Fasern wurden bikompartimentale Seidenfibroin (SF)-Graphen-Nigrosin-Fasern hergestellt, die auf Licht reagieren. Auch diese SF-Graphen-Nigrosin-Fasern beziehen ihre Rekonfigurierbarkeit aus der bikompartimentalen Architektur und bewegen sich um das 4,9- bzw. 7,1-fache ihres Faserdurchmessers, wenn die Fasern durch NIR- bzw. grünes Licht ausgelöst werden.

Es wurden auch dehnbare Hydrogelgerüste mit verschiedenen Porengeometrien für das Tissue Engineering und die Vaskularisierung untersucht. Zu diesem Zweck wurden die aus Poly(ethylenglycoldiacrylat) (PEGDA) und PAA bestehenden 3D-Gerüste charakterisiert und auf ihre Zugfestigkeit geprüft. Die Besiedlung mittels humaner mikrovaskulären Endothelzellen aus Fettgewebe (HAMECs) und Zahnmarkstammzellen (DPSCs) als Stützzellen auf PEGDA-PAA-Gerüste zeigte eine zellfreundliche Umgebung, die weitere Studien zur Gefäßaussprossung in Verbindung mit mechanischer Stimulation ermöglicht.

Insgesamt zeigt diese Arbeit die einzigartigen Eigenschaften von Materialien, die durch die chemische Zusammensetzung, die Struktur und die Umgebungsbedingungen, beeinflusst werden können. Insbesondere durch die Kombination mehrerer Materialien mit stimulierenden Eigenschaften entstehen neue Materialien mit verbesserten und

neuartigen Antrieben, die das Potenzial haben, eine Reihe von Anwendungen zu revolutionieren, von der Gesundheitsfürsorge über die Energieversorgung bis hin zur Umweltüberwachung.

List of Abbreviations

AR	Aspect Ratio
BMP-2	Bone morphogenetic protein-2
BmSF	Bombyx mori silk fibroin
CD	Circular dichroism
CLSM	Confocal laser scanning microscopy
CVD	Chemical vapor deposition
DA	Diversion Angle
DMOAP	Dimethyloctadecyl-[3-(trimethoxysilyl)-propyl]-ammoniumchlorid
DOX	Doxorubicin
DPSCs	Dental pulp stem cells
ECM	Extracellular matrix
ECs	Endothelial cells
EG	Ethylene glycol
EHD	Electrohydrodynamic
Ex/Em	Excitation/Emission
FITC	Fluorescein isothiocyanate
FWHM	Full width at half maximum
HA	Hyaluronic acid
HAMECs	Human adipose microvascular endothelial cells
hMSCs	Human mesenchymal stem cells
IR	Infrared
Irgacure 2959	2-hydroxy-4'-(2-hydroxyethoxy)-2-methylpropiophenone

KH₂PO₄	Monopotassium phosphate
LCST	Low critical solution temperature
LEDs	Light-emitting diodes
MB	Methylene blue
MG	Microgels
mPEG	Monofunctional Poly(ethylene glycol)
NaH₂PO₄	Monosodium phosphate
NH₂C(CH₂OH)₃	Trizma base
NIR	Near-infrared
NPs	Nanoparticles
PAA	Poly(acrylic acid)
PCL	Poly(caprolactone)
PDMS	Poly(dimethylsiloxane)
PEDOT:PSS	Poly(3,4-ethylenedioxythiophene)-poly(styrenesulfonate)
PEG	Poly(ethylene glycol)
PEGDA	Poly(ethylene glycol diacrylate)
PEO	Poly(ethylene oxide)
PHIS	Poly(L-histidine)
PLA	Poly(lactic acid)
PLGA	Poly(lactic-co-glycolic acid)
PLM	Polarized light microscopy
PMMA	Poly(methyl methacrylate)
pNIPAm-co-AAc	Poly(N-isopropylacrylamide)-co-acrylic acid
pNIPAm-co-APBA	Poly(N-isopropylacrylamide-3-(acrylamido)phenylboronic acid)

Poly(NIPAM-ABP)	Poly(N-isopropylacrylamide-co-4-acryloyl benzophenone)
PTFE	Polytetrafluoroethylene
PVCi	Poly(vinyl cinnamate)
RCF	Relative centrifugal force
ROI	Region of interest
RPM	Rounds per minute
SCs	Support Cells
SEM	Standard error of the mean
SF	Silk fibroin
UV	Ultraviolet
UV-Vis	Ultraviolet-Visible
v/v	Volume per volume
w/v	Weight per volume

List of Symbols

Latin Symbols

A	Surface area [m ²]
C	Circularity
c	Concentration [$\mu\text{g mL}^{-1}$]
<i>c_w</i>	Drag coefficient [-]
d	Diameter [m]
D	Distance to center [-]
DA	Diversion angle [°]
d_d	Fiber diameter dry state
d_s	Fiber diameter swollen state
E	Young's modulus [Pa]
F	Force [N]
<i>F_D</i>	Drag force [N]
<i>h</i>	Height [m]
I	Isotropy [-]
K	Curvature [$1 \mu\text{m}^{-1}$]
m	Mass [kg]
<i>M_w</i>	Molecular weight [g mol^{-1}]
P	Power [W]
Q	Swelling factor [-]
s	Distance [m]
t	Time [s]

T_g	Glass transition temperature
U	Voltage [V]
v	Velocity [m s^{-1}]
w	Width [m]
W	Work [N m]
x	Displacement [m]

Greek Symbols

γ	Electrical Conductivity [S cm^{-1}]
ε	(Bending) strain [-]
κ	Thermal conductivity [$\text{W m}^{-1} \text{K}^{-1}$]
λ	Wavelength [nm]
ρ	Density [kg m^{-3}]
σ	Stress [N m^{-2}]
τ	Time constant [s]

Contents

Dedication	I
Acknowledgements	II
Abstract.....	IV
Kurzzusammenfassung	VI
List of Abbreviations	IX
List of Symbols	XII
1. Introduction	1
2. Background.....	4
2.1. Electrohydrodynamic Co-Jetting and 3D Jet Writing.....	4
2.2. Stimuli-Responsive Materials and Systems.....	7
2.3. Stimuli and Materials Properties.....	10
2.4. Geometrical Anisotropy.....	13
2.5. Bio-inspired Materials Systems	17
2.6. Biomaterials	19
2.7. Tissue Engineering.....	21
2.8. Microanalytical Sensing Devices.....	23
2.9. Soft Robotics.....	25
2.10. Graphene and Its Derivatives.....	30
3. Materials and Methods	35
3.1. Chemicals.....	35
3.2. Instrumentation	36
3.3. Software	37
3.4. Polymeric solution for Electrohydrodynamic (Co-) Jet Writing	38
3.5. Optical Sample Analyses	39
3.6. Statistical Analysis.....	40
3.7. Electrohydrodynamic (Co-) Jet Writing of PAA	40
3.8. Swelling Properties of PAA fibers.....	41
3.9. Analyte Transport Experiment.....	42
3.10. Fluorescence Signal and Enhancement Factor.....	43
3.11. Fiber Force Measurement	44
3.12. Diversion Angle & Isotropy.....	46
3.13. Electrohydrodynamic Jet Writing of PEGDA-PAA Scaffolds	46
3.14. Scaffold Characterization.....	47
3.15. Tensile Tests of PEGDA-PAA Scaffolds	47
3.16. Pore Analysis	48
3.17. Electrohydrodynamic Jet Writing of SF Fibers	48
3.18. Raman Spectroscopy.....	49
3.19. Ultraviolet-Visible (UV-Vis) Spectroscopy.....	49
3.20. CD Spectroscopy.....	49
3.21. Tensile Tests of SF Fibers.....	50
3.22. Light-Triggered Actuation of SF Fibers	50

4.	Results and Discussion.....	51
4.1.	Biomimetic PAA Hydrogel Scaffold for Directed Transport.....	52
4.1.1.	Fabrication of Bicompartamental PAA-Fibers.....	53
4.1.2.	Swelling Characteristics.....	55
4.1.3.	Directed Particle Transport.....	61
4.1.4.	Isotropy and Diversion Angle.....	68
4.1.5.	Enhanced Fluorescence Signal.....	70
4.1.6.	Selectivity.....	73
4.1.7.	Biological Application of PAA-Scaffolds.....	75
4.2.	Stretchable Hydrogel Scaffolds for Vascular Tissue Engineering.....	78
4.2.1.	Fabrication of PEGDA-PAA Hydrogel Scaffolds.....	79
4.2.2.	Characterization of Scaffold Geometries.....	80
4.2.3.	Tensile Tests of PEGDA-PAA Scaffolds.....	86
4.2.4.	Cell Culture.....	90
4.3.	EHD Jetting of SF-Graphene Fibers.....	93
4.3.1.	SF Concentration for EHD Jetting.....	94
4.3.2.	Characterization of SF Fibers.....	98
4.3.3.	Pre-Treatment of Graphene.....	102
4.3.4.	Fabrication of Bicompartamental SF-Graphene Fibers.....	106
4.3.5.	Mechanical Tests of SF-Graphene Fibers.....	109
4.3.6.	Light-Triggered Actuation.....	112
5.	Conclusion and Outlook.....	120
	List of Tables.....	124
	List of Figures.....	125
	References.....	128
	Supporting Information.....	150
	Publications.....	151

1. Introduction

Over the last decades, stimuli-responsive materials have emerged as a novel and disruptive innovation in diverse fields, such as medicine,^[11] materials science,^[12] and nanotechnology.^[13] Stimuli-responsive systems are designed to undergo chemical or physical changes, which can alter their properties in response to an applied stimulus. Such stimuli can include but are not limited to light,^[14] pH,^[15] temperature,^[8, 16] and electric^[17] or magnetic fields^[18]. The number of stimuli one system can respond to can also vary, as stimuli-responsive systems can be designed to respond to multiple stimuli, also known as multi-stimuli-responsive materials.^[19] Their ability to sense and respond to a specific stimulus is the reason why these systems are considered ‘smart’ and provide a new level of control over materials and their properties. This level of control is especially attractive for applications where controlled behavior and functionalization is required. In the medical field, for instance, many patients suffer from side-effects when taking medications, as their release is non-specific.^[20] Chemotherapy drugs are especially detrimental since healthy cells and tissues can be damaged as well since the drug does not differentiate between malignant and benign.^[21] More conventional drugs, like antibiotics, also suffer from this non-specific release in form of gastrointestinal problems or other complications.^[22] Stimuli-responsive systems offer a potential solution to these challenges by providing targeted and controlled drug delivery. Releasing its cargo in a desired location and at a desired time triggered by the pH of gastric acid, for instance, significantly reduces side-effects and improves patient compliance.^[23]

In soft robotics, stimuli-responsive systems are utilized as actuators that often mimic the movements and flexibility of systems in nature.^[24] Hydrogels, for instance, are frequently used as material for soft actuators, as they can be easily tuned and functionalized to respond

to changes in pH, temperature, or light.^[25] These soft actuators are often presented in the form of soft grippers,^[26] soft swimmers,^[27] or moving robots,^[28] which undergo shape reconfigurations. Camouflage swimmers, for instance, are autonomously propelled swimmers that mimic animal camouflage strategies in response to a certain pH, temperature, and light. Innovations like these, inspired by nature, present a significant step toward the next generation of smart robotics and many other fields.^[29] Unlike conventional robotics, soft robots consist of pliable materials, like rubber, silicone, or polymers, which make their applications safer, more flexible, and more adaptable. Especially for medical applications, soft robots are superior compared to the conventional ones as tasks can be executed with or on soft tissues and organs without causing any harm. Malachowski et al., for example, have developed thermo-responsive grippers, which can harmlessly dig into the tissue and secure the position of the grippers for drug delivery purposes.^[30]

Tissue engineering, for instance, has experienced a significant impact by bio-inspired and stimuli-responsive materials and systems.^[20a, 31] These smart materials can mimic the extracellular matrix and release growth factors or other bioactive molecules upon a certain trigger, like enzymes^[32], pH^[15a], or temperature^[33] to create a supportive environment, which facilitates and promotes cell growth and differentiation into specific tissues. Various materials, including biomaterials, such as silk fibroin (SF) have been explored as stimuli-responsive system. A semi-interpenetrating polymer network composed of chitosan crosslinked with glutaraldehyde, and SF, for instance, shows great potential as artificial muscle as its swelling and shrinking movements in response to a certain pH are reversible.^[34]

The main objective of this dissertation was to utilize electrohydrodynamic (EHD) (co)-jetting to create and synergize new materials for applications in the tissue engineering field, as well as present solutions to challenges currently faced in conventional approaches. Utilizing materials with different properties and combining them to induce a mechanical

mismatch via architectural inhomogeneity in form of bicompartmental fibers, enhanced actuations in response to pH, or light. The precise control of the fiber deposition via EHD jet writing, moreover, enabled the fabrication of complex geometries, which could control the actuation in a directed manner but also impact the fiber homogeneity and directionality within an entire scaffold. This geometrical impact was investigated for stretchable scaffolds and their applications in the tissue engineering field to study the mechanical impact on cell growth and vascularization.

2. Background

2.1. Electrohydrodynamic Co-Jetting and 3D Jet Writing

Over the last decades, electrohydrodynamic (EHD) co-jetting has emerged as a preferred technique to fabricate multifunctional particles and fibers in a micro- to nanoscale dimension.^[35] The functional versatility of the internal architecture due to its chemical as well as physical tunability^[36] have shown the technique's exceptional potential in various fields, such as sensors,^[37] printed electronics,^[38] filtrations^[39] and biotechnology.^[40] EHD jetting has especially opened up many opportunities for the biomedical field. The technique's applicability to many materials, for instance, has enabled the fabrication of entirely protein-based particles in the nanometer-range for the analysis of the penetration capabilities across the blood-brain-barrier.^[40-41]

In a typical EHD co-jetting setup, the jetting solutions are injected into parallelly arranged nozzles at low flow rates (**Figure 2-1**). Once a liquid meniscus forms at the nozzle tips, an electric potential is externally applied to the nozzles. The induced electric field

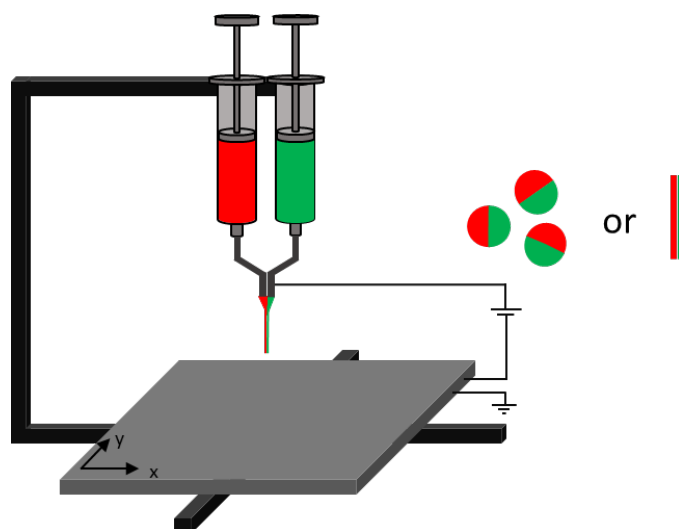


Figure 2-1: Schematics of the electrohydrodynamic (EHD) co-jetting process. The process enables the fabrication of particles or fibers via electrospaying or electrospinning respectively.

accumulates electric charges onto the meniscus surface. The coulombic repulsion between the electric charges deforms the meniscus into a conical shape, also known as Taylor cone. A thin and continuous jet is created that elongates towards the collector to fabricate fibers. The volatile components in the jetting solutions evaporate during the acceleration process towards the collector, resulting in micro- /nano-scale structures. Depending on the applied voltage, flow rate, and nozzle tip-to-collector distance, the jet can also be broken up into electrically charged droplets to form particles. Nanoparticles (NPs), generally in the size range of 1 – 1000 nm, have a large surface area to mass ratio. Their small size and high reactivity compared to bulkier structures of the same material, make them a popular platform in the biomedical field for sensing, imaging of living cells and tissues, and drug delivery.^[42] Especially for the latter, NPs have gained great interest as drug-loaded NPs can release their cargo at a sustained rate or in response to an environmental condition, which significantly reduces off-target toxicity and systemic side-effects.^[43] Another advantage of NPs for drug delivery is their prolonged systemic circulation time due to surface modifications.^[44] PEGylation, for instance is a process in which NPs are coated with poly(ethylene glycol) (PEG) to prevent their non-specific uptake by the reticuloendothelial system.^[45]

The phenomenon of an electrical discharge from liquids was first reported in 1914 by Zeleny.^[46] In the early days and prior to EHD jet writing, electrospinning was mainly used in the textile industry for fabricating non-woven fiber fabrics.^[47] Their high-surface-to-volume ratio and tunable porosity have quickly gained great interest in the tissue engineering field to fabricate nanofibrous scaffolds made of natural and synthetic polymers that mimic extracellular matrix components.^[48] Further applications within the biomedical field include wound dressings with antibacterial properties,^[49] and drug delivery platforms for the controlled release of various drugs such as paclitaxel^[50] and mefoxin.^[51] However, the lack of control over the fiber mat parameters, such as pore size, gave rise to the EHD jet. While

electrospun fiber mats are jetted in a rapid whipping manner of the polymer jet, EHD jetting creates a stable polymer jet. Mounting the grounded collector plate on a computer-assisted x-y stage, as seen in **Figure 2-1**, further allows a more controlled deposition of the fiber jet to create highly ordered scaffolds with various geometries and multiple layers (**Figure 2-2**).^[3] This modified electrojetting process is known as 3D jet writing, as three-dimensional structures with high precision can be fabricated.^[3] The control of the pore size is especially beneficial for the tissue engineering field as pores are crucial for nutrient and oxygen diffusion, as well as waste removal. Moreover, research has shown that pore size and shape significantly impact the cell interaction, migration, proliferation, and differentiation.^[52] Osteoblasts, for instance, show an enhanced cellular response to round pore shapes with diameters ranging from 200 – 400 μm .^[53] Eggli et al. reported a smaller amount of bone growth within the same scaffold material but with 50 – 100 μm diameter pores.^[54]

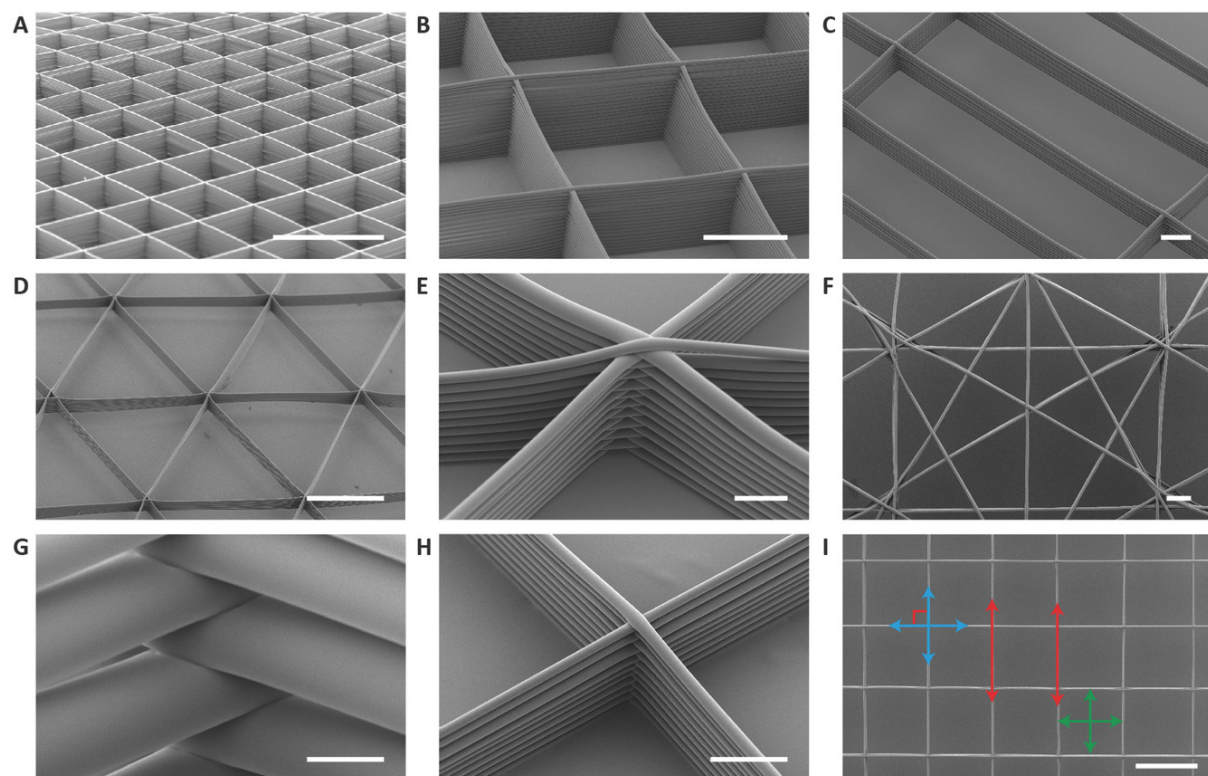


Figure 2-2: SEM images of different scaffold geometries fabricated via 3D jet writing.^[3]

2.2. Stimuli-Responsive Materials and Systems

Stimuli-responsive materials have emerged as attractive materials for their ability to undergo a conformational change and alter their material properties in response to an applied stimulus. Various stimuli such as pH,^[16a] temperature,^[55] electricity,^[56] light,^[14c] magnetic field,^[57] or solvents^[58] can be recognized by stimuli-responsive systems and trigger a response, which makes them also known as “smart” materials. Their versatility and tunability make them a desired tool for a wide range of applications. One of the most promising fields for stimuli-responsive systems is drug delivery. By designing drug delivery systems, which respond to specific stimuli, like pH^[59] or temperature^[16b, 16c], one can locally and timely control the drug release in the body. A pH-responsive system, for instance, can detect and respond to the stomach with its specific pH level by releasing its cargo.^[15d, 23] This controlled release

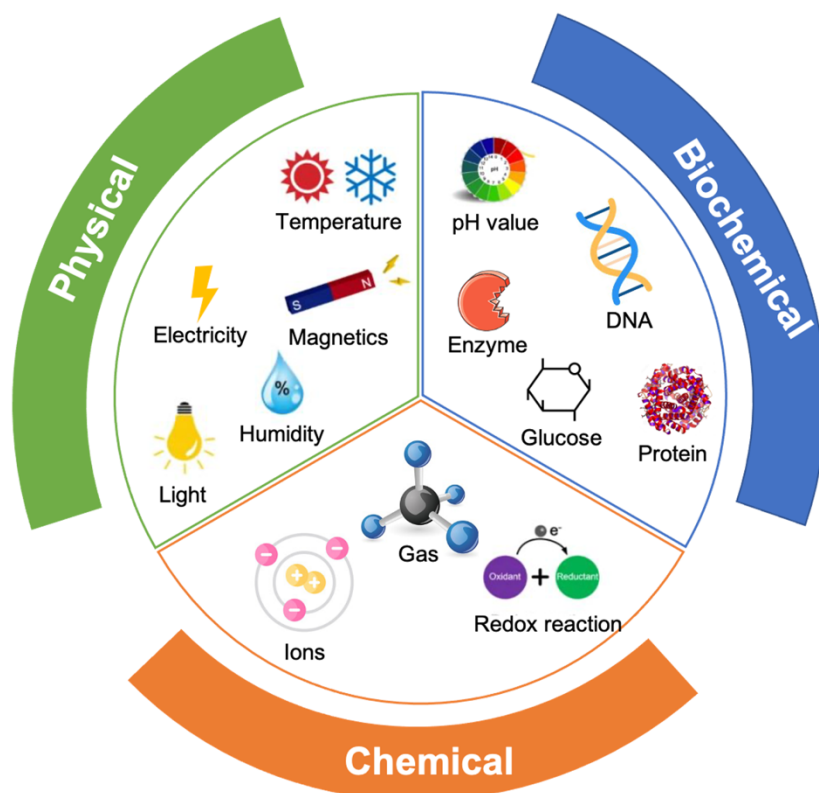


Figure 2-3: Overview of biochemical, chemical and physical stimuli.

significantly increases the delivery efficiency, which reduces off-target delivery and side-effects.^[15c, 60] Other possible applications are within the field of electronics,^[61] as sensors, switches^[62] or other electronic components.^[63] A change in temperature, for instance, can trigger an electronic response.^[64] Overall, stimuli-responsive systems show great potential for a wide range of applications across various fields, as they create new and innovative solutions to challenges, from drug delivery to materials science and electronics.^[65]

Multiple factors need to be considered when designing a stimuli-responsive system. First, the stimulus that triggers the system. In general, all stimuli can be classified into three categories: biochemical, chemical, and physical stimuli (**Figure 2-3**). Second, materials that are suitable for the application in terms of compatibility, magnitude, and speed of the response and, in some cases, reversibility of the actuation. Therefore, depending on the stimulus that triggers the system, materials can be chosen based on their chemistry, like molecular weight, and properties. And finally, the architectural design of the system, as the layout and arrangement of components, can affect the system's performance in terms of magnitude and response time. For mechanical actuations and shape reconfigurability, in which a physical change is induced, geometrical inhomogeneity can support and enhance the effect. **Table 2-1** is a subset of the broad literature on stimuli-responsive materials and gives a glimpse of the versatility and application of those materials.

Table 2-1: Common stimuli and their applicational field

Application	Stimulus	Strategies and Results	Reference
(Bio)sensors	Temperature	pNIPAm-based material actuates between swollen and non-swollen state for rapid tuning of surface plasmon resonance (SPR).	[63]
		pNIPAm microgels collapse above LCST resulting in color change due to microgel solvation state modulated plasmon coupling between the gold nanoparticles (AuNPs).	[64]
	pH	Differently colored quantum dots anchored to single graphene oxide sheet via pH-responsive polymer linkers change conformation at distinct pH ranges resulting in a colorimetric change.	[65]
	CO₂	AuNPs coated with CO ₂ responsive polymer, poly(N-(3-amidino)-aniline) (PNAAN), a CO ₂ responsive polymer, coated to AuNPs, swells and detaches from AuNPs upon CO ₂ trigger resulting in AuNP aggregation and color change.	[66]
	Glucose	Hydrogel microbeads contained glucose-responsive fluorescent dye monomer, which diboronic acid moiety preferably binds to the hydroxyl groups of glucose, switching on the fluorescence.	[67]
Drug Delivery	Light	Microneedles (MNs) loaded with ibuprofen included light-responsive 3,5-dimethoxybenzoin conjugate for on-demand release.	[68]
		Near-infrared light-activatable MNs heat tumor and induce thermal ablation for photothermal therapy. The poly(caprolactone) MNs then melt to release doxorubicin for chemotherapy.	[12b]
	pH	Controlled drug release via chemically-modified hydrogels, which enable the ionization at different pH.	[69]
	Glucose	Hypoxia	Hypoxia-sensitive hyaluronic acid (HS-HA) conjugated with hydrophobic 2-nitroimidazole converts to hydrophilic 2-aminoimidazoles and release insulin in a hyperglycemic environment
Mechanical actuators	Humidity	Bilayer actuators as reversible humidity-responsive actuation. Water has a higher affinity to graphene oxide (GO) on one side than the partially reduced graphene oxide–polypyrrole (prGO-PPy) on the other side.	[71]
	Light	Liquid crystalline polymers (LCPs) including azobenzene moieties undergo trans-/cis- isomerization upon (UV) light exposure.	[12d, 72]
	Temperature	Bilayer pattern and different thermal expansion coefficients induce bending motion.	[73]

2.3. Stimuli and Materials Properties

Materials are defined by their properties and determined by chemical composition, microstructure, and how a material is processed.^[66] A mechanical actuator, for instance, might require a flexible and elastic material. The elasticity can be influenced by the material's crystallinity, the strength of the bonds between atoms, and the arrangements of atoms themselves.^[67] Isomers, for instance, have the same chemical formula but differ in orientation or bonding sequence of their atoms and thus have different chemical and physical properties.^[68] The same applies to materials with the same chemical structure but different molecular weights. Polymers with high molecular weights are more viscous and have a higher melting point than polymers with lower molecular weights.^[69] Functional groups also influence material properties, such as their solubility, boiling, and melting point.^[70] They play an essential role in stimuli-responsive systems because these moieties are responsible for characteristic chemical reactions, which allow the system to respond to a stimulus.^[44b] Disulfides, for instance, can be used for drug delivery when the bond is chemically cleaved to release the linked cargo in an alkaline pH.^[71] Therefore, it is crucial to choose a suitable material and its properties based on the applied stimulus.

Glutathione, for instance, is one biochemical stimulus harnessed for solid tumor immunotherapy. Li et al. designed nano-micelles loaded with a photosensitizer, namely MeTTMN. The nano-micelles locally release their cargo in the presence of high glutathione concentrations in cancer cells. The disulfide bond is cleaved similarly to the depicted reaction shown in **Figure 2-4A**. Compared to photosensitizers remaining in the nano-micelle core, the released ones significantly improve the photodynamic therapy by generating more reactive oxygen species.^[72]

One of the most common chemical stimuli for triggered systems is pH. pH-responsive systems have revolutionized the field of drug delivery in particular as they can sense the pH

difference between malignant (6.5) and healthy tissues (~7.4) to prevent off-target toxicity, which is especially advantageous for delivering vaccine components.^[73] In the extracellular environment of solid tumors, for instance, rupturing hydrazone bonds or protonating amino groups can trigger a cargo release.^[15b] Liu et al. developed a dual pH-responsive multifunctional nanoparticle system with poly(L-histidine) (PHIS) and R848, an antitumor immune regulator, serving as the nanocore. The material property of PHIS changes from hydrophobic to hydrophilic as PHIS is ionized in an acidic environment causing the disintegration of the nanoparticle and subsequently the release of R848 to exert immunoregulatory activities. The outside coating of the nanocores consists of doxorubicin (DOX) conjugated to hyaluronic acid (HA) via an acid-cleavable hydrazone bond similarly seen in **Figure 2-4B**. The bond is cleaved after internalizing HA-DOX through CD44-mediated endocytosis at pH 5.5, causing the release of DOX to kill cancer cells for the chemotherapeutic part. The multifunctional nanoparticle system significantly inhibited the tumor growth of 4T1 tumor-bearing mice, demonstrating the synergy between immunotherapy and chemotherapy against breast cancer enabled by the pH-responsiveness.^[74] Ionizing hydrogels due to pH is another common drug delivery strategy using the chemical stimulus. Gao et al. designed microgels consisting of poly(N-isopropylacrylamide)-co-acrylic acid (pNIPAm-co-AAc), (AAc-MG), and poly(N-isopropylacrylamide-3-(acrylamido)phenylboronic acid) (pNIPAm-co-APBA), (APBA-MG).^[75] Here, AAc and APBA are the pH-responsive parts of the microgels. At a basic pH of pH 10, both microgels are negatively charged, while the model drug, methylene blue (MB), is positively charged and bound to both microgels due to strong electrostatic interactions resulting in the drug loading of the microgels. The pK_a of APBA is 8.4, meaning that at a pH below that value APBA will be neutrally charged. Due to the electrostatic repulsion, MB is released from APBA-MG, while still being bound to AAc-MG. Only at a pH below the pK_a

of AAc (pK_a 4.25), MB is fully released as AAc-MG is neutralized at that pH. Thus, the incorporation of polymers with different pK_a values enables the sequential and controlled release of drugs at physiologically relevant areas, such as tumor microenvironments to reduce ‘off-target’ toxicities, improve target accumulation, and lower the frequency of administration for a higher patient compliance.

Light is a physical stimulus, often harnessed for mechanical actuators, as seen in **Table 2-1**. Those photo-responsive systems often have azobenzene moieties incorporated into their polymer networks because of their reversibility and clean photochemistry. The first isomeric state of the azobenzene is the thermally stable trans configuration. Upon light exposure, the azobenzene absorbs a photon and isomerizes from the stable-trans to the meta-stable cis state (**Figure 2-4C**). This isomerization reverts to the stable-trans state when the cis

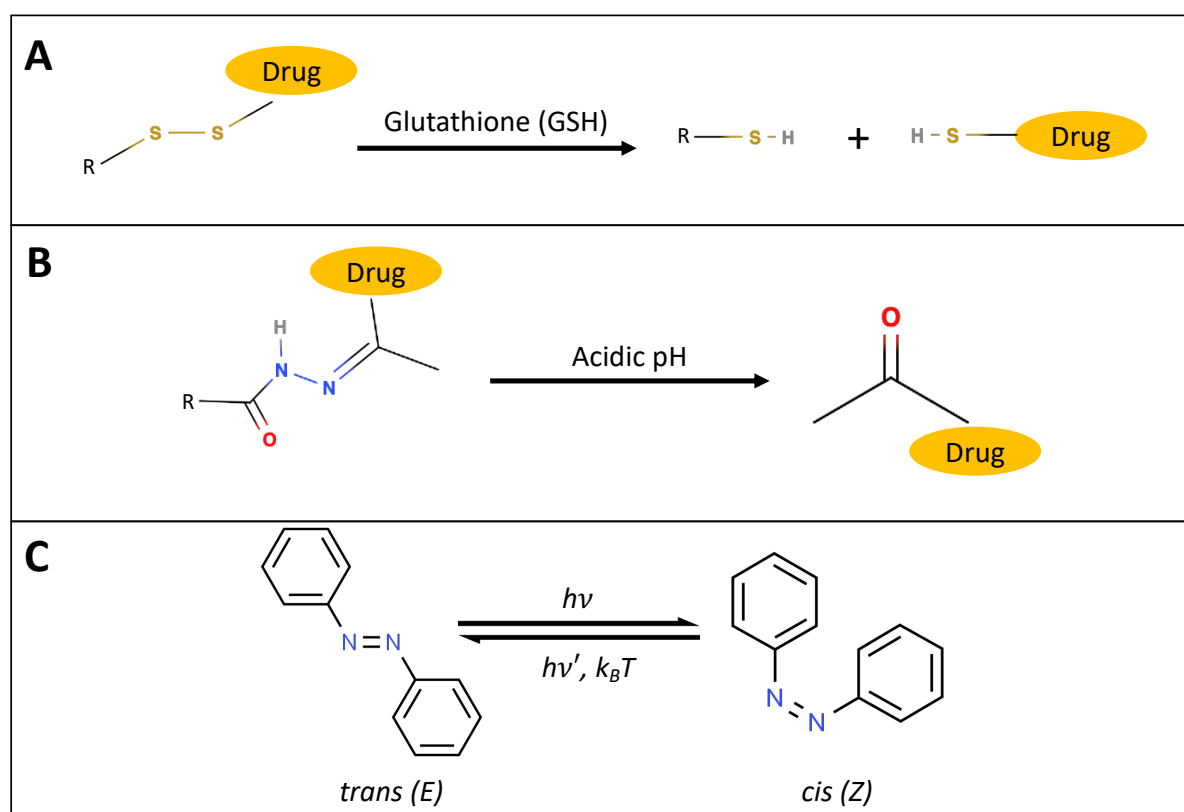


Figure 2-4: Conformational changes due to applied stimuli. A) Disulfide bond cleavage due to high glutathione concentration. B) pH-dependent hydrogel swelling. C) Azobenzene isomerization between stable trans and meta-stable cis state.

molecule thermally relaxes or if the light at a wavelength in the cis absorption band is applied.^[76] Ikeda and his co-workers, for instance, have developed liquid-crystal networks that contain the abovementioned azobenzene moieties and undergo trans-cis isomerization under irradiation.^[14d]

2.4. Geometrical Anisotropy

Architectural inhomogeneity combined with mechanical mismatches enhance the mechanical actuation or shape reconfigurability.^[8, 24b, 24c, 77] A mechanical mismatch can occur due to the usage of completely different or the same materials, which differ in one or more properties based on molecular weights, crosslinking, and crystallinity.^[78] The architectural inhomogeneity, on the other hand, is created through the fabrication in the forms of bilayer or patterned films,^[77d, 79] fibers,^[80] or particles^[81]. Lahann and his co-workers used EHD co-jetting to fabricate multicompartmental microcylinders, which can bend, toggle, or shapeshift into snail-like particles.^[9, 82] Therefore, they combined bicompartmental and core-shell arrangements with different polymers, such as poly(lactic-co-glycolic acid (PLGA) and poly(methyl methacrylate) (PMMA). The polymers were chosen based on their different glass transition temperature, at which the polymer transitions from a rigid to soft material. The T_g of PLGA (47–48°C) is nearly a 3-fold lower than the T_g of PMMA (115–116°C). The authors harness this difference in material property for an anisotropic actuation. For that, they apply ultrasound to heat the multicompartmental microcylinders. The temperature only exceeds the T_g of PLGA. Thus, only that compartment actuates while PMMA remains untriggered (**Figure 2-5A**). Another particle shape is created by simply decreasing the weight percentage of PMMA to one-tenth of its initial value, which lowers the particle's rigidity. As a result, the bending of the PLGA compartment increases. The authors demonstrated more shape reconfigurations that they describe as "bull-head" or "ring particles" by using materials

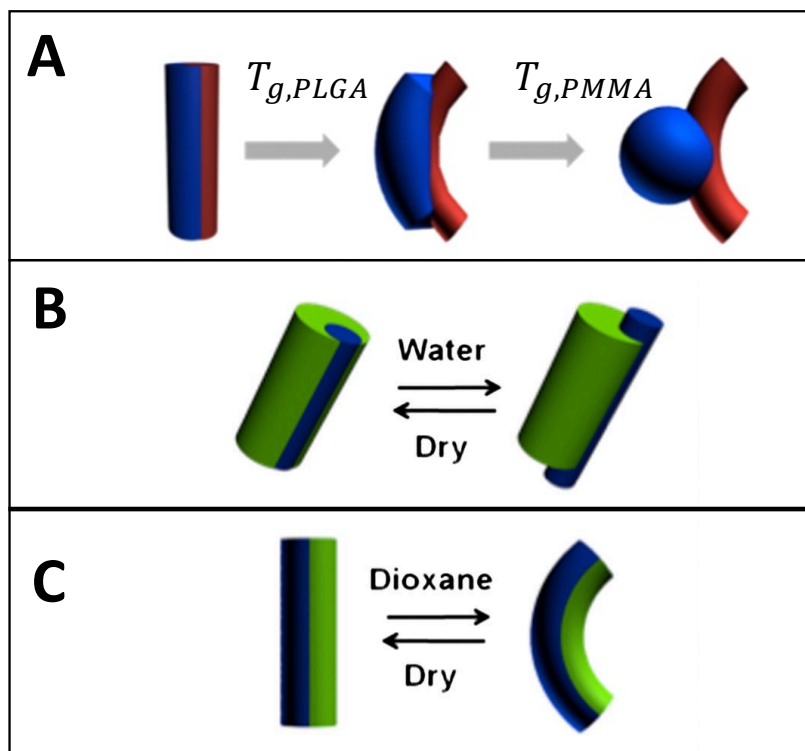


Figure 2-5: Anisotropic shape-shifting of multicompartamental microcylinders. **A)** Irreversible shape-shifting of PLGA/PMMA microcylinders due to heating. **B)** Reversible shape-shifting of Hydrogel/PLGA microcylinders due to swelling and deswelling depending on the water or dry state, respectively. **C)** Reversible shape-shifting of PEO/PVCi microcylinders due to swelling and deswelling depending on the dioxane or dry state, respectively. Figure adapted with permission from:^[9]

with distinct T_g . The reported systems triggered by temperature are non-reversible. For fully reversible actuation, the authors have substituted one polymer compartment with a hydrogel, which is water-responsive. Upon water exposure of those multicompartamental microcylinders, the hydrogel compartment swells by 280%, while the PLGA remains unchanged (**Figure 2-5B**). For bicompartamental microcylinders composed of poly(ethylene oxide) (PEO) and crosslinked poly(vinyl cinnamate) (PVCi), the immersion into dioxane results in reversible bending as PEO maintains its shape (**Figure 2-5C**). Based on the principle described above, Ionov and his co-workers have fabricated bilayered films made of a thermoresponsive polymer (**Figure 2-6**).^[8] The used polymer, poly(N-isopropylacrylamide-co-4-acryloyl benzophenone) (poly(NIPAM-ABP), changes its solubility at the low critical

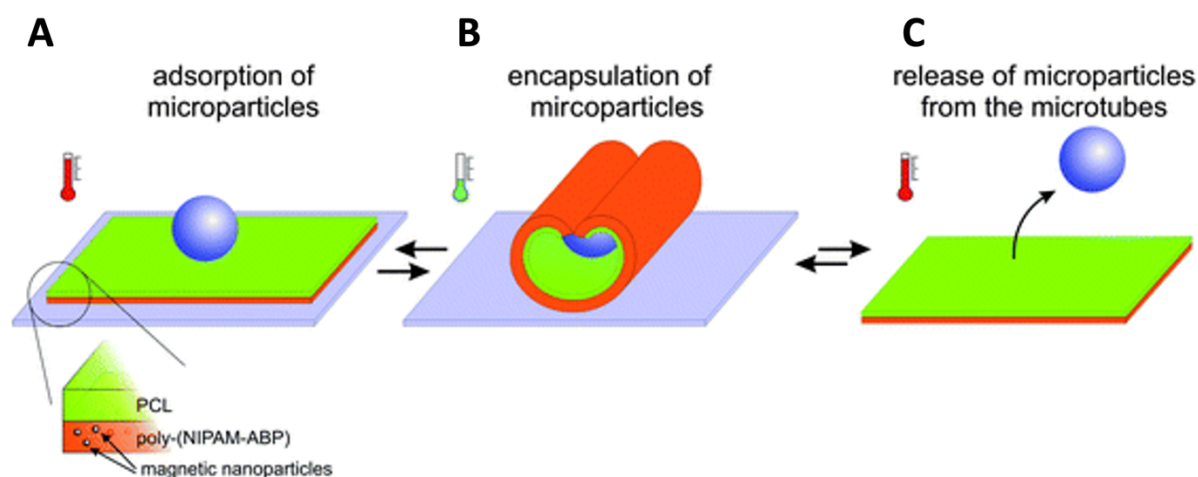


Figure 2-6: Thermo-responsive bilayers for reversible capture and release of microparticles. A) Films consisting of polycaprolactone (PCL) and poly(N-isopropylacrylamide-co-4-acryloylbenzophenone) (poly(NIPAM-ABP) with incorporated magnetic nanoparticles in an unactuated state at elevated temperatures. B) Encapsulation of microparticles at reduced temperatures via self-rolling mechanism. C) Release of microparticles at elevated temperatures.^[8]

solution temperature (LCST = 28°C) in aqueous media, meaning that the polymer only actuates if the temperature is below the one of the LCST, while the other layer consisting of poly(caprolactone) (PCL) remains unresponsive. Within 1–3 seconds, the bilayers roll and form tubes at a temperature below the LCST ($T < 28^\circ\text{C}$) (**Figure 2-6B**). These instant and reversible actuations enable the capture and release of microparticles in dependence on the temperature of the aqueous medium (**Figure 2-6C**). Further, the authors incorporated magnetic NPs into their thermo-responsive layer for an additional response to an externally applied magnetic field with which the authors can change the position of the microtubes (**Figure 2-6A**). The same group, Ionov, and his co-workers, further demonstrated short-side, long-side, and diagonal rolling of rectangular stimuli-responsive hydrogel-based polymer bilayers by varying the lengths, widths, and thicknesses of both active and passive material.^[77a]

A more complex approach to self-folding films or objects than bilayers and, due to geometrical anisotropy, is patterning. Similar to the previously described principle of

bilayers, one of the polymers remains unaffected by the stimulus, while the active one undergoes a shape transition that might be caused by surface forces, which results in shape change. Therefore, active materials are positioned at certain locations of an object that otherwise entirely consists of the passive material. Exposing the material to a stimulus induces a controlled actuation of the object as the stimulus only triggers the active material. Well-thought-out positioning of active polymers opens up new opportunities in shape reconfiguration of more complex geometries rather than the conventional self-folding into a tube. Gracias and co-workers reported polyhedral containers with variable shapes, sizes, and precisely defined porosities in all three dimensions. Therefore, hinges made of PCL were used that acted as active material and connected non-responsive SU-8 faces. At a temperature of 60°C, PCL melted and induced an irreversible shape reconfiguration into a cubic container.^[83] Based on the same principle, stimuli-responsive hinges were used to fold 2D objects into other geometries, like dodecahedrons,^[83] pyramids,^[84] and phlat balls.^[84a] The main application of these self-folding polymer thin films is to encapsulate and release drugs, particles, and cells in a controlled manner. Another application is demonstrated by Gracias and his co-workers, who reported self-folding polymers films for microfluidic purposes. More specifically, the group differentially photo-crosslinked SU-8 films, which self-folded after the desolvation in water and returned to their flat shape once the structure was immersed in acetone. Varying the UV exposure energy and direction enabled controlling the curvature in terms of extent and directionality. A multilayer patterning scheme to integrate PDMS-based microfluidic networks with these SU-8 films allowed the self-assembly of curved microfluidic networks.^[85] Overall, varying the aspect ratio and materials of multicompartmental particles, in which one material property differs from another, offers a variety of possible shape reconfigurations.

2.5. Bio-inspired Materials Systems

Over centuries, many living organisms have evolved mechanisms to sense and respond to changes in their environment. Scientists study these mechanisms to develop novel materials and stimuli-responsive systems that can mimic their behavior and are inspired by nature. Flowers, for instance, blossom due to a temperature change.^[86] A faster responsive plant is the *Mimosa pudica* plant, also known as the ‘shame plant’, which rapidly collapses its leaves upon touch to protect itself from herbivores (**Figure 2-7A-C**). The stimulus is transmitted as an action potential across all leaves attached to the stem. An exchange of ions is induced in the leaves and thus changes the turgor pressure in plant cells.^[87]

Certain carnivorous plants have developed highly modified leaves that act as traps. The Venus flytrap, *Dionaea muscipula Ellis*, is particularly intriguing due to its rapid trap closing mechanism of around 0.3 seconds.^[88] The leaf of the Venus flytrap is divided into two parts, the upper and lower part (**Figure 2-7D, E**).^[89] The upper leaf consists of two lobes and functions as a trap, which center appears in red. Attracted by the red color, insects touch the sensitive trigger hair on the leaves. The physical stimulation activates sensitive ion channels and, subsequently, motor cells. The leaves are closed within a fraction of a second, leaving the prey entrapped.^[90] Therefore, the Venus flytrap has received significant attention in numerous studies and has been described as ‘one of the most wonderful plants in the world’.^[91] Xu et al., for instance, designed a bio-inspired gripper to mimic the gripping process of the Venus flytrap. Similar to the carnivorous plant, the gripper has two-leaf-like structures with thorns, which help to seal and secure the gripper after closing. The gripper is driven by a dielectric elastomer actuator and is controlled by voltage. An applied voltage induces an expansion of the dielectric elastomer actuator, which opens up the leaves with an opening range of 32 degrees. Turning off the voltage, on the other hand, returns the actuator to its original closed state within 0.25 seconds.^[92]

Hong et al., for example, mimicked limb-like motions in biological systems and used poly(3,4-ethylenedioxythiophene)-poly(styrenesulfonate) (PEDOT:PSS) to vary the ion permeability of ionic electroactive polymer actuators. The usage of this conjugated polymer further enabled the control of ion movement through structural design to achieve intrinsic angular deformation. Sharp bending angles above 90° and beyond were reported. Electrochemical analysis indicates that the primary mechanism behind the actuation is the charging of electric double-layer capacitors via ion accumulation. Further, the expansion of the PEDOT:PSS layer is due to ion interchange and penetration.^[93]

Another artificial Venus flytrap was developed by Lim et al., which is a bimorph structure that also consists of PEDOT and a soft layer of poly(dimethylsiloxane) (PDMS). In this work, the photothermal layer was further doped with tosylate. The photothermal

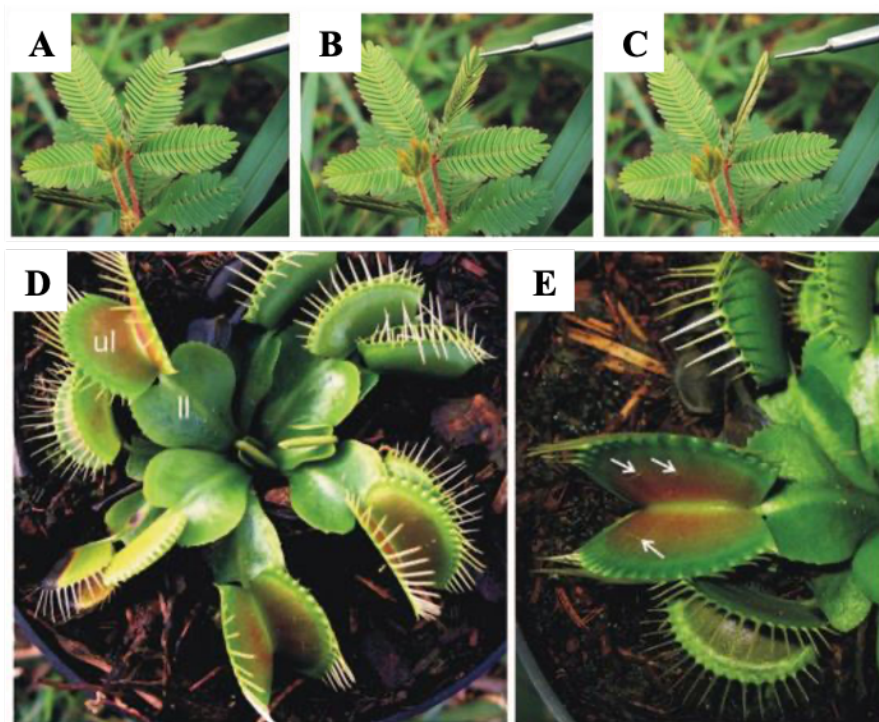


Figure 2-7: Stimuli-responsive plants. A-C) *Mimosa pudica*. Leaflets closing due to touch induced trigger. Time-lapse between each image is about 1 second. D, E) *Dionaea muscipula* Ellis (Venus flytrap). D) Leaves are divided into upper (ul) and the lower leaf (ll). E) The upper leaf consists of two lobes; which center is red colored and has three sensitive trigger hairs (arrows).^[7]

properties of PEDOT generate localized heat pockets within the structure once exposed to near-infrared (NIR) light of a wavelength of 808 nm and induce the bimorph to bend and close in less than 4 seconds. While the actuation is reversible as the structure re-opens, when the infrared light source is removed, the movement does not exhibit the typical snapping motion of the plant.^[94]

2.6. Biomaterials

Many definitions of the term “biomaterial” have been proposed over the years.^[95] Bruck, for instance, has defined biomaterials as “materials of synthetic or natural origin used alone or in combination with drugs as part of a device in the treatment, augmentation, or replacement of tissues or organs without causing acute or chronic harm to the host, while maintaining their intended biological and physical effectiveness during their useful service life in vivo”.^[96] In short, biomaterials are substances that are in contact with biological tissues or fluids without causing any inflammations or adverse side effects. Therefore, these materials find broad applications in modern medicine, such as implantable medical devices.^[97] Moreover, biomaterials can be used for drug delivery and also support wound healing.^[98]

Silk, for example, is a biomaterial that does not elicit a significant immune response and has been successfully used in wound healing and the tissue engineering field for bone, cartilage, tendon, and ligament tissues.^[99] Natural silk is a fibrous protein produced as fibers by spiders like *Nephila clavipes* and silkworms, such as *Bombyx mori*. The latter uses silk to form cocoons for its metamorphosis into a moth. One single strand of such a cocoon silk fiber consists of two silk fibroin (SF) cores, which are surrounded by a glue-like sericin coating acting as a protective layer.^[100] The simple amino acid composition is rich in glycine, alanine, serine, and tyrosine, and consists of two macromolecules, a heavy chain with molecular weights of 391 kDa and light chains with 26 kDa.^[101] The heavy chain sequence is repetitive

and semi-crystalline, which occurs in the repeated amino acid motifs. In the natural cocoon, these regions form a hydrogen-bonded, anti-parallel, β -sheet structure, which is hydrophobic, making silk insoluble.^[102] The sequence of the light chain, on the other hand, is non-repetitive and non-crystalline.^[100] The posterior gland of the *Bombyx mori* is known to exclusively synthesize fibroin chains, which is the most important protein of the silk.^[103] The SF concentration in the posterior gland is 12–15%. As a viscous solution with a concentration of 20–30%, the fibroin is stored in the middle region of the gland until needed for spinning, where sericin is also synthesized.^[104] The unique properties of SF, such as strength, flexibility, tailorable degradability and biocompatible nature make it an attractive material. Many research groups have used SF to fabricate films, porous matrices, hydrogels, nonwoven mats, yarns etc., due to its ease of processing.^[99, 105] Hereby, nearly 85% of the reported studies have used *Bombyx mori* silk fibroin (BmSF).^[106]

Li et al., for instance, used BmSF to fabricate electrospun scaffolds for bone tissue engineering. The scaffolds contain bone morphogenetic protein-2 (BMP-2), which are important for stimulating osteoblast differentiation and bone formation,^[107] and NPs made of hydroxyapatite, which is known as bone mineral.^[108] Compared to the controls, the group reported high calcium deposition and upregulation of BMP-2 transcripts levels, which helped the bone formation from human mesenchymal stem cells (hMSCs).^[109] Park et al. further compared electrospun BmSF scaffolds *in vitro* and *in vivo* to porous 3D poly(lactic acid) (PLA) scaffold, which were commercially available. The scaffolds were implanted at critical bone defect in rat calvaria. The electrospun BmSF scaffolds supported the proliferation and alkaline phosphatase activity of osteoblasts, which resulted in a bone regeneration of nearly 78.3%, whereas the PLA scaffolds only showed 49.31% bone regeneration.^[110]

In the vascular tissue engineering field non-woven, tubular nanofibrous SF scaffolds were fabricated via electrospinning to harness the materials mechanical properties.^[111] Zhang

et al., for instance, designed tubular SF scaffolds and cultured human coronary artery smooth muscle cells and human aortic endothelial on the luminal surface under physiological pulsatile flow.^[111c] Therefore, tubular silk scaffolds could be a significant advancement for tissue-engineered vascular grafts as they can closely mimic the mechanical properties and vascular cell outcomes of native vessels. The development of new biomaterials has been a rapidly growing research area. With the advancements of material science and biotechnology, biomaterials have the potential to revolutionize various fields.

2.7. Tissue Engineering

Tissue engineering is a multidisciplinary field where knowledge from various fields, such as biology, medicine, materials science, and engineering, are synergized to engineer tissues used as models for drug development and disease research. The major goal of tissue engineering, however, is to create the patient's tissues and organs in vitro, such as the heart, liver, and kidneys replacing diseased tissue.^[112] Current methods like artificial organs or organ transplantation, however, still require better biocompatibility and functionality despite the significant advances in the last years.^[113] Moreover, organ transplantation is limited by the shortage of donated organs. The risk of immune rejection is another hurdle of organ transplantation, which cannot be treated with immunosuppressive therapy.^[114] The applications to replace diseased tissues and organs range from developing skin grafts for burn victims to cartilage and bone regeneration.^[52b, 115] One of the biggest technological challenges, however, is mimicking the natural extracellular matrix (ECM).^[116] Thus, designing and fabricating ECM-like scaffolds have been the focus of attention within the tissue engineering field.^[106] The approach relies on three factors: i) cells, ii) scaffolds, and iii) growth factors.^[117]

The source of cells significantly impacts the success of tissue engineering.^[118] Based on their source type, cells can be classified into three groups. The first category is autologous, which are the patient's cells.^[119] The second, allogenic, is derived from other human sources, while animals are the source for the last class, xenogenic. The last two classes can elicit immune responses and therefore require immunosuppressive therapy.^[120] Thus, autologous cells are the most optimal cell source for tissue engineering. One challenge with these cells, however, is that harvesting a sufficient amount of cells is difficult.^[121] Especially harvesting cardiac cells from patients who suffer from myocardial infarction is extremely challenging. The cells can be expanded by cell culture, but this procedure is very time-consuming and expensive due to the required manpower and media.^[117]

The scaffold must meet several requirements to support the growth and differentiation of cells. Various materials, like synthetic polymers or natural biomaterials, can be used for fabricating scaffolds.^[122] Even decellularized tissues are often used and seeded with new cells before the implantation into a host for further growth and differentiation into functional tissue.^[123] One requirement the scaffolds should meet is the interconnectivity of micropores, which enables the seeded cells to migrate within the pores and increase the cell number. Moreover, these pores allow a sufficient nutrient supply to the cells and waste transport, which is crucial for cell survival inside the scaffold.^[124] Optimal pore sizes range from 100 – 500 μm .^[125] Further, scaffolds must meet the mechanical requirements in terms of strength and absorption kinetics. For bone regeneration, for instance, scaffolds should slowly degrade to maintain their mechanical strength until the tissue is fully regenerated. The skin, on the other hand, requires a scaffold that can degrade within a month, as scaffolds that stay longer than needed in contact with the tissue can hinder tissue regeneration.^[117, 126] To fabricate porous scaffolds various methods like freeze-drying, porogen leaching, and

electrospinning have been applied.^[127] The pore size of electrospun nanofiber sheets, however, is too small for cell migration.

Growth factors are proteins that play an important role in cell proliferation and differentiation.^[128] Cells endogenously secrete growth factors in the body or result from communication with surrounding cells.^[117] Incorporating growth factors into engineered tissues for wound repair, for example, can significantly improve the healing process compared to non-biological wound covers.^[129]

Tissue engineering is a promising field and has the potential to treat diseases and injuries by providing opportunities for personalized medicine. Nonetheless, many challenges need to be tackled to ensure the long-term viability and function of the engineered tissues.^[130] Moreover, biocompatibility needs to be improved to minimize the risk of rejection once the tissue is integrated into the host.^[120]

2.8. Microanalytical Sensing Devices

Sensors have revolutionized the field of analytics by providing unprecedented precision and accuracy in the measurement of the physical and chemical properties of a sample. The directly obtained signals (*in situ*) provide real-time information, making them attractive as a tool for industrial and research applications. The widespread use of sensors in various industries and fields, including (bio)chemistry, environmental and material science, as well as healthcare, reflect their significance as analytical instruments. Typically, a combination of optical, electrical, or chemical methods enables the obtainment of information about the sample being analyzed. Electrochemical sensors, for instance, that mostly operate in the potentiometric or amperometric mode use an electrical current to measure sample properties, such as pH, dissolved oxygen, or the presence of a specific ion. Their sensor size of mostly 12 mm is dictated by standards,^[131] which restrict the direct usage of most of the

commercially available sensors with small sample volumes, such as blood, sweat, saliva, liquor, or directly in the human body.^[132] Standard sensor devices limited by the dimensions of the sensors can be miniaturized by precision engineering. However, this miniaturization down to the micrometer range is limited due to the requirement for a minimum amount of functional substances, such as a reference electrolyte, to ensure a minimum operational lifespan for the sensors.^[133]

In recent years, there have been significant advancements in the field of microanalytical systems.^[1b, 134] Similar to the abovementioned sensors, microanalytical sensing devices are a type of scientific instrument designed to detect and analyze various chemical and physical properties of a sample, however, at a microscale level. The compact size of these microanalytical devices and their highly integrated architecture enable analyte detection from low and diluted sample volumes. Moreover, another advantage of the reduced sensing area is the increase in sensing resolution. At the same time, nonetheless, the small sensing area limits the detection accuracy as the probability of the analyte reaching the detection patch is significantly reduced due to the 3D diffusion of the analyte through the sample space until finally encountering the detection patch.^[135] Further, a less accurate detection output is measured in case of an analyte depletion adjacent to the detection patch.^[136] Therefore, mass transport limitation is often cited as the root cause for low sensitivity as it hinders analyte collection and presents the bottleneck of current microanalytical systems.^[136-137]

To overcome the challenges of mass transport limitations, motor proteins or chemically and topographically patterned protein tracks have been proposed by various research groups to speed up the analyte collection time.^[138] Ibusuki et al., for instance, combined biomolecular motor dynein and DNA binding proteins to develop protein-based motors, which move on DNA nanotubes. The advantage of these novel motors and nanoarchitecture

based on DNA is the enabled arrangement of binding sites on the track, which allowed the control of directed movement. Further, the group also demonstrated multiplexed cargo transport by different motors.^[139] The production of these complex materials, however, is limited in its scalability as fabricating these biomolecular motor-based devices is expensive and time-consuming.^[24a, 140] Other efforts to improve the detection sensitivity by direct transport include surface gradients. Over a given distance, these surfaces change their physical or chemical properties.^[141] The Braun group has reported functionalized patterned polymer brushes that can precisely guide the diffusive transport of small molecules through microscale pathways for the on-chip transport of molecules.^[141b] The downside of these platforms, however, can be surface irregularities^[142] and non-specificity.^[143] Moreover, due to the numerous parameters that are involved in optimizing conditions, the scalability can be negatively impacted as the repeatability is limited.^[144]

2.9. Soft Robotics

Soft robotics is a new field within robotics. The main differences to conventional robotics are the materials used for robots. While conventional robots are made of high-stiffness materials like steel, aluminum, or titanium, soft robots use hyper-elastic materials like polymers, rubber, and silicone for the main body and moving parts. The shock-absorbing materials for soft robotics exhibit material stiffness in the order of $10^4 - 10^9$ Pa, comparable to biological skin or muscle tissue.^[145] Conventional robots, however, lack these shock-absorbing properties making more complex protection crucial. The material difference is, at the same time, one great advantage of soft robotics as the more pliable materials can be easily deformed and conform to their environment. Simultaneously, soft robots remain mechanically resilient, which enables soft robotics operations with increased safety, adaptability, and flexibility. All these advantages offer ample application opportunities like

manufacturing and safety within fields such as healthcare. For medical procedures, for instance, which require access to soft tissues and organs, soft robots can accurately execute their tasks without causing harm to humans. Traditional and rigid robots, on the other hand, could be dangerous and pose a potential risk to sensitive tissues.^[145] Another difference between soft and rigid robotics is their respective manufacturing process. While the latter is often mechanically assembled using machining tools, like milling, lathes, or CNC machines, soft robots are fabricated via 3D printing or molding, which enables lower manufacturing costs. Soft robotics has gained significant momentum in the last decades. This increased interest in soft robotics is not least due to the remarkable advances in artificial intelligence. Therefore, integrated sensors and actuators within the systems are crucial to allow robots to interact with their surroundings. At the same time, this high integration presents challenges when downscaling soft robots to a sub-centimeter size. Parts for data analysis, power, and sensing, for example, have to be moved off-board. Soft actuators on a small scale that respond with deformations to various stimuli, such as thermal, magnetic, or electric fields, are, nonetheless, of great interest for applications in artificial muscles, microrobots, micro-manipulators, and microfluidic systems. Conventional robots can generate greater forces than soft robots ranging from a few millinewtons (mN) to meganewtons (MN) actuated by electrical motors, hydraulic pumps, or pneumatic compressors.^[146] Soft robots, on the other hand, cannot generate large forces due to their elastic materials and usage of pneumatic compressors, shape-memory alloys, and electro-active polymer (EAP), amongst others. **Table 2-2** presents a selection of the extensive literature on soft actuators and provides a glimpse into the diverse range of various classes.

Dielectric elastomer actuators are electrically responsive actuators based on Coulombic attraction between two flexible electrodes with a potential difference located on separate ends of a compressible membrane. Various research groups have demonstrated the

application of dielectric elastomer actuators as artificial muscles proving that the performance of the artificial muscle is comparable to the biological one. Jung et al., for example, mimicked the unique motion of annelids by stacking millimeter-sized soft actuators based on dielectric elastomers.^[147] The typical materials of dielectric elastomer actuators, such as silicones, acrylic elastomers, polyurethanes, and rubbers, allow the actuators to achieve large deformations.^[148] Moreover, casting and 3D printing these materials into various shapes enables different movements, including bending, rolling, and folding. Therefore, many dielectric elastomer actuators find their purpose as soft grippers, as they can grab and release delicate objects. Shintake et al., for instance, showed the versatility of their soft grippers, which can manipulate a wide range of objects in terms of haptics, weight, and shape. The soft grippers could pick up and release light objects like a piece of paper weighing 0.8 g, but also heavier and more fragile ones like a highly deformable balloon filled with water (35.6 g) and a metallic oil can up to 82.1 g.^[149] In general, dielectric elastomer actuators are characterized by their high flexibility, energy density, and strains, which possess self-sensing characteristics. However, one disadvantage of these actuators is the need to operate them with large voltages in the kilovolt range, making them sensitive to electrical breakdowns. Further, the viscoelasticity of the materials can limit the actuator's bandwidth, and the produced strain is low.

NIR-driven actuators are photo-responsive actuators that have gained significant interest in the biomedical field as long-wavelength NIR light can penetrate biological tissue with low losses. Therefore, photochromic molecules, such as graphene, carbon nanotubes, or metal nanoparticles, are incorporated into polymers, which absorb NIR light upon exposure and transform photon energy into thermal energy. Ultimately, this energy transformation modifies the polymer properties, like phase transition, swelling, or thermal expansion. Despite the advantages of biocompatible actuation, NIR-driven actuators suffer from low

actuation speeds. An increase in photochromic molecules within the polymer would increase the NIR light absorption and subsequent energy transformation. Simultaneously, however, this increase comes with a trade-off as the mechanical properties of the polymer are negatively impacted.

Table 2-2: Overview of Soft Actuators

Stimulus	Type of Soft Actuator	Mechanism	References
Electric	Dielectric elastomer	Coulombic attraction between two flexible electrodes with potential differences, which are located on separate ends of a compressible membrane.	[147, 149-150]
	Piezoelectric	An electric field induces mechanical deformation, and vice versa, voltage or electric charge, is generated due to the application of mechanical or vibrational forces.	[151]
	Mechanical/servo motor	Electrically powered servomotor connected to soft parts of robot.	[150, 152]
	Neurostimulation	Sensing of electrical signals generated through neurons communication.	[153]
Explosive		Induced motion, such as jumping due to chemically-induced reaction resulting in explosion.	[154]
Magnetic		Incorporation of magnetic particles and fillers within materials. Actuation by controlling magnetic field direction and magnitude.	[155]

Photo-responsive	NIR light driven	Polymer doping with photothermal reagents like carbon nanotubes, metal nanoparticles, and graphene transform photon energy into thermal one inducing thermal expansion, swelling, or phase transition.	[156]
	Visible light driven	Liquid crystal polymer networks or carbon-based materials transforms light into mechanical energy.	[157]
Pressure	Pneumatic	Pressurized gas or air deflects the chambers by increasing or decreasing the volume, which is transformed into motion.	[158]
	Hydraulic	Fluids are pumped into designed chambers to achieve a desired movement.	[159]
Thermal	Synthetic hydrogels	3D polymer network (de-) swells upon exposure of light, temperature, or pH, etc.	[30, 160]
	Shape memory alloy	Material's inability to undergo reversible changes in the crystal structure, deform, and return to material's original shape under loading/thermal cycles. Alloying a variety of materials to achieve desired actuation.	[161]
	Shape memory polymer	Actuation into temporary and permanent shape due to an applied stimulus (e.g., light or heat).	[162]
	Liquid crystal elastomer	Liquid crystals incorporated into a polymer network induce deformations when stimulated by heat, light, or electric fields as liquid crystal molecules undergo a phase transition and orientate.	[163]

2.10. Graphene and Its Derivatives

In the last decades, graphene and its derivatives have gained significant interest in the scientific field. The 2D material consists of a single layer of carbon atoms, which are arranged in a hexagonal lattice, as seen in **Figure 2-8A**. With the emergence of graphene, various forms of carbon nanostructures have been introduced. Fullerene, for instance, is formed by wrapping up the 2D graphene layer into 0D molecules. The by far most investigated type of fullerene molecule is buckminsterfullerene, also known as C_{60} or buckyball, which consists of 60 carbon atoms arranged in a spherical shape. This specific type of fullerene resembles the geodesic domes created by architect Buckminster Fuller, hence the name. Buckminsterfullerenes show promising applications in the biomedical field due to its anti-

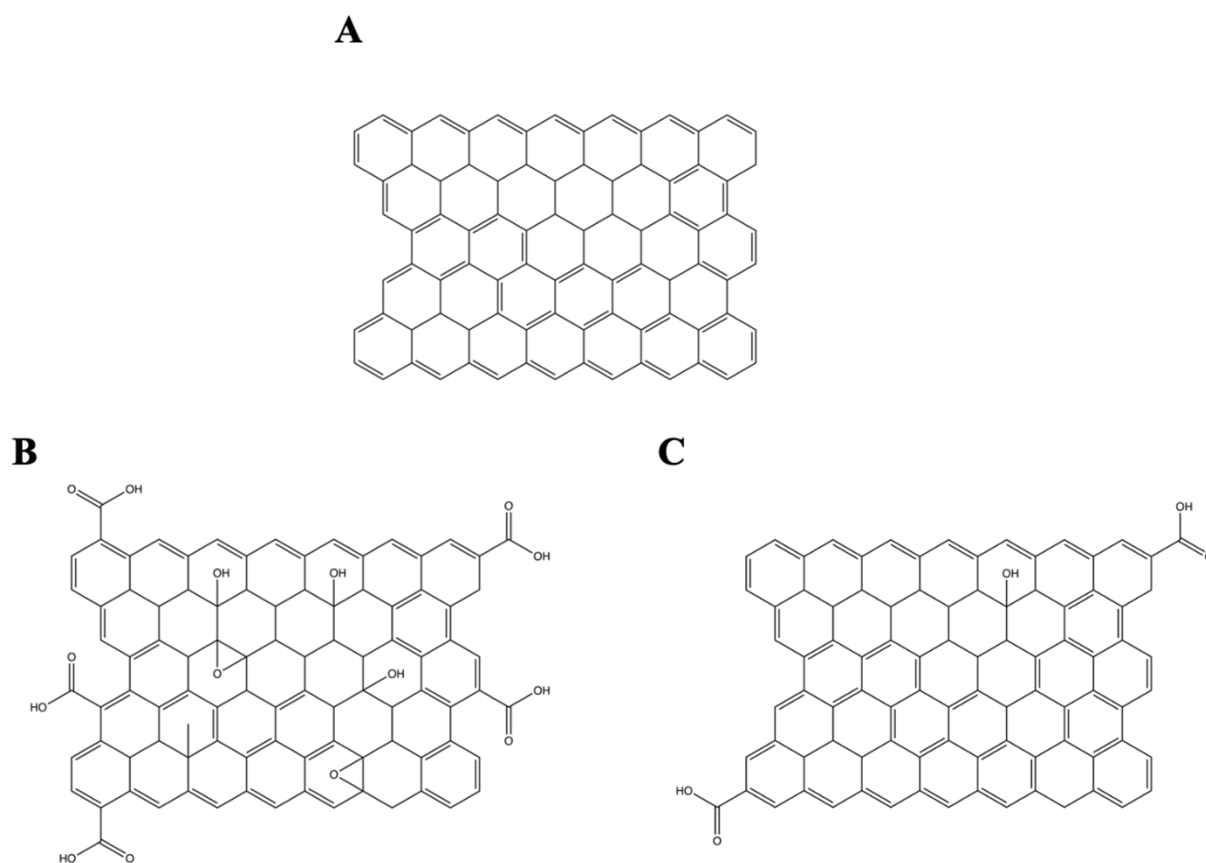


Figure 2-8: Graphene and its derivatives. A) Graphene. B) Graphene Oxide. C) Reduced Graphene Oxide. All images reproduced under terms of the CC BY-SA 4.0. Copyright 2022, PackBMEengineer.

oxidant features,^[164] but also in various types of organic semiconductor devices.^[165] Carbon nanotubes and graphite are other forms of carbon nanostructures that are formed by cylindrically rolling the 2D graphene layer into 1D nanotubes, or stacking the 2D graphene layers into a 3D structure, respectively. The latter, graphite, is, for example used as electrode material for electrochemical reactions due to its electrical conductivity and chemical inertness towards a broad range of reagents and solvents.^[166] Carbon nanotubes, on the other hand, find applications in the field of biotechnology as components of biosensors^[167] and medical devices^[168] since they enable fluorescent,^[169] as well as photoacoustic imaging.^[170] Further, carbon nanotubes can induce localized heating upon NIR radiation. Overall, graphene has paved the way for numerous innovative areas in science and technology. Graphene's exceptional properties, such as high mechanical strength,^[171] impermeability to gases,^[172] thermal,^[173] and electrical conductivity,^[174] make it a highly desirable material for a wide range of applications in various fields, such as sensors, electronics, and biomedicine. Graphene has outperformed many materials, such as copper by withstanding electric current densities that are a million times higher than copper. Moreover, some characteristics have even reached theoretically predicted limits, like the electron mobility at room temperature with $2.5 \times 10^5 \text{ cm}^2 \text{ V}^{-1} \text{ s}^{-1}$,^[175] while the theoretical limit is $\sim 2 \times 10^5 \text{ cm}^2 \text{ V}^{-1} \text{ s}^{-1}$.^[176] The same applies to graphene's intrinsic strength of 130 GPa,^[171] which value is close to the theoretical one obtained by Griffith.^[177] In terms of mechanical properties, graphene also has an outstandingly high Young's modulus of 1 TPa.^[171] In comparison, the theoretical value of steel is five times lower than that of graphene ($E = 0.2 \text{ TPa}$).^[178] Various research groups have further reported the superior thermal conductivity of graphene exceeding $\kappa = \sim 3,000 \text{ W mK}^{-1}$ near room temperature.^[173] Some of these exceptional characteristics, however, have only been achieved for mechanically exfoliated graphene^[179] and graphene, which is deposited on special substrates like hexagonal boron nitride.^[175, 180] Moreover,

depending on the method being used to prepare graphene, dimensions, shapes, and quality can vary, which subsequently impacts the material's properties.^[181] Mechanical exfoliation, as mentioned above, is one fabrication method of graphene in which strongly layered materials, like graphite, are mechanically split by using scotch tape. This technique, therefore also often referred to as the scotch tape technique, enables the extraction of highly structural crystals and electronic quality. However, as this approach is labor-intensive and time-consuming, mechanical exfoliation is not suitable for industry-scale production.^[174a] Liquid-phase exfoliation of graphite, on the other hand, allows graphene production on an industrial scale. In this method, graphite is typically exposed to non-aqueous solvents, which surface tension favors the increase in the total area of graphite crystallites. Via sonication, graphite is then split into single platelets, and finally into monolayer flakes after prolonged treatment. The suspension containing these monolayer flakes is then concentrated by centrifugation.^[181-182] Chemical vapor deposition (CVD) is another approach to produce graphene, which, however, then exists as polycrystalline film or powder made of micro- to millimeter-sized domains.^[183] Carbon-containing gas, such as methane, ethylene, or acetylene are typically used as gaseous carbon precursors and are introduced into a high-temperature chamber along with a substrate material, like copper or nickel.^[184] At temperatures above 1200°C, methane gas, for instance, decomposes on the surface of the substrate.^[185] The carbon atoms then form graphene layers on top of the substrate until the growth process is stopped. One advantage of the CVD method is that it allows the precise control of the graphene thickness, uniformity, as well as quality.^[183, 186] Irrespective of the synthesis method, studies have shown that graphene exhibits a remarkable response to infrared (IR) radiation through photothermal conversion, as graphene is composed of sp^2 -bonded carbon network, which undergoes various stretching and bending vibrations.^[187] During the forced resonance vibration process the IR-phonon interactions increases the degree of disorder and kinetic vibration energy is converted into

heat motion energy. This photothermal conversion, combined with graphene's high thermal conductivity enable the development of novel devices, which harnesses these properties for optically driven actuators, for instance, and show great potential for wireless actuation and remote displacement controls. Based on this concept, Loomis et al. have designed graphene-PDMS composites and demonstrated reversible, elastic expansion and contraction under IR exposure. By adding 0.1 – 2.0% w/w graphene nanoplatelets into PDMS, changes in stress were measured, which were four orders of magnitude higher than those of pristine PDMS polymer.^[188] Other types of actuators have been reported, which are, for instance, thermally responsive.^[189] Moreover, graphene has been utilized to fabricate ionic electroactive actuators,^[190] dielectric elastomer,^[191] or acoustic ones.^[192]

Graphene derivatives, the so-called “cousins” of graphene, have also gained significant interest in the last decades as certain physical, magnetic, as well as chemical properties, such as surface energy, electronic structure, or reactivity can be tailored. **Table 2-3** shows the similarities and differences in the properties of graphene and its derivatives. The most prominent form of functionalized graphene is graphene oxide, which synthesis is based on the oxidation of graphite.^[193] Graphite oxide is then mechanically exfoliated and various oxygen functionalities, like hydroxyls, carboxylic acid, ketone groups, epoxides, and others like lactones and esters are found on the resulting graphene oxide.^[194] This functionalization is responsible for graphene oxide's hydrophilicity, as exfoliated graphene is hydrophobic in nature, and therefore, not dispersible in water. The changed material property makes graphene oxide, compared to graphene, a more attractive material for applications that, for instance, involve the dispersion with aqueous solutions. Moreover, graphene oxide shows fluorescence quenching ability, surface functionalization capability, and amphiphilicity for biotechnological applications.^[195] However, the oxidation of graphene

comes with a trade-off of the reduced electrical^[196] and thermal conductivity of $\kappa = 0.5 - 1.0 \text{ W m}^{-1} \text{ k}^{-1}$.^[197]

Reduced graphene oxide is another graphene derivative, which has fewer oxygen functional groups than graphene oxide. Emerging from the more cost-effective production of graphene by reducing the cheap graphene oxide via thermal, chemical, and electrochemical treatments, reduced graphene oxide shows graphene-like properties. Its good electrical conductivity $\gamma = 103.3 \text{ S cm}^{-1}$,^[198] and thermal conductivity $\kappa = 30 - 2600 \text{ W m}^{-1} \text{ k}^{-1}$,^[199] make reduced graphene oxide a good compromise between graphene and graphene oxide.^[200]

Overall, the exceptional properties of graphene and its derivatives make them highly desirable materials for a wide range of applications. Ongoing research in graphene is expected to result in new discoveries and applications.

Table 2-3: Properties of graphene and its derivatives.

Properties	Graphene	Graphene Oxide	Reduced Graphene Oxide
Electrical Conductivity	10^6 S cm^{-1} ^[201]	Insulating/semi-conductive ^[196]	103.3 S cm^{-1} ^[198]
Thermal Conductivity	$5000 \text{ W m}^{-1} \text{ k}^{-1}$ ^[173a]	$0.5 - 1.0 \text{ W m}^{-1} \text{ k}^{-1}$ ^[197]	$30 - 2600 \text{ W m}^{-1} \text{ k}^{-1}$ ^[199]
Hydrophilicity	hydrophobic ^[202]	hydrophilic ^[202]	hydrophobic ^[202]

3. Materials and Methods

3.1. Chemicals

The chemicals were used without further purification and were of analytical grade. For all experiments, Milli-Q water was used, which was purified with a MilliQ-Plus System from Merck Millipore.

Table 3-1 lists all used chemicals, materials, and lab supplies, which were additionally obtained to the ones from VWR.

Table 3-1: Used chemicals and materials

Jetting Solutions:

Chemicals	Company
Poly(acrylic acid) (PAA) $M_w = 450\,000\text{ g mol}^{-1}$	Sigma Aldrich
Ethylene glycol	Merck KGaA
Poly(ethylene glycol diacrylate) (PEGDA) $M_w = 700\text{ g mol}^{-1}$	Merck KGaA
2-hydroxy-4'-(2-hydroxyethoxy)-2-methylpropiophenone (Irgacure 2959)	Sigma Aldrich
Silk fibroin lyophilized powder (SF) $M_w = 100,000 - 150,000\text{ g mol}^{-1}$	Advanced BioMatrix
Calcium lignosulfonate	Provided by IONYS AG
Cremophore	Provided by IONYS AG
Graphene, single layer	Thermo Scientific
Nigrosine, water soluble	Thermo Scientific
Soy Lecithin	Sigma Aldrich
Tween20	Sigma Aldrich
Glycerol	Sigma Aldrich
mPEG-Rhodamine, mPEG-FITC $M_w = 2\,000\text{ g mol}^{-1}$	Creative PEGWorks

Materials	Company
Potassium dihydrogen phosphate ($\geq 99.0\%$ ACS)	Honeywell Chemicals
Citric Acid	Sigma Aldrich
Sylgard 184 (PDMS)	Dow Corning Corporation
Microparticles: <ul style="list-style-type: none"> • MF-FluoBlue 9.8 • PS-R-214.0 	microparticles GmbH
Silicon wafers with a native oxide layer	Siegert Wafer GmbH
Dimethyloctadecyl-[3-(trimethoxysilyl)-propyl]-ammoniumchlorid (DMOAP) solution in 60% wt methanol	Sigma Aldrich
Metallic needles (25G, ID = 0.84 mm)	Nordson EFD
Syringes (1 mL)	Braun
Grinding balls 3 mm hardened stainless steel	Fritsch

3.2. Instrumentation

In **Table 3-2** all instruments are listed, which were used to conduct this work. This includes the entire jetting station setup and the instruments for optical, as well as chemical analyses of the respective samples.

Table 3-2: List of used instruments

Instruments	Company
Computer-assisted XY Stages	Newport Corporation
External power source	FuG Elektronik
Syringe pumps LA-110	Landgraf HLL GmbH
VHX-5000	Keyence
MED 020 device	Bal-Tec AG
VEGA 3	TESCAN
SP5 Confocal microscope	Leica
BX53	Olympus
Genesys 180 UV-Vis Spectrophotometer	Thermo Scientific
TC-3F Bioreactor	EBERS Medical Technology S.L.
Pulverisette 6	Fritsch GmbH
SOLIS-850C - High-Power LED for Microscopy	Thorlabs
SOLIS-565C - High-Power LED for Microscopy	Thorlabs
J-815 CD Spectrophotometer	Jasco
Senterra Raman microscope	Bruker Optics
Landmark® 370.10 Servohydraulic Test Systems	MTS Systems GmbH

3.3. Software

Table 3-3 lists all software, which was used to control the computer-assisted stages of the jetting station and to perform and plot (image-based) analyses and data.

Table 3-3: List of used software

Software	Company
Labview	National Instruments
DMC	Direct Machining Control
MatLab	MathWorks
ImageJ	National Institutes of Health
GraphPad Prism v9	GraphPad Software Inc.
Origin	OriginLab Corporation
Opus	Bruker

3.4. Polymeric solution for Electrohydrodynamic (Co-) Jet Writing

Table 3-4 contains the composition of the various polymer solutions that were prepared for the respective projects. For the bicompartamental fibers two jetting solutions of 15.0% weight per volume (w/v) poly(acrylic acid) (PAA) in Milli-Q water were prepared with different ethylene glycol concentrations (0.5% and 20.0% volume per volume, (v/v)).^[2] The monocompartamental fibers and scaffolds were fabricated with the poly(ethylene glycol diacrylate) (PEGDA) – PAA hydrogel solution. For this hydrogel solution, 7.5% (w/v) PAA was mixed with 80% w/v PEGDA. After homogeneous mixing, 80 μ L of 10% (w/v) 2-hydroxy-4'-(2-hydroxyethoxy)-2-methylpropiophenone (Irgacure 2959) in an ethanol and water (70:30) solution was added as a radical initiator, as described elsewhere.^[203] For the bicompartamental silk fibers, lyophilized silk fibroin powder (SF, 50.0% w/v) is added to Milli-Q water and thoroughly mixed until fully dissolved. The solution is then centrifuged at 2460 relative centrifugal force (RCF) for 30 minutes to remove all bubbles. While the non-actuating silk compartment only consists of 50.0% w/v SF solution, the actuating compartment consists of 50.0% w/v SF and various concentrations of nigrosine and pre-treated graphene. Respective amounts of nigrosine were dissolved in Milli-Q water and added to lyophilized SF powder to form 50.0% w/v SF solution. For the pre-treatment of graphene, 200 mg graphene were wet-ground with 20.0 mL methanol in a planetary mono mill (Pulverisette 6, Fritsch GmbH, Germany). At 300 rounds per minute (RPM) the graphene was ground by 3 mm stainless steel balls for 30 minutes. After milling, the graphene-methanol mixture was transferred to a flask for reflux with an additional 25.0 mL methanol. The solvent and graphene mixture were heated to 100°C and magnetically stirred for 1.5 hours until methanol fully evaporated. Once the mixture cooled down, 4.0 mL of calcium lignosulfonate (1.00% w/v) and cremophor (0.125% w/v) were added. The

mixture was then ultrasonicated for 2 hours at 100% sonication power resulting in a 5.0% w/v graphene suspension. Respective amounts of the suspension were then added to lyophilized SF powder.

Table 3-4: List of polymer solutions for jetting

Compartments	Materials	Polymer Concentration	Solvent	Crosslinker
Bicompartmental	Poly(acrylic acid) (PAA)	15% (w/v)	Milli-Q water	0.5% Ethylene glycol (EG)
	PAA	15% (w/v)	Milli-Q water	20% (v/v) EG
	Silk Fibroin (SF)	50% (w/v)	Milli-Q water	Methanol-treated after jetting
	SF Pre-treated graphene Nigrosine	50% (w/v)	Milli-Q water	Methanol-treated after jetting
Monocompartmental	Poly(ethylene glycol diacrylate) (PEGDA)	80% (w/v)	Milli-Q water	10% (w/v) 2-hydroxy-4'-(2-hydroxyethoxy)-2-methylpropiophenone (Irgacure 2959) in ethanol and water (70:30) solution
	PAA	7.5% (w/v)		

3.5. Optical Sample Analyses

For optical analyses, samples and experiments were imaged with a bright-field microscope (VHX-5000, Keyence, Germany), fluorescence and polarized light microscope (BX53, Olympus, Germany), confocal laser scanning microscopy (CLSM), and scanning electron microscope (SEM, VEGA 3, TESCAN, Germany). For polarized light microscopy, samples on glass slides are examined between crossed polarizers. For SEM imaging the samples were sputter-coated with an approximately 5 nm gold–palladium [80:20] layer to improve the conductivity using a MED 020 device (Bal-Tec AG, Balzers, Liechtenstein). SEM images

were obtained at voltages ranging from 2.0 – 8.0 kV. LSCM was performed on a Leica SP5 inverted confocal microscope (Leica, Germany). To visualize mono- and bicompartmental fibers, the compartments were fluorescently labeled with mPEG-Rhodamine (Ex/Em 570/595 nm) and mPEG-Fluorescein isothiocyanate (FITC) (Ex/Em 494/521 nm), respectively. All images were processed using ImageJ.

3.6. Statistical Analysis

All experiments were repeated at least three times. Microsoft Office Excel (Microsoft, USA) was used to process the data. All statistical analyses were carried out using GraphPad Prism v9 software (GraphPad Software, Inc., USA). All data are presented as mean \pm standard error of the mean (S.E.M). Statistical significance was analyzed using one-way analysis of variance with Tukey's multiple-comparison test. *p*-Values represent different levels of significance; *p* < 0.05 *; *p* < 0.01 **; *p* < 0.001 ***; *p* < 0.0001****.

3.7. Electrohydrodynamic (Co-) Jet Writing of PAA

Scaffolds made of bicompartmental fibers were fabricated using the EHD co-jetting procedure with the two PAA jetting solutions and the respective ethylene glycol concentrations. A syringe pump (LA-110, Landgraf HLL GmbH, Germany) with a flow rate of 20 μ L per hour was set to flow the two polymeric solutions in a laminar regime through parallel metallic needles (25G, ID = 0.84 mm, Nordson EFD, USA). An external power source (FuG Elektronik, Germany) charged the needles to -1.9 kV. The grounded collector plate was mounted on a computer-assisted x-y stage (Newport Corporation, USA). The x-y stage was controlled by software (Direct Machining Control, Lithuania) that precisely placed the stable polymer jet into pre-programmed structures with the collector moving at a speed of

25 mm s⁻¹. The distance between the needles and the collector plate was kept constant at 0.5 cm. The bicompartmental fibers were jetted on Dimethyloctadecyl-[3-(trimethoxysilyl)-propyl]-ammoniumchlorid (DMOAP)-coated silicon wafers, which were placed on top of the collector plate. All other samples were jetted onto silicon wafers. For samples examined with the confocal microscope, glass slides were used. All samples were crosslinked for 15 minutes at 130°C.

3.8. Swelling Properties of PAA fibers

The different swelling properties of 15.0% PAA fibers (mono- and bicompartmental) were determined in the following pH 3.0, 4.0, 5.0, 7.0, 9.0. All buffers had a molarity of 0.1 M and an ionic strength of 0.265 M.

For the swelling factor Q , the fiber diameters ($n = 5$) were measured in a dry d_d and swollen d_s state after being immersed in the respective buffer overnight and calculated with the following equation:

$$Q = \frac{d_s - d_d}{d_d} \quad \text{Equation 1}$$

The bending radius R was measured with ImageJ to obtain the curvature K of bicompartmental fibers with the following equation:

$$K = \frac{1}{R} \quad \text{Equation 2}$$

The circularity C of the bicompartmental fibers was determined for pH 7.0 and pH 9.0 with ImageJ that uses the following equation with surface area A , and perimeter p :

$$C = \frac{4\pi A}{p^2} \quad \text{Equation 3}$$

For the aspect ratio AR of the bicompartmental fibers the diameters d of major and minor axes were determined in the following pH values 7.0 and 9.0 with ImageJ and calculated using the following equation:

$$AR = \frac{d_{major}}{d_{minor}} \quad \text{Equation 4}$$

The bending strain ε of bicompartmental fibers were determined over time. Therefore, the fiber radius r_f and bending radius R were measured with ImageJ for the following equation:

$$\varepsilon = \frac{r_f}{R} \quad \text{Equation 5}$$

3.9. Analyte Transport Experiment

A chamber-like structure was placed onto the scaffold and consisted of a glass coverslip and PDMS strips. The chamber was then filled with a non-actuating solution (pH 3.0). With a pipette, 10 μL of a microparticle suspension at varying concentrations ($c = 1, 5, 10, 15, 20, 25, 30, 35, 40, 45, \text{ and } 50 \mu\text{g mL}^{-1}$) were added to the scaffold. Once the chamber was filled, three syringe pumps gradually replaced the acidic solution with an actuating solution

(pH 7.0). Two syringe pumps, one at the top and the other at the bottom, ensured a laminar flow. A third syringe pump was used to withdraw the solution from the site. All syringes were operated with syringe pumps at flow rates of 40 and 80 μL per hour, respectively. For separation experiments, non-binding spheres were prepared by immersing FITC carboxylated polystyrene particles in 3 – 5% DMOAP (60% in methanol) for 10 minutes and then washing them with Mili-Q water.

3.10. Fluorescence Signal and Enhancement Factor

Images of fluorescently-labeled microspheres (diameter $d = 10 \mu\text{m}$) were taken before and after the actuation with the fluorescence microscope. All settings, such as gain, exposure time, and magnification were kept constant throughout all experiments. The fluorescence signal F was determined by processing the images with ImageJ. Therefore, the region of interest (ROI) was selected and the integrated density, surface area of the selected ROI, and background for correction were measured. With the following equation the corrected F was calculated:

$$F = \text{Integrated Density} - (\text{Area of selected ROI} * \text{Mean Fluorescence of Background}) \quad \text{Equation 6}$$

Based on the calculated F , the enhancement factor was determined with the following equation:

$$\text{Enhancement Factor} = \frac{F_{\text{after}}}{F_{\text{before}}} \quad \text{Equation 7}$$

The standard curve of various particle concentrations of fluorescently-labeled microspheres ($d = 10 \mu\text{m}$) ($c = 0.025, 0.05, 0.1, 0.25, 0.5, 1, 2.5, 5, 10, 15, 20, 25, 30, 35, 40, 45, 50, 60,$ and $70 \mu\text{g mL}^{-1}$), was determined and calculated with **Equation 6**. Therefore, $10 \mu\text{L}$ of the respective concentration was placed on a silicon wafer. The droplet was imaged with a fluorescence microscope.

3.11. Fiber Force Measurement

Silicon wafers were coated with polytetrafluoroethylene (PTFE) to prevent friction during fiber force measurements. First, the bicompartamental fibers were jetted onto the wafers. Then, a single PMMA fiber was jetted perpendicular to the bicompartamental fibers, as seen in **Figure 3-1**. The wafer was placed at an angle of 5° on the microscope table. Like previous actuation experiments, the pre-filled chamber containing the non-actuating pH 3.0 solution was replaced with pH 7.0. The actuated PAA fibers displaced the PMMA fiber with a known mass (**Equation 8**). Considering the angled wafer and the actual distances covered by the fibers (**Equation 10 & Equation 11**), the work generated by the bicompartamental fibers can be determined, as described in **Equation 9**. Finally, the force can be calculated

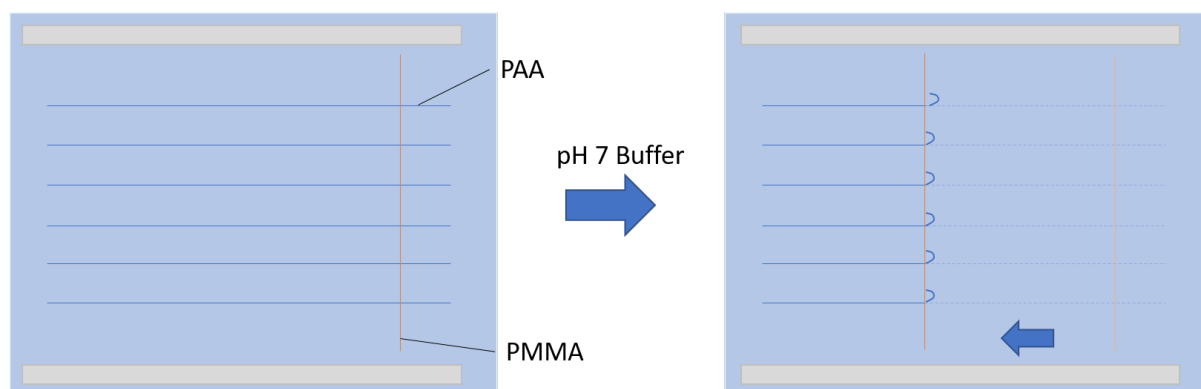


Figure 3-1: Schematic of fiber force measurement.

using **Equation 12**. The surface area of the fibers, as described in **Equation 13**, is calculated to determine the drag force (**Equation 14**) on the curling fibers. The calculated force does not take into account the low drag force.

Mass of PMMA fiber:

$$m_{PMMA} = \pi * r^2 * l * \rho \quad \text{Equation 8}$$

With radius r , length l and $\rho_{PMMA} = 1.18 \text{ g/cm}^3$

PAA fiber work to displace PMMA fiber:

$$W = m_{PMMA} * g * \Delta s \quad \text{Equation 9}$$

With distance Δs and $g = 9.81 \text{ m/s}^2$

The distance covered by PAA fibers is calculated with the following equation considering the angle α of the tilted wafer with the length l_{wafer} in respect to the microscope table:

$$\Delta s = \left(\frac{l_{wafer} * \sin(\alpha)}{l_{wafer}} \right) * (s + s_{measured}) - s_0 \quad \text{Equation 10}$$

With a measured start distance s , the actual start distance s_0 due to the angled wafer can be determined:

$$s_0 = s * \frac{l_{wafer} * \sin(\alpha)}{l_{wafer}} \quad \text{Equation 11}$$

Force generated by one PAA fiber:

$$F = \frac{W}{s_{measured}} \quad \text{Equation 12}$$

Fiber surface area for drag force

$$A = \pi r h + \pi r^2 \quad \text{Equation 13}$$

With fiber radius r and length h

Drag Force

$$F_D = \frac{1}{2} c_w * \rho * A * v^2 \quad \text{Equation 14}$$

With drag coefficient $c_w = 1.20$, $\rho = 997 \text{ kg m}^{-3}$, surface area $A = 5.7 * 10^{-7} \text{ m}^2$, velocity $v = 0.348 * 10^{-3} \text{ m s}^{-1}$

3.12. Diversion Angle & Isotropy

All videos were analyzed using MATLAB. A particle tracking plug-in for ImageJ, TrackMate, was used to track the position of particles in each video frame and measure their paths. The diversion angle was calculated by measuring the angle of the non-actuated fiber in relation to the tracked particle path after actuation. With another ImageJ plug-in, FibrilTool, the anisotropy of fibers and fibers with spheres was analyzed by selecting the tracked particle path as region of interest (ROI) (yellow). Here, a score of "0.0" indicated a purely anisotropic array, while a score of "1.0" indicated a perfectly ordered fiber movement.

3.13. Electrohydrodynamic Jet Writing of PEGDA-PAA Scaffolds

With the PEGDA-PAA hydrogel solution, stretchable scaffolds of various and complex geometries were fabricated. Therefore, the EHD jetting technique was applied, similar to the described method above in **Chapter 3.7** with a flow rate of $40 \mu\text{L h}^{-1}$. An external voltage of -1.9 kV was applied to the needles, and the collector plate was moved with a speed of 40 mm s^{-1} . The distance between the needle and the collector plate was kept constant at 0.5 cm . Scaffolds were jetted on silicon wafers, which were placed on top of the collector plate. After each layer, the scaffolds were directly crosslinked on the collector plate by covering them with a custom-built chamber. That chamber ensured the crosslinking with an

ultraviolet (UV)-lamp ($\lambda = 365$ nm) under nitrogen gas for 30 seconds. Finally, the scaffolds were lifted off the silicon wafers and mounted on 3D-printed frames for further experiments.

3.14. Scaffold Characterization

To characterize the scaffolds, bright-field images were processed with ImageJ by thresholding the images and applying “Analyze Particles” to measure the respective surface areas and fiber width. The directionality of individual fibers throughout the entire scaffold was analyzed in terms of their angle homogeneity. Therefore, the processed images were analyzed by running the plugin “Directionality Analysis” with “Fourier components” as method. The full width at half maximum (FWHM) were determined with Excel from the previously obtained data, which required the analyses of each peak. Scaffolds were cut with a razor blade and observed with the optical microscope to analyze the cross-sectional fiber area A with ImageJ by using the polygon selection.

3.15. Tensile Tests of PEGDA-PAA Scaffolds

The scaffolds were mounted on the bioreactor (TC-3F bioreactor, EBERS Medical Technology SL, Spain) for monotonic load to fracture experiments and cyclic tensile tests. For the monotonic load to fracture experiments the scaffolds were pulled in the vertical direction with a speed of 0.1 mm s^{-1} . For the cyclic tensile test, the scaffolds were stretched 1 mm at 1 Hz for 2 hours. Experiments were conducted in air and 37°C water. Tensile stress σ was obtained from the measured force F and surface area A on which the force acts with the following equation:

$$\sigma = \frac{F}{A} \quad \text{Equation 15}$$

For tensile strain ε , the proportional deformation was determined by the change in length Δl divided by the original length l_0 :

$$\varepsilon = \frac{\Delta l}{l_0} \quad \text{Equation 16}$$

The Young's modulus is defined as the ratio of tensile stress σ to tensile strain ε :

$$E = \frac{\sigma}{\varepsilon} \quad \text{Equation 17}$$

3.16. Pore Analysis

For the pore analysis of the scaffolds, a MATLAB code developed for image processing was used, which measured the height and width of each pore. The ratios of width and height were calculated with the following equation:

$$\text{Ratio} = \frac{\text{pore}_{after}}{\text{pore}_{before}} \quad \text{Equation 18}$$

3.17. Electrohydrodynamic Jet Writing of SF Fibers

EHD jetting technique was used to fabricate SF mono- and bicompartmental fibers from the respective solutions. The technique is similar to the described method above in **Chapter 3.7** with a flow rate of $10 \mu\text{L h}^{-1}$. An external voltage of $U = 1.7 \text{ kV}$ was applied to the needles, and the collector plate was moved with a speed of 40 mm s^{-1} . The distance between the needle and the collector plate was kept constant at 1.0 cm . Fibers were jetted on silicon

wafers, which were placed on top of the collector plate. Finally, the SF fibers were placed in a chamber filled with MeOH-vapor to make the fibers water-insoluble.

3.18. Raman Spectroscopy

For Raman spectroscopy, SF fiber samples were placed on a gold-coated silicon wafer. A bright-field microscope was used to observe the sample and focus the laser on the sample surface and collimation of backscattered light. A temperature stabilized diode laser $\lambda = 532$ nm and 758 nm operated at 1 mW and was used as an excitation source.

3.19. Ultraviolet-Visible (UV-Vis) Spectroscopy

The absorption of the formulations was measured with UV-vis spectrophotometer (Genesys 180) in the spectral range of 200 – 1000 nm. To measure the baseline, a cuvette was filled with Milli-Q water and used as reference. All sample formulations were diluted to a concentration of 0.01% and plotted after subtracting the reference baseline.

3.20. CD Spectroscopy

SF solutions and fibers with concentrations of 1.0 mg mL⁻¹ were analyzed by circular dichroism spectrophotometry (Jasco J-815) in the far-UV region (190 – 250 nm). Rectangular quartz cells with a 1 mm path length (1 mm QS) were loaded with the respective sample. As a control spectrum, Milli-Q water was used and subtracted from the sample spectra. Each spectrum was the average of five scans.

3.21. Tensile Tests of SF Fibers

SF fibers were cut into lengths of 5.0 cm. Each fiber was taped at the fiber ends and mounted into the Landmark® 370.10 servohydraulic test systems machine (MTS Systems GmbH, Germany) with a 5 pounds load cell. The fibers were pulled in the vertical direction with a speed of 0.01 mm s^{-1} for the monotonic load to fracture experiments. Tensile stress σ and strain ϵ , and Young's modulus are obtained from the measured force F and surface area A , as described in **Chapter 3.15**.

3.22. Light-Triggered Actuation of SF Fibers

Bicompartmental SF and graphene fibers were cut into lengths of 1.0 cm and individually glued to toothpicks for actuation experiments. The samples were then irradiated with an infrared- or a green LED laser ($\lambda_{IR} = 850 \text{ nm}$ and $\lambda_{green} = 565 \text{ nm}$) and observed under a bright-field microscope.

4. Results and Discussion

This chapter aims to highlight and discuss stimuli-responsive systems made of various materials. The first system designed and investigated is the PAA hydrogel scaffold that responds to changes in pH and is utilized to overcome challenges in current microanalytical systems. Therefore, the swelling behavior of the PAA fibers is studied. Moreover, the transport efficiencies of microspheres mimicking analyte by the reconfigurable fiber network are investigated. Another hydrogel scaffold, in this case, made of PEGDA-PAA, is mechanically stimulated to study the impact on cell differentiation. The scaffolds are characterized based on their material as well as structural properties. Therefore, the fiber homogeneity within the entire scaffold is investigated, and tensile tests are performed. Lastly, light-triggered silk fibers are presented as an actuator. Through a series of experiments, including tensile tests, we have investigated the properties and behavior of these systems in response to different stimuli. Further, the resulting data are analyzed in this chapter to gain a deeper understanding of their potential applications in various fields, such as tissue engineering and microanalytical systems. The findings of this research have important implications for developing new materials and technologies in these areas.

4.1. Biomimetic PAA Hydrogel Scaffold for Directed Transport

The leaf-closing mechanism of *Drosera capensis* L. (*Droseraceae*) inspired the PAA hydrogel scaffold and its actuation movement. Upon tactile sensation triggered by prey, such as insects, the leaves of the carnivorous plant, more specifically, the upper and more rigid cell layer, expand to a lesser extent than the other. As a result, the plant folds its long leaves around the prey to increase its contact for digestion (**Figure 4-1**). The function of this movement is similar to the one of the Venus Flytrap. Results from this chapter were already published in *Advanced Functional Materials*.^[2] M.Sc. Anke Steier developed the used PAA hydrogel ink and B.Sc. Roxana Disela performed experiments to study the ionic strength impact on swelling behavior of bicompartamental fibers.^[10] Mimicking nature's approach to actuation and inspired by the architectural inhomogeneity of the carnivorous plant's leaves, bicompartamental fibers are designed and draw their shape reconfigurability from their fiber architecture. Depositing fibers in a structured manner further enables the control of the actuation directionality, which allows a directed transport. Utilizing this actuation control allows the directed transport of placed objects. Microspheres that mimic the analyte in sample solutions were placed onto the scaffold. The fibers then transported the microspheres toward the center of the structure. This biomimetic work provides a promising platform to



Figure 4-1: *Drosera capensis* L. (*Droseraceae*). A) Before and B) after actuation entrapping an insect.^[1]

overcome challenges faced in current microanalytical systems, which suffer from mass transport limitations. Currently, none of these systems have been systematically applied in the analytical field as most of the active systems reconfigure in an undirected manner.

4.1.1. Fabrication of Bicompartamental PAA-Fibers

Analogous to the leaf's asymmetry, bicompartamental PAA fibers are created via EHD co-jetting. Therefore, two different polymer solutions were prepared by mixing 15.0% w/v PAA with EG (0.5% v/v and 20.0% v/v for compartments A and B, respectively) in Milli-Q water (**Figure 4-2A**). As reported elsewhere, EG has been used as a crosslinker for PAA.^[204] Therefore, Nie et al. incorporated EG into their electrospun PAA fibers and thermally treated them for crosslinking to improve stability in aqueous environments.^[204a] As control and to verify EG's ability as a crosslinker, PAA fibers were electrojetted without EG. The fibers were still thermally treated to confirm that crosslinking solely occurs due to EG. Then, the

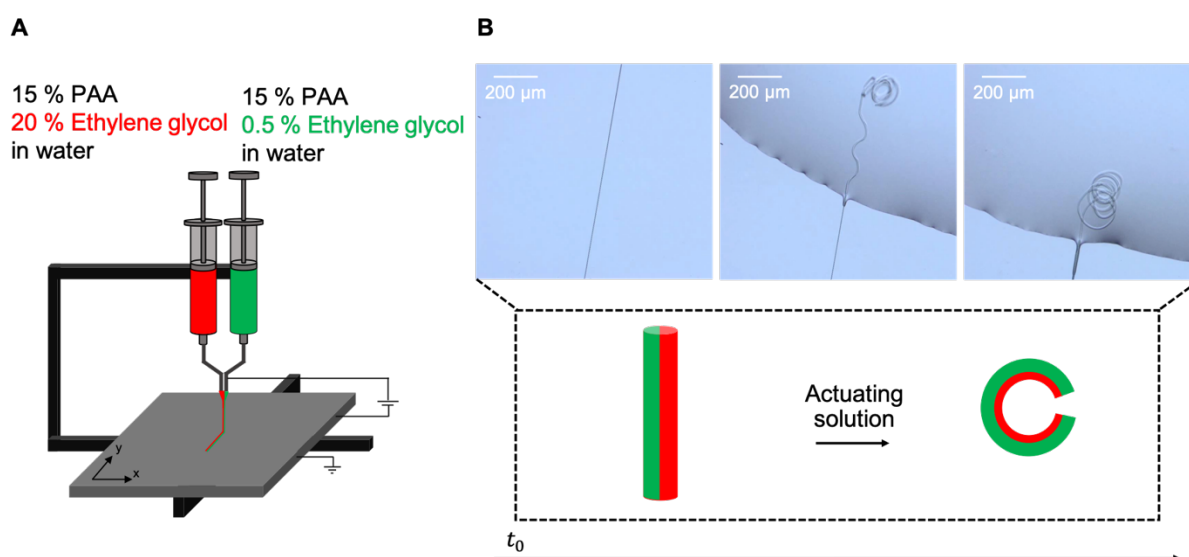


Figure 4-2: EHD Co-jet writing of pH-responsive polymer fibers. A) Schematic setup for bicompartamental fiber preparation via jet writing. **B)** Shape reconfigurability mechanism due to swelling anisotropy. Light microscopy images of actuating bicompartamental PAA fibers. Scale bar 200 μm .^[2]

fibers were immersed in water. Instantly, after immersion, those fibers without EG dissolved, verifying their ability as a crosslinker. Another control was performed to investigate the necessity of thermal crosslinking with EG. Fibers containing EG were electrojetted but not thermally crosslinked. After water immersion, those fibers also dissolved. Therefore, all fibers contained EG and were thermally crosslinked. For anisotropic swelling, however, different EG concentrations were added to each compartment so that once the fibers are crosslinked, each compartment has a different network density. This asymmetric density is responsible for the different swelling properties upon an actuating solution (pH 7.0) (**Figure 4-2B**).

CLSM was performed to confirm the bicompartamental fiber architecture. Therefore, compartment A with 20.0% v/v EG was fluorescently dyed red, while compartment B with 0.5% v/v EG was fluorescently dyed green (**Figure 4-3**). As seen in **Figure 4-3A**, both

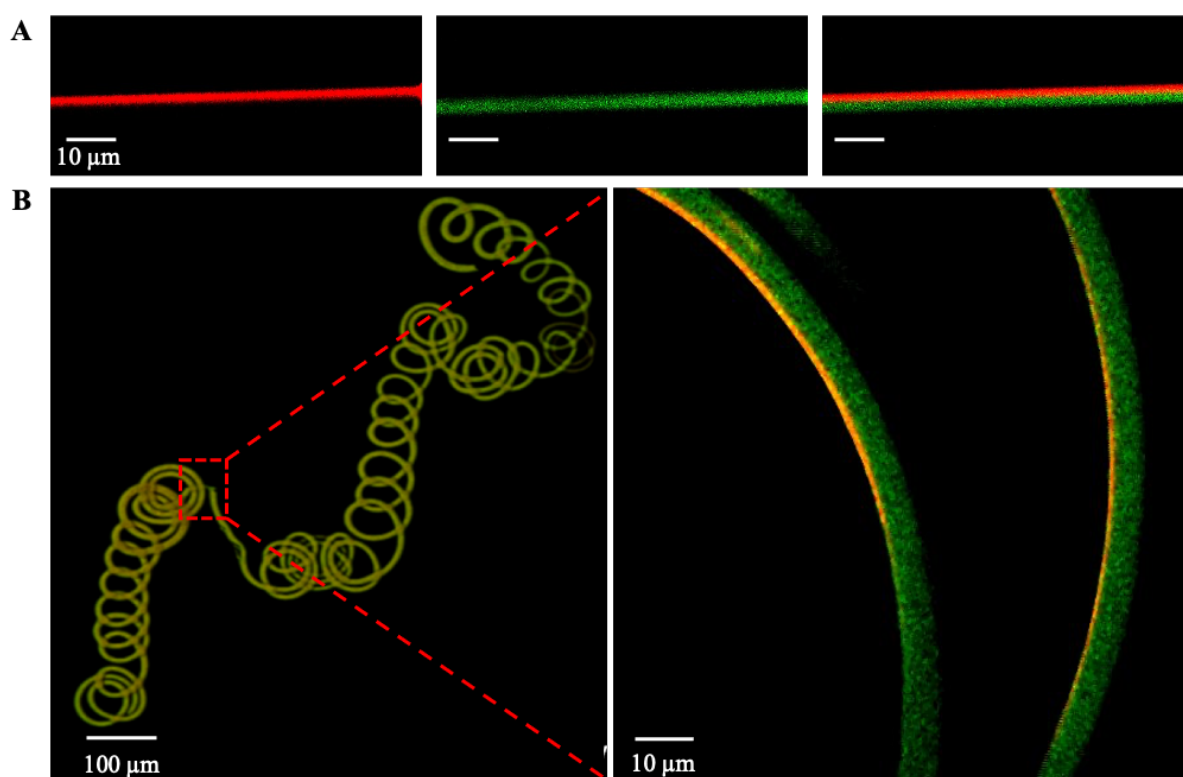


Figure 4-3: Confocal images of bicompartamental poly(acrylic acid) (PAA) fiber. In red, compartment A with 20% ethylene glycol (EG); in green, compartment B with 0.5% EG. **A)** Before actuation. Scale bar 10 μm . **B)** After actuation. Compartment B swells five times more than compartment A. Scale bar 10 and 100 μm , respectively. Adapted from ^[2]

compartments have the same width to form one uniform bicompartamental fiber with roughly 4 μm in diameter. Once the actuating solution of neutral pH is added, the bicompartamental fibers instantly swell and curl due to the anisotropic fiber architecture. CLSM images showed that the swelling of compartment B is five times higher than compartment A due to its lower crosslinking concentration (**Figure 4-3B**).

4.1.2. Swelling Characteristics

The swelling of this pH-responsive hydrogel was investigated for mono- and bicompartamental fibers. Various pH buffers ranging from 3.0 – 9.0 were screened to determine which pH induces the greatest fiber actuation, with one compartment swelling more than the other. Therefore, the swelling factor Q and curvature K were investigated. In **Figure 4-4A**, Q of mono- and bicompartamental fibers were plotted as a function of pH. Thereby Q increased with an increase in pH as the carboxylic groups of PAA were ionized above its pK_A value of 4.7.^[205] Under strong acidic conditions with citric acid buffer ($\text{pH} < 3.0$), the carboxyl groups of the polymer network are protonated, screening the electrostatic repulsion between charged acid groups. An increase in pH causes the carboxylic acid groups in the hydrogel network to lose protons and become negatively charged carboxylate ions, leading to an increased electrostatic repulsion and an overall expansion of the hydrogel.^[206] In terms of EG concentration, a higher one, like in compartment A, inhibited more significant hydrogel swelling compared to compartment B. For pH 7.0 – 9.0, three different buffer types, Trizma base ($\text{NH}_2\text{C}(\text{CH}_2\text{OH})_3$), monopotassium phosphate (KH_2PO_4), and monosodium phosphate (NaH_2PO_4), were previously tested elsewhere. In brief, the difference in swelling factors of fibers immersed in Trizma base and monosodium phosphate were less significant than fibers with monopotassium phosphate buffer. For the Trizma base buffer, the swelling factor of the lower crosslinked hydrogel was only 2.5-fold

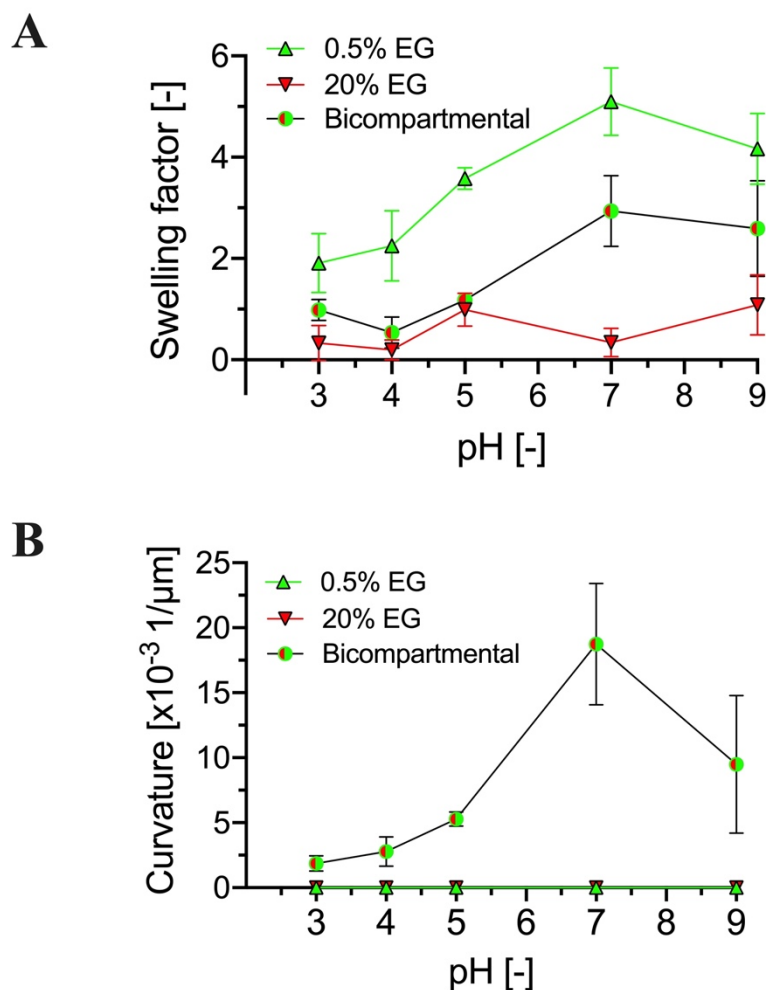


Figure 4-4: pH-dependent swelling of mono- and bicompartmental fibers. A) Swelling factor ($n = 5$ for all groups). **B)** Curvature ($n = 5$ for all groups). All data in are represented as mean \pm S.E.M. Adapted from ^[2]

higher than the hydrogel fibers with 20.0% v/v EG. The monosodium phosphate buffer induced a more significant difference in swelling factor by 4.3-fold. Nevertheless, bicompartmental fibers immersed in those two buffers did not actuate and curl significantly. The most significant swelling difference and actuation, on the other hand, was measured after immersion in monosodium phosphate buffer as monocompartmental fibers containing 0.5% v/v EG immersed in monopotassium phosphate had a swelling factor of 5.1, while the ones with 20.0% v/v EG had a lower swelling factor of 0.3, resulting in a swelling factor difference of 17-fold. Therefore, monopotassium phosphate buffer was used for further

experiments. Irrespective of the buffer type, Q reaches a plateau at pH 7.0 and further increases to pH 9.0, for instance, does not result in significant changes.^[207] Further, as mentioned above, the swelling difference is the greatest at pH 7.0, resulting in the greatest actuation with compartment B swelling five times more than compartment A. Consequently, bicompartamental fibers curl the most at pH 7.0, inducing the most significant curvature ($K = 19.0 \times 10^{-3} \text{ l } \mu\text{m}^{-1}$), as seen in **Figure 4-4B**. As a control, the bending ability of monocompartamental fibers was also evaluated. However, it was determined that these fibers could not bend. Therefore, the curvature could not be determined. The bending radius R approaching infinity and the curvature equaling zero reflect the bending inability of monocompartamental fibers, which shows the importance and necessity of bicompartamental fiber structures for bending motions.

As a next step, the circularity C and the aspect ratio (AR) of shape reconfigured fibers were determined for pH 7.0 and 9.0 to investigate the reconfigured fibers in more detail. Buffers at lower pH were neglected in these experiments because fibers were only reconfigured into circles at higher pH values. **Figure 4-5A** shows that the bicompartamental fibers reconfigured into a more circular shape ($C = 0.9 \pm 0.002$) at pH 7.0, compared to the fibers at pH 9.0 ($C = 0.84 \pm 0.03$). A circularity value of “1.0” represents a perfect circle, while values closer to “0.0” indicate a more elongated shape of an increasing polygon. Therefore, the aspect ratio, which takes the minor and major axes of reconfigured fibers into account, also gives an indication of how significant the actuation was. Similar to c , an AR value of “1.0” corresponds to a circle. In this case, however, values above and below “1.0” indicate an increasingly elongated polygon. At pH 9.0, for instance and as seen in **Figure 4-5B**, the AR value was higher ($AR = 1.29 \pm 0.11$) than at pH 7.0, which was closer to a circle ($AR = 1.07 \pm 0.03$). These observations can be attributed to the fact that the difference in swelling ratio between the PAA polymer containing 0.5% EG and the PAA polymer

containing 20.0% EG is the greatest at pH 7.0 and decreases again at higher pH values.

Taking all the results above together, the most significant and well-defined actuations were induced at pH 7.0. Therefore, all the following experiments were performed at neutral pH.

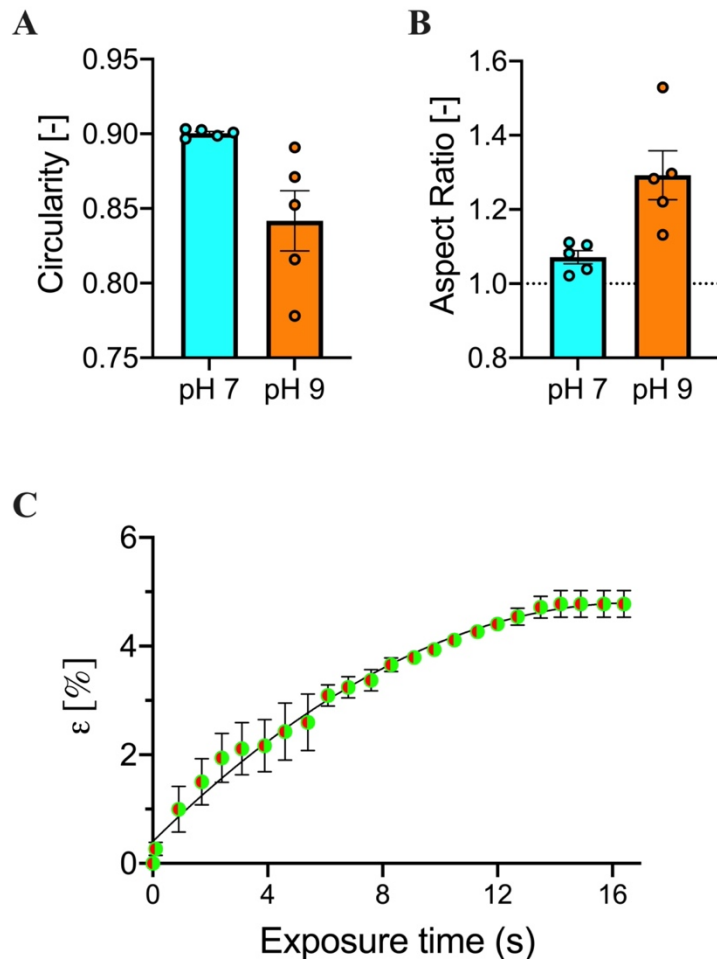


Figure 4-5: Shape reconfiguration properties of bicompartmental fibers. **A)** Circularity ($n = 5$ for all groups) and **B)** aspect ratio of reconfigured fibers ($n = 5$ for all groups). An aspect ratio value “1.0” indicates a circle, while value “0.0” is indicating an increasingly elongated polygon. **C)** Bending strain of bicompartmental fibers ($n = 5$ for all groups). All data in are represented as mean \pm S.E.M. Adapted from ^[2]

PMMA fibers of a known length and density were perpendicularly placed on bicompartmental fibers for transport to determine the force generated by the fibers. Therefore, the wafer with the fibers was placed at a 5° angle to the microscope table and the actuating solution was added. The force was calculated as followed by first determining the mass of the PMMA fiber:

$$m_{PMMA} = \pi * r^2 * l * \rho \quad \text{Equation 19}$$

With radius r , length l and $\rho_{PMMA} = 1.18 \text{ g/cm}^3$

$$m_{PMMA} = \pi * (0.0005 \text{ cm})^2 * 0.4 \text{ cm} * 1.18 \text{ g/cm}^3$$

$$m_{PMMA} = 3.7 * 10^{-7} \text{ g}$$

PAA fiber work to displace PMMA fiber:

$$W = m_{PMMA} * g * \Delta s \quad \text{Equation 20}$$

With distance Δs and $g = 9.81 \text{ m/s}^2$

The distance covered by PAA fibers is calculated with the following equation considering the 5° angle of the tilted wafer in respect to the surface:

$$\Delta s = \left(\frac{l_{wafer} * \sin(\alpha)}{l_{wafer}} \right) * (s + s_{measured}) - s_0 \quad \text{Equation 21}$$

$$s_0 = s * \frac{l_{wafer} * \sin(\alpha)}{l_{wafer}} \quad \text{Equation 22}$$

With a measured start distance $s = 15 * 10^3 \mu m$, the actual start distance s_0 due to the angled wafer can be determined:

$$s_0 = 15 * 10^3 \mu m * \frac{40 * 10^3 \mu m * \sin (5)}{40 * 10^3 \mu m}$$

$$s_0 = 1,307.3 \mu m$$

With $s_{measured} = 853.8 \mu m$, distance Δs results in:

$$\Delta s = 74.4 \mu m$$

The work one PAA fiber generates to displace a PMMA fiber is calculated with the PMMA mass $m_{PMMA} = 3.7 * 10^{-7} g$, covered distance $\Delta s = 74.4 \mu m$, $g = 9.81 m/s^2$

$$W = 3.7 * 10^{-10} kg * 9.81 \frac{m}{s^2} * 74.4 * 10^{-6} m$$

$$W = 2.7 * 10^{-13} Nm$$

Force generated by one PAA fiber:

$$F = \frac{W}{s_{measured}}$$

Equation 23

$$F = \frac{2.7 * 10^{-13} Nm}{853.8 \mu m}$$

$$F = 3.4 nN$$

Fiber surface area for drag force

$$A = \pi r h + \pi r^2$$

Equation 24

With $r = 3 * 10^{-6} m$ and $h = 60 * 10^{-3} m$, a fiber surface area of $A = 5.7 * 10^{-7} m^2$ is calculated.

Drag Force

$$F_D = \frac{1}{2} c_w * \rho * A * v^2 \quad \text{Equation 25}$$

With drag coefficient $c_w = 1.20$, $\rho = 997 \text{ kg/m}^3$, surface area $A = 5.7 * 10^{-7} \text{ m}^2$, velocity $v = 0.348 * 10^{-3} \text{ m/s}$

$$F_D = 41 \text{ pN}$$

Thus, a curling fiber in solution can generate a force of 3.4 N, as the low drag force is neglected.

Lastly, the kinetics of pH-induced curling of bicompartmental fibers was studied by measuring the strain caused by their bending motion (**Figure 4-5C**). The bending radius R of the fibers was measured at different times while they were exposed to an actuation solution, and it was found that the bending decreased as the fibers absorbed more water. It is hypothesized that this decrease in bending over immersion time is due to water saturation, which suggests that water is the driving force of the actuation. The bending strain increased exponentially over time following the relationship $1 - \exp\left(-\frac{t}{\tau}\right)$ with t as time and τ as the time constant that yielded $\tau = 0.16 \text{ s}$.

4.1.3. Directed Particle Transport

The actuation directionality of bicompartmental fibers can be controlled by depositing them in a structured manner. Therefore, the computer-assisted x-y stage moves the collector plate such that the stable polymer jet is precisely placed into a pre-programmed structure of a spiderweb network geometry. All fibers overlap at the scaffold center to create a $2.0 \times 10^{-3} \text{ cm}^2$ - sized spot. Due to the overlap of multiple fibers from various directions at one central point, the fibers actuate and reconfigure towards the scaffold geometry upon neutral

pH exposure, as that point was more stable during and after the actuation. The entire scaffold with a diameter of 1.5 cm was centrally integrated within a 2.0×2.0 cm PDMS chamber (Figure 4-6). An induced buffer exchange from pH 3.0 – pH 7.0 triggered the actuation of the fibers and can be utilized for the directed transport of randomly placed polystyrene microspheres, which mimic the analyte in a sample solution (Figure 4-7).

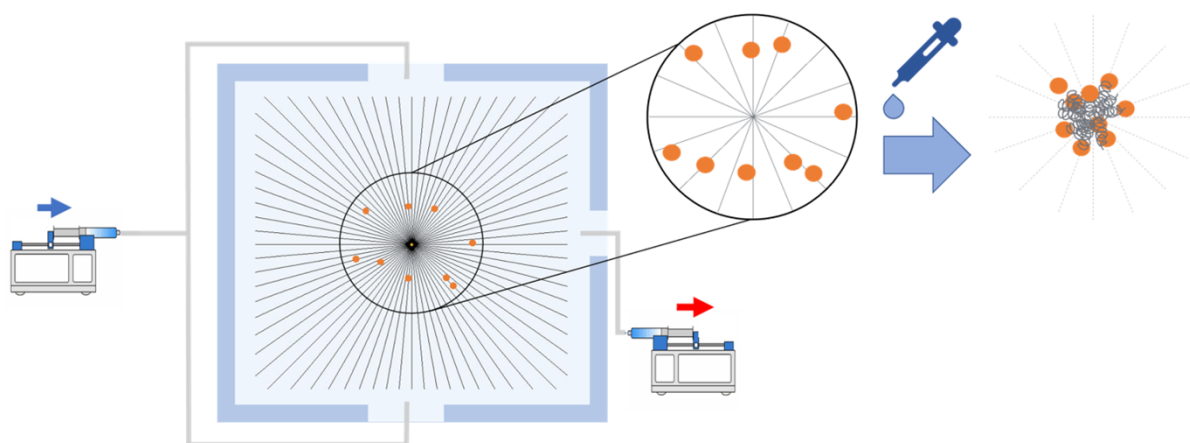


Figure 4-6: Schematic of the chamber setup for directed particle transport. Randomly placed microspheres deposited on the scaffold, which is actuated by an induced buffer exchange from pH 3.0 – pH 7.0 via syringe pumps.

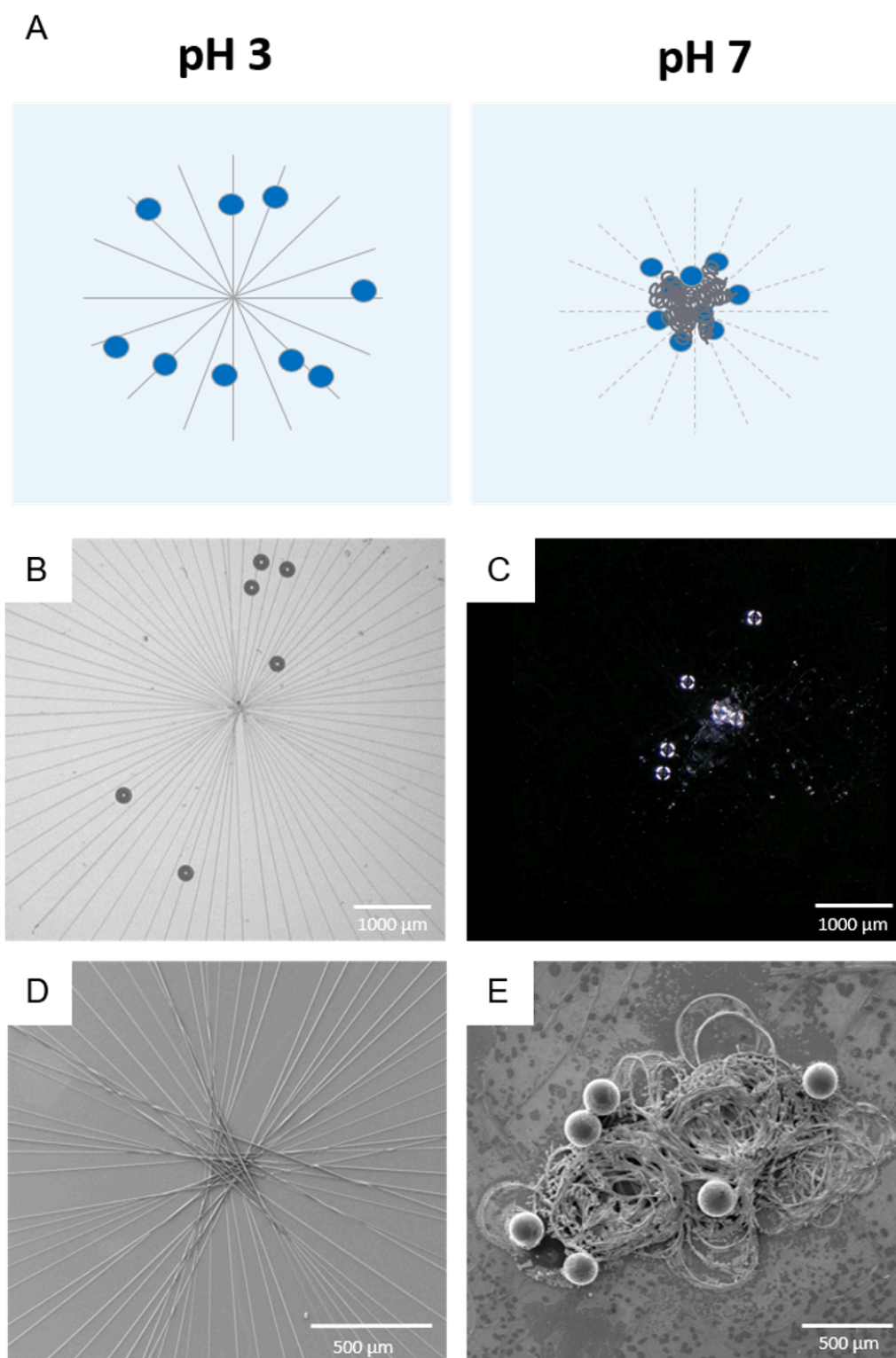


Figure 4-7: Directed transport for analyte collection. A) Schematic setup of the pH-responsive scaffolds and spheres within a chamber. Bright-field and SEM images of fiber structures and spheres before (B, D) and after (C, E) the actuation. Scale bar 1000 and 500 μm, respectively.^[2]

The analyte deposition onto the spiderweb network and its large surface area coverage of 1.77 cm^2 increased the probability of analytes settling on fibers. However, fiber reconfiguration within $t \approx 240 \text{ s}$ reduced the surface area coverage by 99% to a small sensing area of 0.02 cm^2 . The movement toward the center of the scaffold transports these randomly placed polystyrene microspheres ($d = 10 \text{ }\mu\text{m}$, $d = 50 \text{ }\mu\text{m}$, and $d = 200 \text{ }\mu\text{m}$) to a small sensing area, increasing the number of analytes detected per unit area and, thus, sensitivity. **Figure 4-8** is a qualitative representation of the relative surface area coverage of microspheres of various sizes over time. At $t = 0$, all particles were at their starting point, and thus, had a maximum distance D to the center ($D = 1$). Once the actuating solution was added, the curling fibers transported the spherical particles towards the center, resulting in a

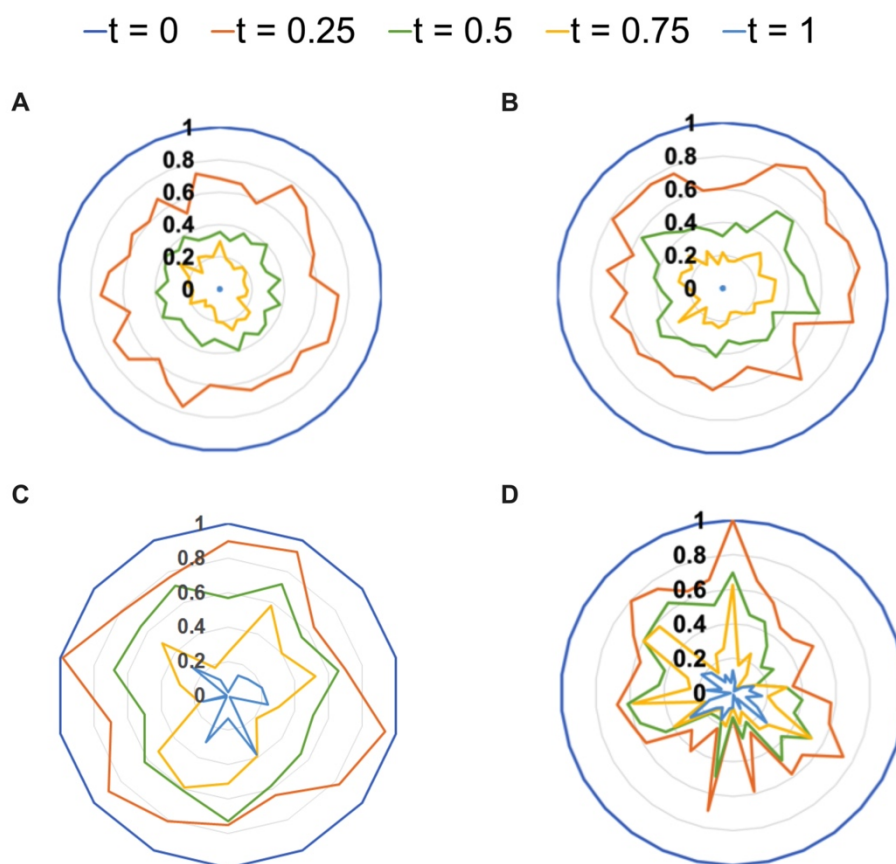


Figure 4-8: Particle Transport due to fiber reconfiguration of A) control, B) 10 μm , C) 50 μm , and D) 200 μm . Adapted from [2]

shrinking surface area. On average, the fibers transported the spherical particles 45% at $t = 0.25$, causing a 70% shrinkage in relative surface area. By $t = 1$, the surface area had decreased to just 7% of its original size. The control and transport of smaller spheres ($d = 10 \mu\text{m}$) fully reached the center of the scaffold, while larger spheres did not. More specifically, 53% and 56% of $50 \mu\text{m}$ and $200 \mu\text{m}$ spheres, respectively, were not fully transported to the scaffold center. However, a minimum relative distance of 80% was achieved by fibers with the two mentioned sphere sizes. Overall, all fibers did not uniformly transport the particles, leading to an exponential decrease (**Figure 4-9D**). The transport of $10 \mu\text{m}$ microspheres followed the same trend, but to a lesser extent. In contrast, the movement is more uniform and similar to the one of the control, showing a linear and uniform decrease.

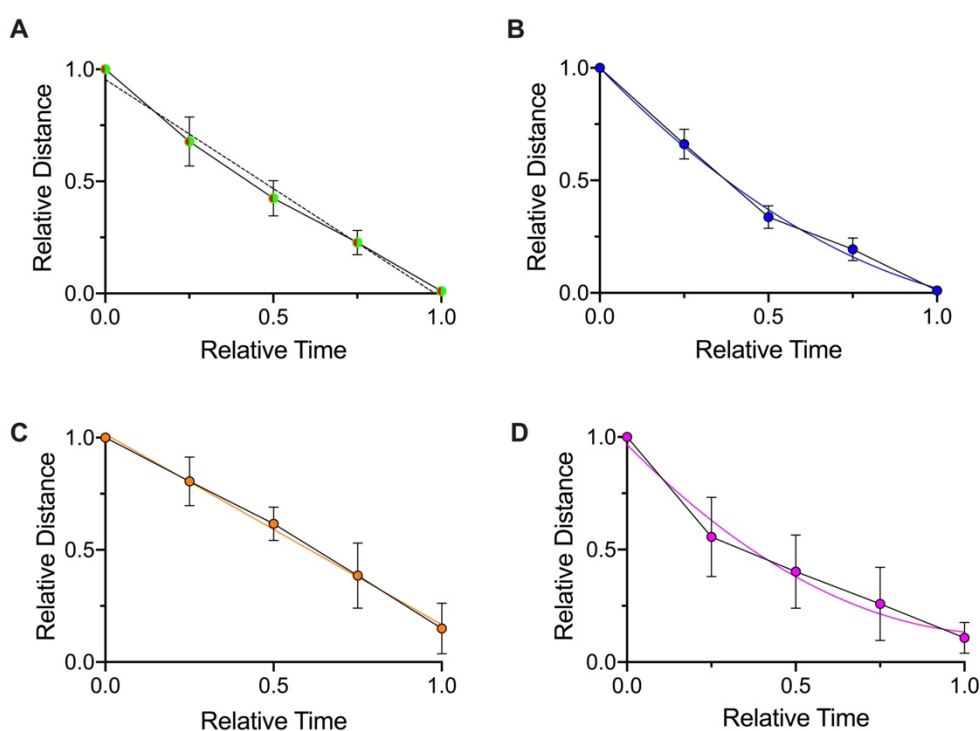
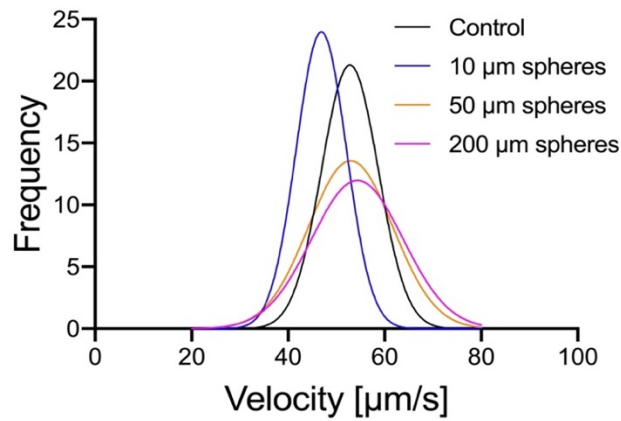


Figure 4-9: Quantitative representation of relative surface area coverage over a relative time of A) control, B) $10 \mu\text{m}$, C) $50 \mu\text{m}$, and D) $200 \mu\text{m}$ spheres. Trendline control ($y = -0.9724x + 0.9542$; $R^2 = 0.9902$), $10 \mu\text{m}$ spheres ($y = -0.9807x + 0.9318$; $R^2 = 0.9714$), $50 \mu\text{m}$ spheres ($y = -0.8486x + 1.0157$; $R^2 = 0.9973$), $200 \mu\text{m}$ spheres ($y = 0.6076x^2 - 1.4141x + 0.938$; $R^2 = 0.9821$). Adapted from [2]

The inconsistency in fiber movement with medium- and larger-sized spheres ($d = 50 \mu\text{m}$ and $d = 200 \mu\text{m}$) was supported by a wider velocity distribution, $v = 46 \pm 12 \mu\text{m s}^{-1}$ and $v = 46 \pm 9 \mu\text{m s}^{-1}$, respectively (**Figure 4-10A**). In comparison, the velocity distribution of control ($v = 47 \pm 5 \mu\text{m s}^{-1}$) and fibers with $10 \mu\text{m}$ spheres ($v = 42 \pm 5 \mu\text{m s}^{-1}$) were narrower and had a lower standard deviation. In all cases, however, reconfigurable fibers enabled a fast surface area reduction. Conventional microanalytical systems, on the other hand, without a size-reducible sensing area, suffer from inaccurate analyte detection as the probability of analyte directly reaching the small sensing area is significantly low. The impact of particles on fiber curling was further studied by examining the actuation response. Similar to the previous results, the transport of medium- and larger-sized spheres showed a sigmoidal curve, unlike the linear curve for the control and $10 \mu\text{m}$ spheres (**Figure 4-10B**). Moreover, the transport of $200 \mu\text{m}$ spheres also delayed the fiber actuation response by 23 seconds and caused more random fiber trajectories. The same applies to the transport of $50 \mu\text{m}$ spheres, which delayed the fiber actuation responds by 19 seconds.

A



	Control	10 μm spheres	50 μm spheres	200 μm spheres
Amplitude	21.30	23.98	13.56	11.98
Mean	52.79	46.87	52.95	54.34

B

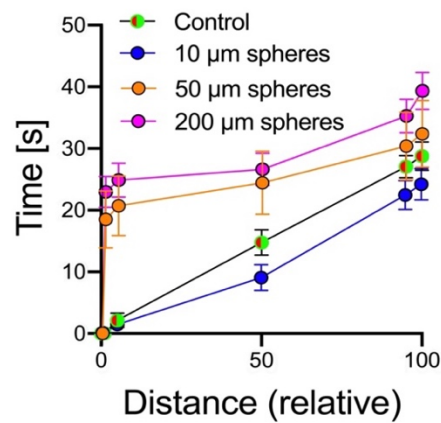


Figure 4-10: Fiber reconfiguration. A) Fiber velocity and B) Reconfiguration response of actuated fibers with 10 μm , 50 μm , 200 μm spheres, and control. Adapted from ^[2]

4.1.4. Isotropy and Diversion Angle

Fibers that transport larger spheres follow a more undirected trajectory once they reconfigure due to neutral pH. To analyze the particles impact on the fiber trajectory, the anisotropy and diversion angle of shape reconfigured fibers were analyzed. Therefore, actuation videos were pre-processed with the ImageJ plug-in 'TrackMate' prior to the analyses, as seen in **Figure 4-11A**. The isotropy of fibers with and without particles was analyzed with another ImageJ plug-in 'FibrilTool' by selecting the ROI (yellow). While an isotropy score of '0' indicates purely isotropic arrays, a score of '1' shows a perfectly ordered fiber movement. In **Figure 4-11A**, the isotropy score is shown by the arrow length. Further, as seen in the schematics of **Figure 4-11B**, the diversion angle of the initial fiber before actuation (dotted line) is measured against the fiber track after actuation (solid line). The fiber diversion angles without and with 200 μm spheres are represented in **Figure 4-12A** and **B** respectively. The red arrow represents the averaged results ($n = 30$). More specifically, the arrow length

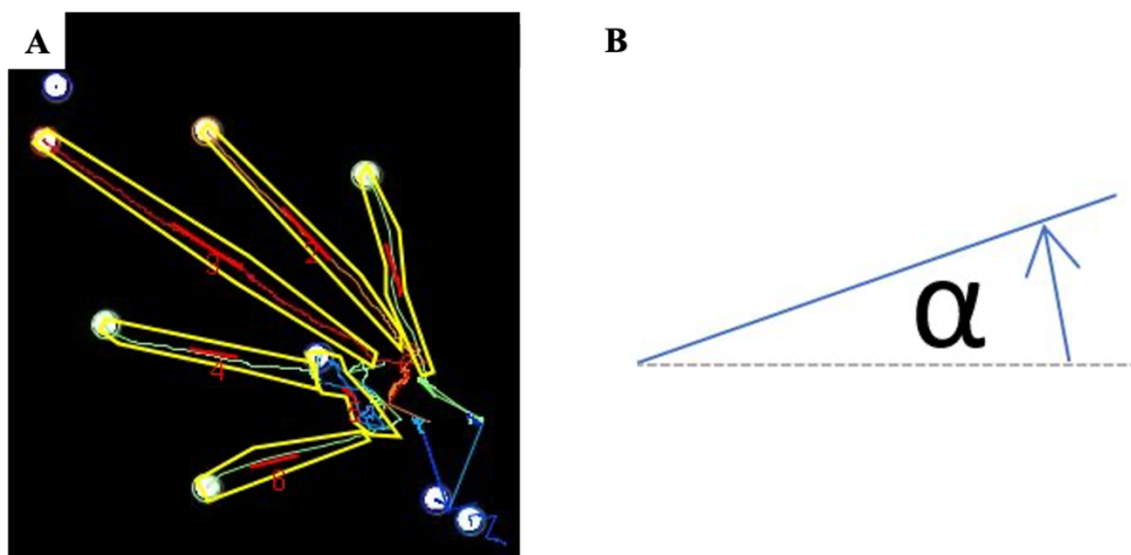


Figure 4-11: Isotropy and diversion angle measurement. **A)** ROI selected regions of post-processed images with TrackMate to measure the isotropy of fibers with particles. Red indicating the isotropy score. **B)** Schematics of the diversion angle measurement. Solid line indicating the actuated fiber path. Dotted line shows the unactuated fiber path.

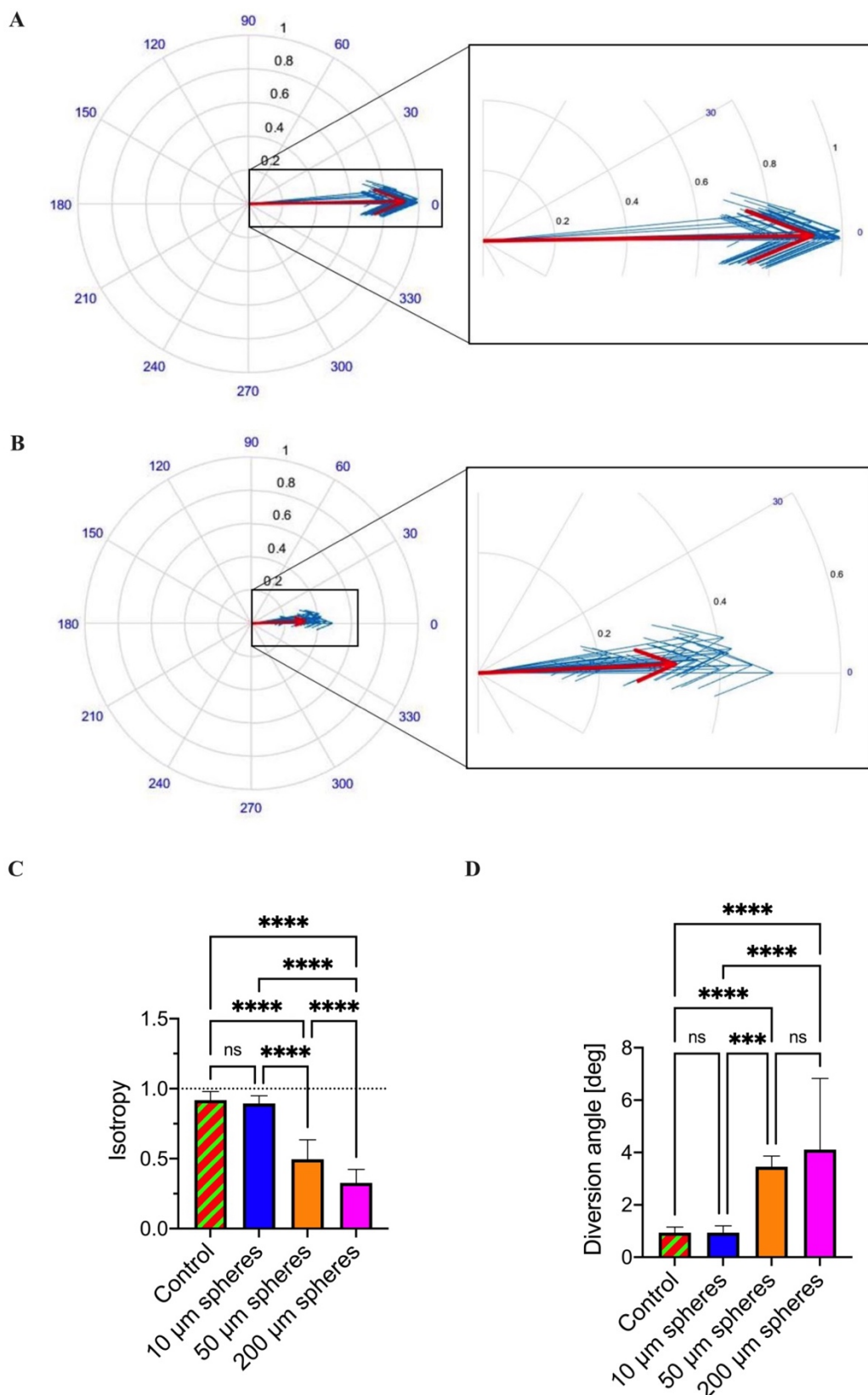


Figure 4-12: Anisotropy and diversion angle. Angular distribution of actuated fibers **A)** without spheres (n=30 for all groups) and **B)** with 200 μm spheres (n=30 for all groups). **C)** Quantitative analysis of diversion angle (n = 30 for all groups). **D)** Quantitative analysis of anisotropy (n = 30 for all groups). For (C) and (D), significant difference: ****p < 0.0001 (unpaired t-test). Adapted from [2]

indicates how isotropic the overall fiber trajectories were. The angle shows the average diversion angle. As seen in **Figure 4-12C**, fibers with 50 μm and 200 μm spheres have a significant lower isotropy score, $I = 0.5$ and $I = 0.33$, respectively, than the control ($I = 0.92$) and 10 μm spheres ($I = 0.89$). The same sphere impact can be seen with the diversion angle (**Figure 4-12D**). Again, fibers with medium- and larger sized spheres had a significant higher diversion angle ($DA = 3.46^\circ$ and $DA = 4.11^\circ$) compared to the control and fibers with 10 μm spheres, which both had the same diversion angle of $DA = 0.94^\circ$. Thus, the fiber trajectory is significantly impacted by the spherical particles.

4.1.5. Enhanced Fluorescence Signal

Based on the ability of the scaffold to directly transport and accumulate microspheres into the center, fluorescently-labeled spheres ($d = 10 \mu\text{m}$) were used to measure the increase in fluorescence signal after actuation. In the unreconfigurable state of a scaffold, the spheres were randomly placed all over the fiber network and no fluorescence was detectable (**Figure 4-13B**). Due to the wide scattering of the microspheres on the entire platform, no overlap and spatial density can be plotted in the 2D kernel density estimation plot (**Figure 4-13E**), which is based on the scatter plot (**Figure 4-13F**). Once the scaffold is triggered by neutral pH, the fibers start to transport the microspheres toward the center, where an increase in fluorescence intensity and spatial density was detected. **Figure 4-13G** and **H** show the results after the actuation that suggest that the actuation actively increased the platform's sensitivity and lowered the detection limit. The close proximity of multiple microspheres in **Figure 4-13D** enabled the detection of a fluorescence signal directly proportional to the number of microspheres present in the sample (**Figure 4-14A**). The fluorescence intensity signal below a concentration of $c = 1 \mu\text{g mL}^{-1}$ was not detectable, as

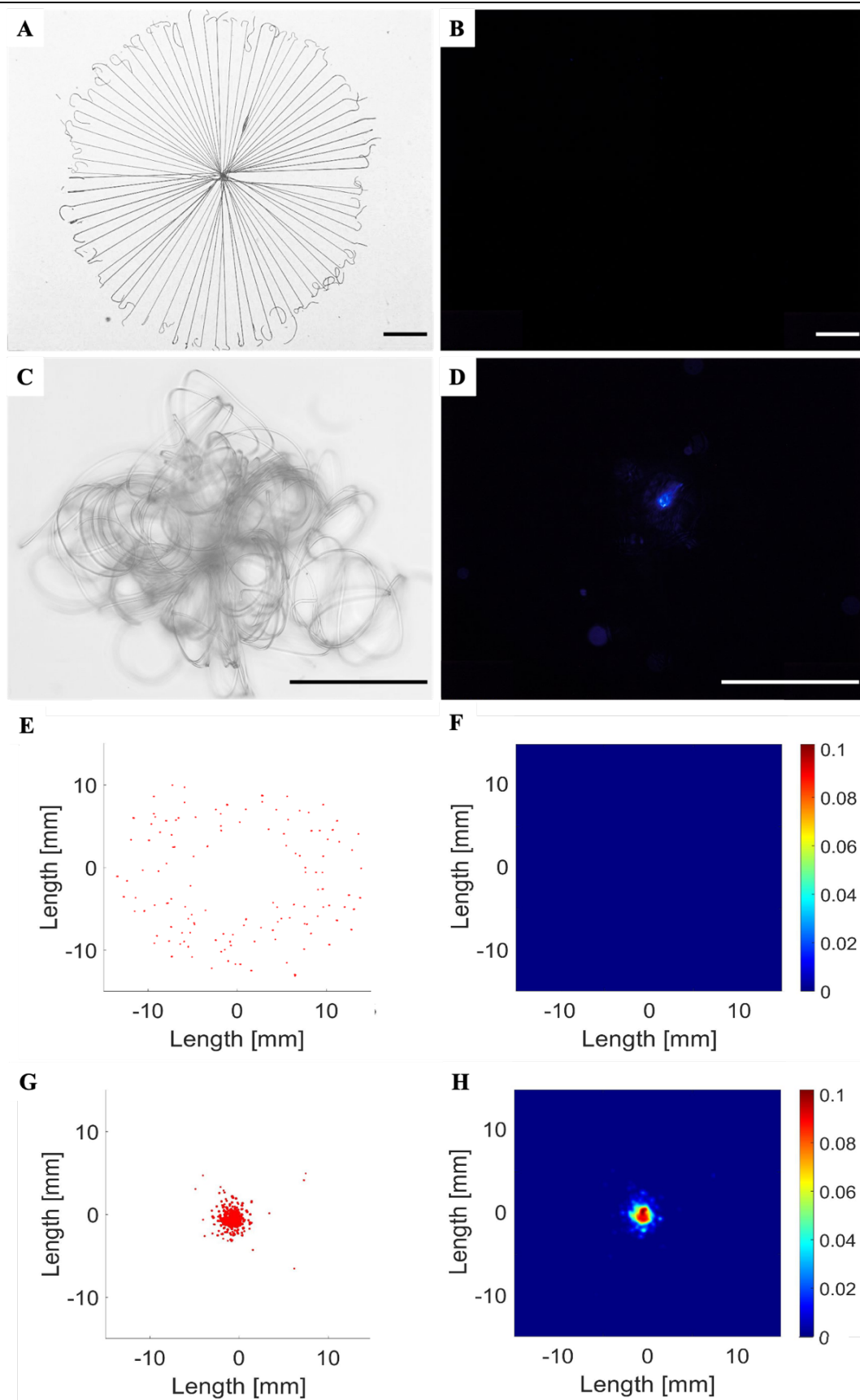


Figure 4-13: Increased fluorescence intensity due to enhanced analyte collection. A-D) Microscopy images and E-H) Scatter plots and 2D Kernel density estimation plots of 10 μm spheres before (A, B, E, F) and after (C, D, G, H) the actuation. Scale bars 20 μm . Adapted from [2]

the number of microspheres was insufficient for a detection. More microspheres within the sample, on the other hand, induce a higher fluorescence signal. However, this increase in intensity due to a large number of microspheres is limited up to a concentration of $c = 50 \mu\text{g mL}^{-1}$. The intensity signal of a concentration exceeding this limitation does not significantly differ from the intensity of $c = 50 \mu\text{g mL}^{-1}$, as the signal is saturated, reaching the maximum detectable intensity. Therefore, concentrations below $c = 1 \mu\text{g mL}^{-1}$ and above $c = 50 \mu\text{g mL}^{-1}$ are neglected for further experiments. The enhancement factor was

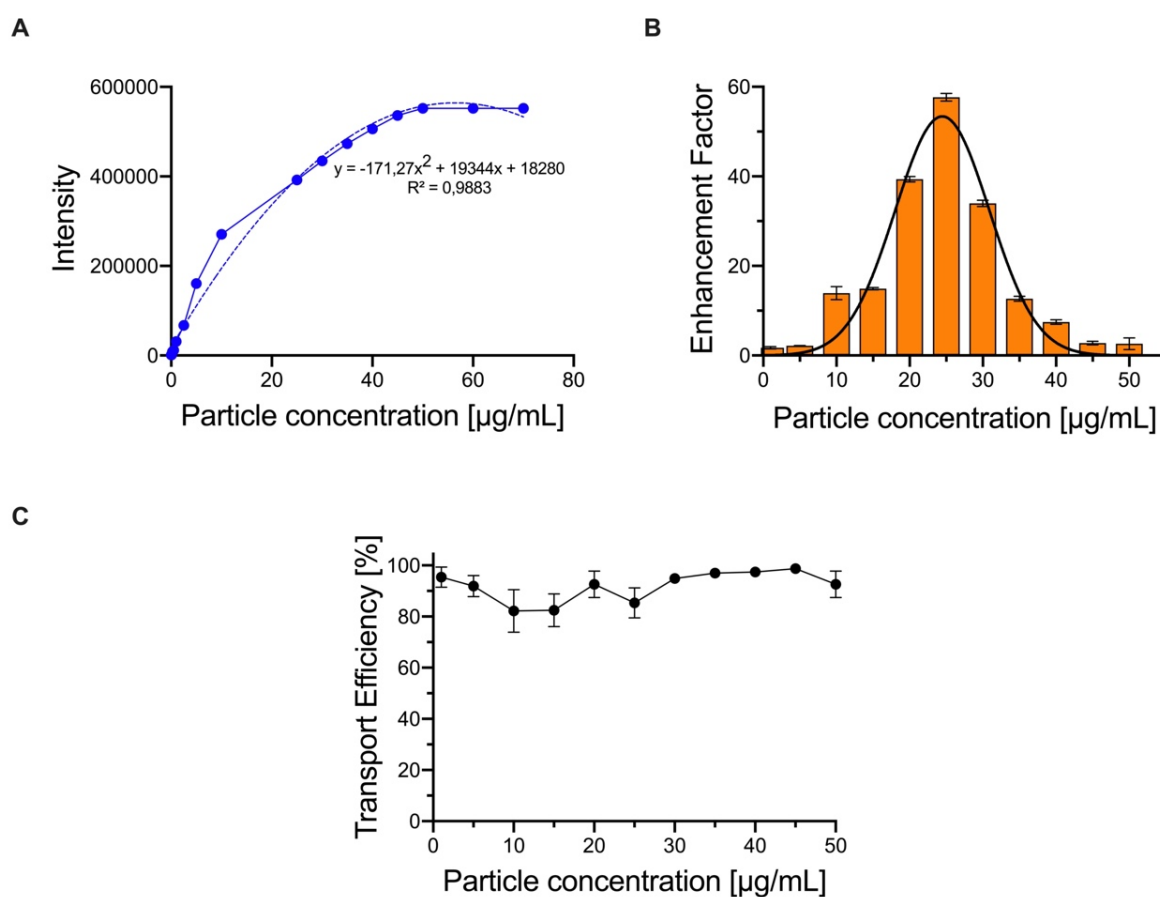


Figure 4-14: Efficiency of directed particle transport. **A)** Standard curve of fluorescence intensity signal of various particle concentrations ($c = 0.025, 0.05, 0.1, 0.25, 0.5, 1, 2.5, 5, 10, 15, 20, 25, 30, 35, 40, 45, 50, 60,$ and $70 \mu\text{g mL}^{-1}$; $n = 3$ for all groups). **B)** Fluorescence enhancement factor of spheres after actuation depending on the initial particle concentration ($c = 1, 5, 10, 15, 20, 25, 30, 35, 40, 45,$ and $50 \mu\text{g mL}^{-1}$; $n = 3$ for all groups). **C)** Scaffold transport efficiency of spheres ($n = 3$ for all groups). Data in **(B)** and **(C)** are represented as mean \pm S.E.M. Adapted from [2]

determined to analyze the analyte collection efficiency of the platform toward its center and is the ratio of fluorescence intensity signal detected after and before the direct sphere transport. **Figure 4-14B** shows the enhancement factor of various particle concentrations ($c = 1, 5, 10, 15, 20, 25, 30, 35, 40, 45,$ and $50 \mu\text{g mL}^{-1}$). The application of Gaussian distribution to fit the results are indicated in **Figure 4-14B** (Mean = $25 \mu\text{g mL}^{-1}$; amplitude = 53.4). The intensity enhancement for the lowest concentration of $c = 1 \mu\text{g mL}^{-1}$ was only 2-fold, which was the lowest ratio among all concentrations, as expected. The highest concentration ($c = 50 \mu\text{g mL}^{-1}$), on the other hand, achieved the second-lowest enhancement factor with a 5-fold intensity enhancement, as the initial intensity in the unreconfigurable state was already high. Thus, the particle collection in the scaffold center did not significantly increase the detected intensity. The greatest intensity enhancement of 57-fold was measured for $c = 25 \mu\text{g mL}^{-1}$. However, irrespective of the particle concentrations, randomly placed microspheres were transported to the sensing area with a $91.9 \pm 2.4\%$ efficiency (**Figure 4-14C**).

4.1.6. Selectivity

The selectivity of shape reconfigurable scaffolds was assessed by simultaneously placing microspheres ($d = 10 \mu\text{m}$) with different properties onto the scaffold. Sphere surfaces, which were hydrophobically coated, represent non-binding spheres. The surface of binding spheres, on the other hand, remained untreated. **Figure 4-15A, C** and **Figure 4-15B, D** present scatter and 2D kernel density estimation plots of three sample overlays with non-binding and binding spheres, respectively. It can be clearly seen in **Figure 4-15A** and **B** that fibers did not transport non-binding spheres. Moreover, it was observed that even spheres, which landed on fibers after random placement, did not get picked up. On the contrary, after the actuation those non-binding spheres remained behind and formed a torus shape. Binding spheres, on

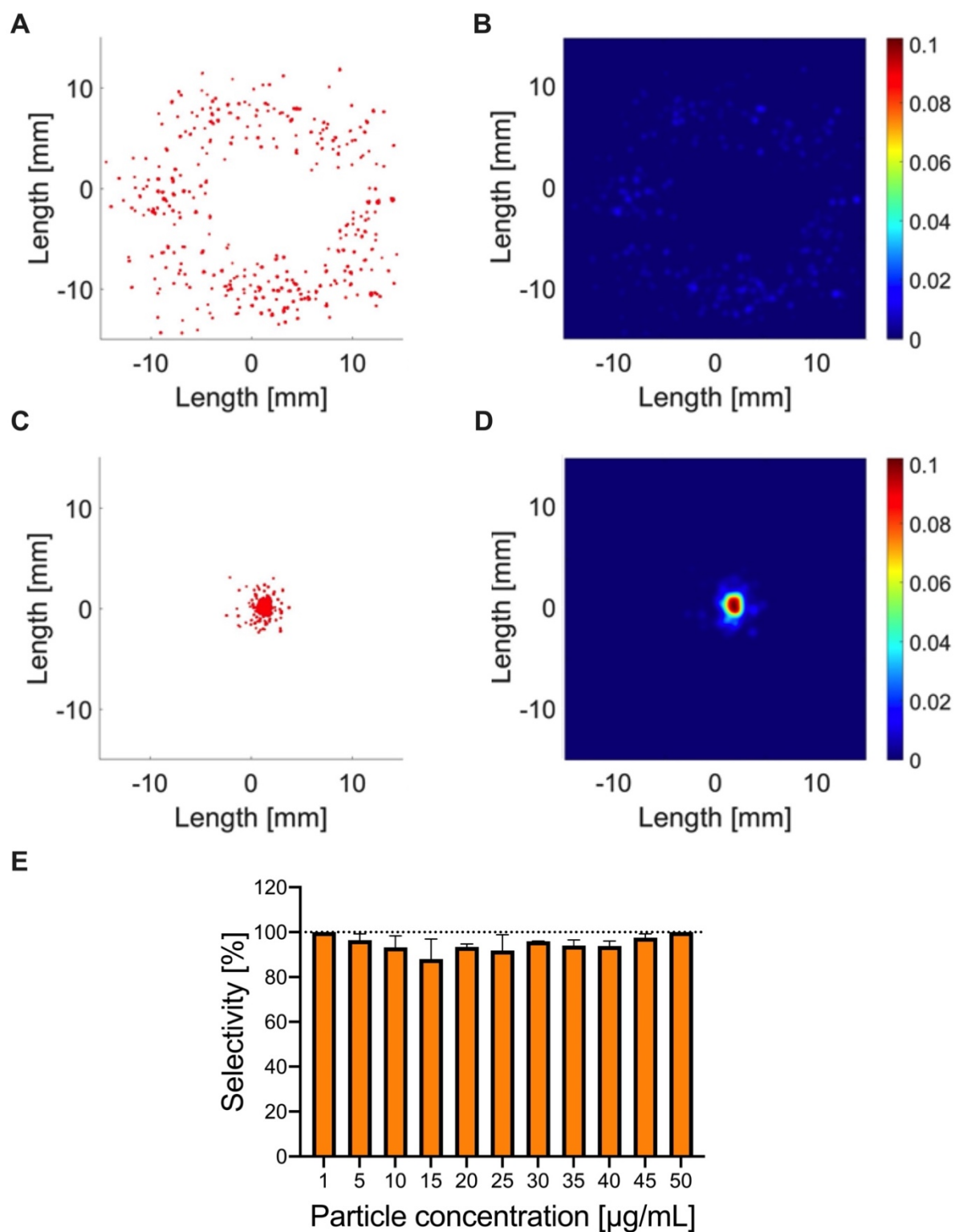


Figure 4-15: Scaffold selectivity for analyte separation. Scatter and 2D Kernel density estimation plots of non-binding (A, B) and binding (C, D) spheres. E) Selectivity of non-binding and binding spheres ($n = 3$ for all groups). Concentration of non-binding spheres remained constant ($c = 10 \mu\text{g mL}^{-1}$). Data in (E) are represented as mean \pm S.E.M.^[2]

the other hand, were all transported to the sensing area in the center of the scaffold. Various binding sphere concentrations ($c = 1, 5, 10, 15, 20, 25, 30, 35, 40, 45,$ and $50 \mu\text{g mL}^{-1}$) were screened to investigate the scaffold's selectivity. The concentration of the non-binding spheres, however, remained constant at $c = 10 \mu\text{g mL}^{-1}$. A significant separation from the non-binding spheres was achieved at all binding sphere concentrations. At a binding sphere concentration of $50 \mu\text{g mL}^{-1}$, the greatest selectivity with $98.6 \pm 2.0\%$, was achieved. On average and for all tested concentrations, separation efficiencies of $95 \pm 3\%$ were achieved.

4.1.7. Biological Application of PAA-Scaffolds

Assessing the scaffold's ability to shape reconfiguration with biological and more complex sample solutions is crucial for potential applications as a microanalytical system. Therefore, experiments were repeated in a 10% fetal bovine serum-based medium. As seen in **Figure 4-16A** and **B**, no significant impact was observed on the shape reconfigurability compared to the actuating solution. In previous experiments by the Lahann group,^[10] the effect of ionic strengths on the fiber swelling behavior was investigated. Therefore, the swelling factors were plotted over the ionic strengths, which were screened in the range of 0.224 M to 0.500 M (**Figure 4-16C**). Irrespective of the EG concentration, both polymer solutions, 0.5% w/v and 20.0% w/v EG, swelled throughout all tested ionic strengths, even if to a lesser extent, and have their maximum swelling factor at an ionic strength of 0.265 M. In general, however, the polymer solution with 0.5% w/v EG has 1.5 to 4.6-fold higher swelling factors than the one with the higher EG concentration. As blood has a lower ionic strength than the screened range, 0.15 M,^[208] it is not expected that the ionic strength of blood will negatively affect the fibers' shape reconfigurability. Thus, it is assumed that the device's function as a potential microanalytical sensor is not impacted by ionic strengths. Nonetheless, future studies will need to investigate the sensitivity and specificity of the platform in

presence of non-target proteins and other components within the sample solution for potential biosensing applications. Such complex sample solutions might impact the fiber reconfigurability and consequently the detection function, as seen in biomolecular motor-based devices, which are impacted by undiluted blood samples.^[209] Future studies should also include the immobilization of certain biomolecules onto our polymer network via CVD for specific recognition of molecules, as previously reported.^[210] Moreover, since the analysis is based on optical measurements, limitations within the optical detection and resolution can impact the platforms' read-out. Therefore, the fluorescence signal of the analyte, which is to be detected needs to be detectable by the respective optical microscope. It can be concluded that the reconfigurable spiderweb-like network has the potential to actively transport and accumulate analyte in a detection patch if the potential challenges mentioned above are studied and overcome.

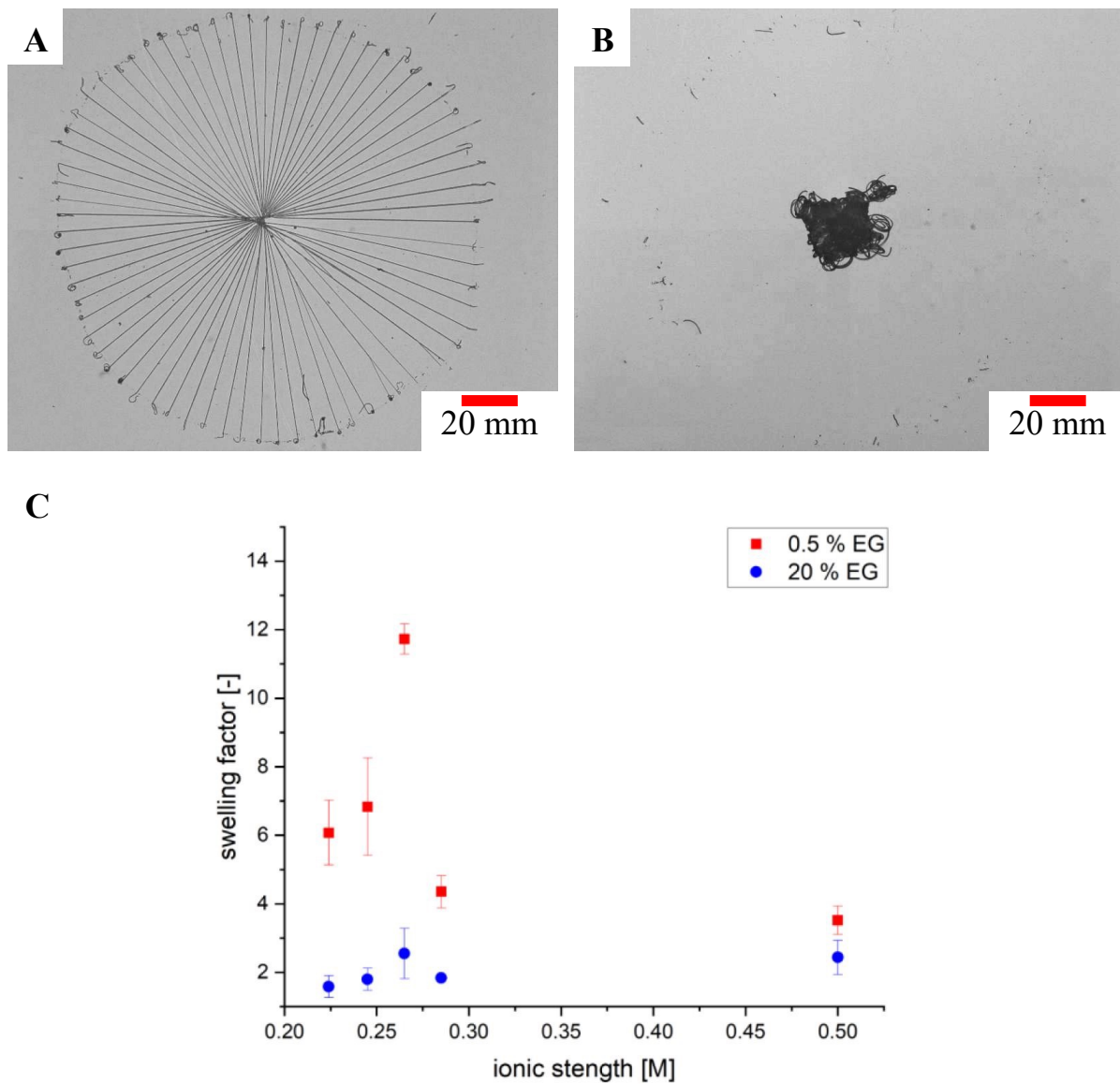


Figure 4-16: Fiber reconfigurability in complex solutions. A) before and B) after the addition of 10% fetal bovine serum-based medium. Scale bars 20 mm. Adapted from [2]
C) Ionic strength impact on swelling behavior of bicompartmental fibers.^[10]

4.2. Stretchable Hydrogel Scaffolds for Vascular Tissue Engineering

Stable and functional blood vessel networks are essential for tissue survival and their functionality, both *in vitro* and *in vivo*, as these networks provide cells with oxygen and facilitate nutrient-waste exchange.^[211] Therefore, vascular tissue engineering is an important field to consider when engineering tissues or organs.^[212] One common approach to creating vascularized tissue is co-culturing endothelial cells (ECs) and support cells (SCs), which spontaneously self-assemble into a vessel network.^[6, 213] There are two processes for blood vessel formation, i) angiogenesis, which involves the sprouting of capillaries from pre-existing blood vessels,^[214] and ii) vasculogenesis, where the capillaries assemble *in situ* from undifferentiated ECs.^[215] The basis of angiogenesis, sprouting, is regulated by various environmental factors like mechanical, biophysical, and chemical cues and can be utilized to design hierarchical vascular networks within tissues.^[216] Previous studies have shown that blood vessel organizations in mature tissue are affected by external forces.^[217] A strategy to construct vascular networks containing micro and macro vessels has been proposed by the Levenberg group, showing the influence on the sprouting behavior, which resulted in a hierarchical vascular network.^[6, 213a, 218] Further, the group has investigated factors, which govern vessel migration and orientation within 3D structures, as well as the origin location of new sprouts. Hereby, scaffold compartments with varying geometries were fabricated using SU-8 photoresist, which was crosslinked with UV light through custom-made negative masks. Various geometries, like circles, hexagons, squares, and rectangles were fabricated. The group's results suggest compartment geometry influences the vessel morphology at early stages of vascular development. Within polygonal compartments, such as hexagons and squares, for instance, new sprouting vessels connected the center of the sides of opposing corners.^[6] However, the challenge remains to control angiogenesis and sprout geometry to

mimic the complex vascular tree of living tissues as the endothelium adjusts tissue-specific phenotypes with unique architectures according to tissue needs. Moreover, the previously used SU-8 photoresist is an epoxy-based material that exhibits mechanical properties comparable to quartz.^[219] Thus, stretchable PEGDA-PAA hydrogel scaffolds are fabricated to create vascularized 3D tissues with defined vessel geometry. By applying external forces, such as static or uniaxial cyclic stretching, the combined effect of specific vessel geometries and external forces on sprout formation decisions is investigated. In this chapter, M.Sc. Marvin Klaiber supported the fabrication and mechanical tests of the PEGDA-PAA scaffolds. The cell seeding experiments were executed by M.Sc. Oryan Karni Katovich from Technion - Israel Institute of Technology.

4.2.1. Fabrication of PEGDA-PAA Hydrogel Scaffolds

Stretchable PEGDA-PAA scaffolds were fabricated using the EHD jetting procedure. Therefore, 7.5% w/v PAA was mixed with 80.0% w/v PEGDA. After homogeneous mixing, 80 μ L of 10.0% (w/v) 2-hydroxy-4'-(2-hydroxyethoxy)-2-methylpropiophenone in an ethanol and water [70:30] solution was added as a radical initiator, as described elsewhere.^[203] Scaffolds of various geometries were jetted onto the x-y controlled collector plate into pre-programmed structures, as seen in **Figure 4-17**. The scaffolds were crosslinked after each layer on the collector plate. Therefore, the entire scaffold is covered with a custom-built chamber to ensure crosslinking with a UV-lamp ($\lambda = 365$ nm) under nitrogen gas for 30 seconds. After crosslinking, more material can be deposited on the previously jetted scaffold. This process can be repeated cyclically to create a 3D scaffold. The scaffolds differ in pore size (300 and 500 μ m), geometry (square, triangle, circles, and rhombus with various angles), and height depending on how many cycles are repeated.

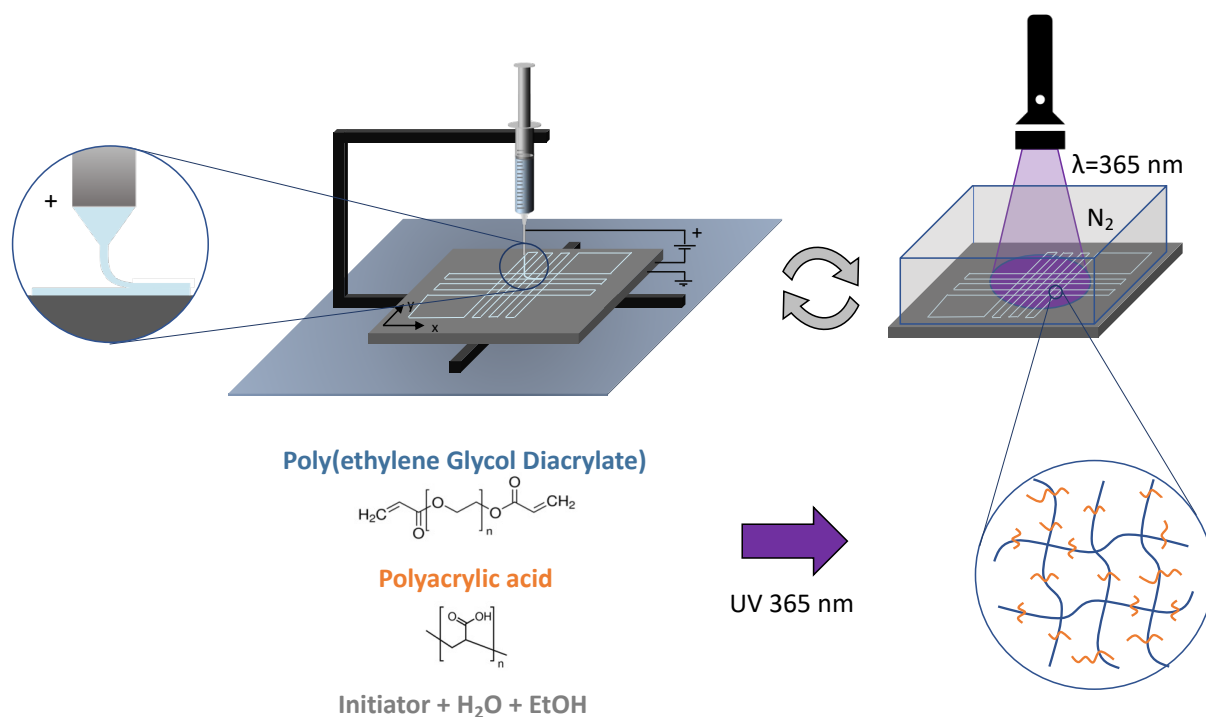


Figure 4-17: Schematics of stretchable PEGDA-PAA hydrogel scaffolds fabrication. EHD jet writing of the hydrogel ink onto the x-y controlled collector plate into pre-programmed structures. Crosslinking via UV lamp ($\lambda = 365 \text{ nm}$) under nitrogen gas. More material can be deposited on the previously jetted and crosslinked layer to create 3D structure. Steps can be repeated cyclically.

4.2.2. Characterization of Scaffold Geometries

Complex scaffold geometries were designed with DMC software, which is normally used to create laser machining designs and control laser machines. The software XY controls the collector plate mounted on x-y stages and enables precise fiber deposition into various complex structures. Scaffold squares with defined pore sizes, as used for standard tissue engineering applications, are shown in **Figure 4-18A**. The pore sizes are varied and range from 300 – 500 μm , resulting in pore surface areas of 90.000 – 250.000 μm^2 , respectively. Moreover, the orientations of the scaffold squares can be changed and tilted from 90° to 45° (**Figure 4-18B**). Other geometries, like triangles and rhombuses, are also fabricated, as seen in **Figure 4-18C-E**. For triangles, the angles are varied to create all types of isosceles

triangles, including acute, obtuse, and right ones. Changing the angular orientations of the fiber strands to create isosceles triangles, however, inherently changes the pore size of the jetted scaffold as the pore surface area of triangles is determined by the length of its base and the height perpendicular to it. Thus, changing the angle between the triangle base and height changes the height, which determines the pore surface area of the triangle. The same applies to rhombuses. A rhombus is a quadrilateral with all sides of equal length and opposite angles that are equal. The pore surface area of a rhombus is determined by multiplying the length of one of its diagonals by the length of the perpendicular drawn from one diagonal to the opposite side. Changing the angle between the diagonals changes the length of the perpendicular one, which again changes the surface area of the pore. Therefore, the pore size

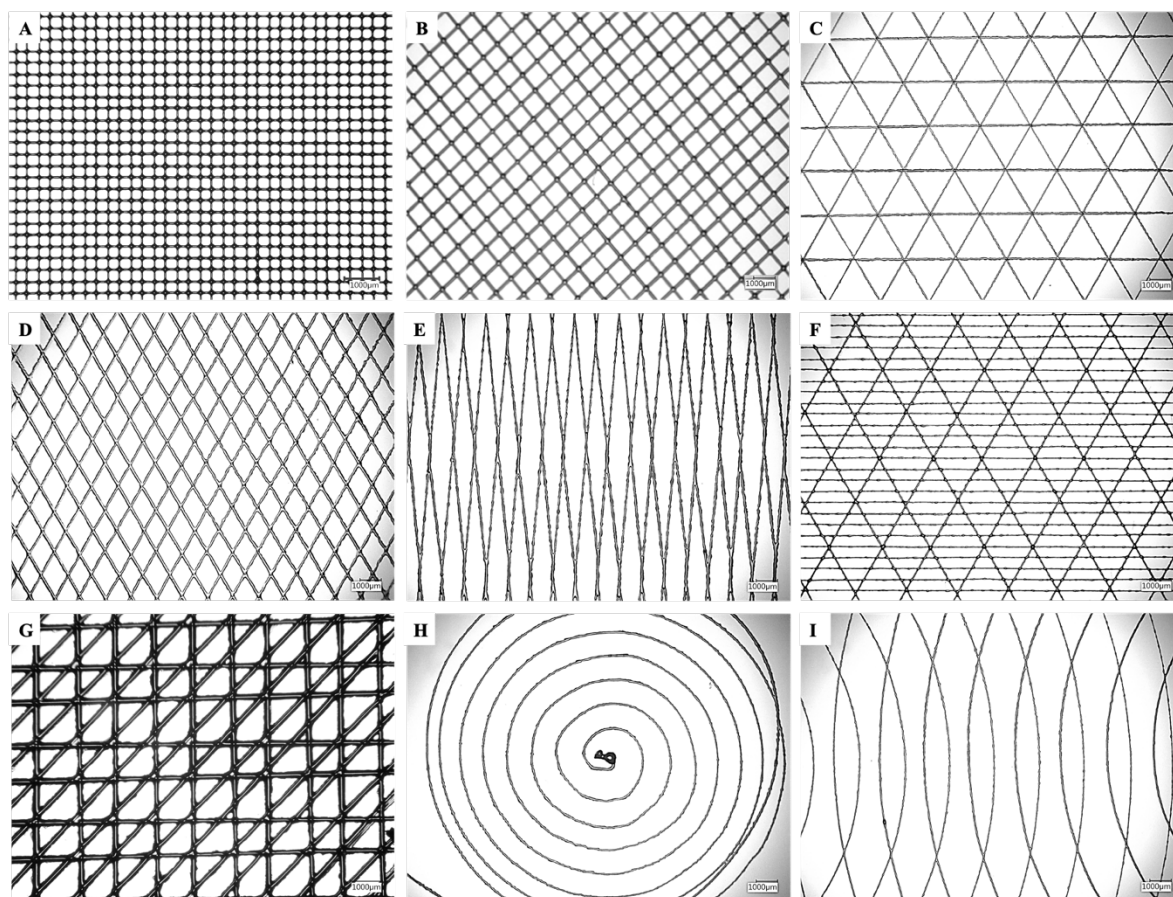


Figure 4-18: Complex scaffold geometries of PEGDA-PAA hydrogel scaffolds. A, B) Squares with 90 and 45 orientations. C) Triangles. D, E) Rhombuses with various angle combinations (60° , 120° and 10° 170° , respectively). F, G) Lines jetted across rhombus and squares, respectively. H, I) Curved structures.

of rhombuses significantly changes once the angle change from 60° and 120° to 10° and 170° , as the lengths increase by 314.9%. This significant change in lengths results in a 5.5-fold pore surface area increase of the pores. More complex geometries, in which fiber strands are jetted horizontally or diagonally across rhombuses or squares, are shown in **Figure 4-18F, G**. Moreover, curved fiber strands can be jetted to form spirals and multiple overlaid circles as both stages move simultaneously.

For three geometries, squares, triangles, and rhombuses, the homogeneity throughout the entire scaffold is analyzed in terms of fiber directionality. Therefore, the angle orientation of individual fiber strands is measured and plotted with the number of structures in a given direction over the direction angles, as seen in **Figure 4-19A-C**. Horizontal fiber strands in triangles and squares are oriented at angles of 0° . In the squared geometry, the vertical fiber strands, which are perpendicular to the horizontal ones with 0° , show angular orientations of -90° and $+90^\circ$. Fiber strands of rhombuses, on the other hand, are oriented at -60° and $+60^\circ$. As expected, scaffolds with squared and triangular pore geometries showed three distinct peaks at -90° , 0° , and $+90^\circ$, while the one with rhombuses only has two peaks at -60° and $+60^\circ$. Concerning the homogeneity, the squared scaffold geometry showed the narrowest peaks with FWHM values of -1.14 ± 0.02 and thus highest peak values up to 0.11. Scaffold geometries with isosceles triangles and rhombuses with 60° and 120° , on the other hand, had almost 2- to 3-fold lower values with 0.06 and 0.04, respectively. Accordingly, both geometries have wider FWHM values. While triangles have FWHM values of 2.75 ± 0.2 , rhombuses have the highest values with FWHM = -6.84 ± 1.03 , indicating that this scaffold geometry shows the most irregularities compared to the other two. Due to the order of the fiber strand displacement and the irregular fiber lengths, as seen in **Figure 4-19D-F**, rhombuses have a 6-fold higher value than squares. All fiber strands of the scaffold with the squared pore geometries have the same lengths because the respective fiber strands are

parallel to the entire scaffold geometry. However, fibers that are not deposited parallel to the entire scaffold, like in a triangle and rhombus geometry, result in different lengths leading to asymmetrical pores. This asymmetry is particularly evident at the scaffold edges, as the shortest fiber length within the same scaffold can be 8-fold shorter than the longest diagonal fiber, impacting the directionality. The fiber strand jetting orders S1, S2, and S3 are indicated by arrows and color-coded in **Figure 4-19D-F**. Here, blue is the first jetted strand, followed by red and yellow, whereby the latter, S3, only applies to the triangle geometry. The fiber strand diameters of complex geometries were compared after one jetting cycle *c* (**Figure 4-19G**). Moreover, the impact of the strand jetting order is analyzed. The squared geometry shows the thinnest and most homogeneous fibers with average widths of $w = 63.82 \pm 1.61 \mu\text{m}$. Scaffolds with triangles, on the other hand, show the most inhomogeneous fibers with the highest standard deviations of all geometries ($w = 119.87 \pm 24.06 \mu\text{m}$). Even excluding the last fiber strand S3, the standard deviation remains the largest compared to the others ($w = 107.46 \pm 19.84 \mu\text{m}$). Rhombuses, in contrast, have the largest fiber widths with an average of $w = 163.55 \pm 16.12 \mu\text{m}$. Comparing each strand within a geometry itself, the squares and rhombuses show no significant differences between S1 and S2, while for the triangles, two significant differences can be seen between S1 and S2 and between S1 and S3. Since the square geometry showed the best results in terms of fiber homogeneity and width, square-shaped scaffolds were fabricated with five and ten repeated cycles. **Figure 4-19H** compares the fiber strand widths S1 and S2 of the square geometry after one, five, and ten cycles. As mentioned above, no significant difference can be seen between the two fiber strands after one jetting cycle. The same applies to strand widths after five cycles, which are almost 2-fold wider than the ones after one jetting cycle. The fiber width increases from five to ten jetting cycles however, then only shows a 1.3- to 1.1-fold wider strand for S1 and S2. After ten cycles, significant differences can be seen

between S1 and S2, with $w = 154.23 \pm 10.99 \mu\text{m}$ and $w = 127.27 \pm 2.12 \mu\text{m}$, respectively. Moreover, the first strands after five and ten cycles are wider than the respective second strands, as the latter strands are immediately crosslinked once jetted. Contrary to the first crosslinked. This width difference seems to increase with the number of cycles since the effect is not yet seen after one jetting cycle strands, which have more time to flatten on the surface before the entire scaffold is crosslinked. This width difference seems to increase with the number of cycles since the effect is not yet seen after one jetting cycle.

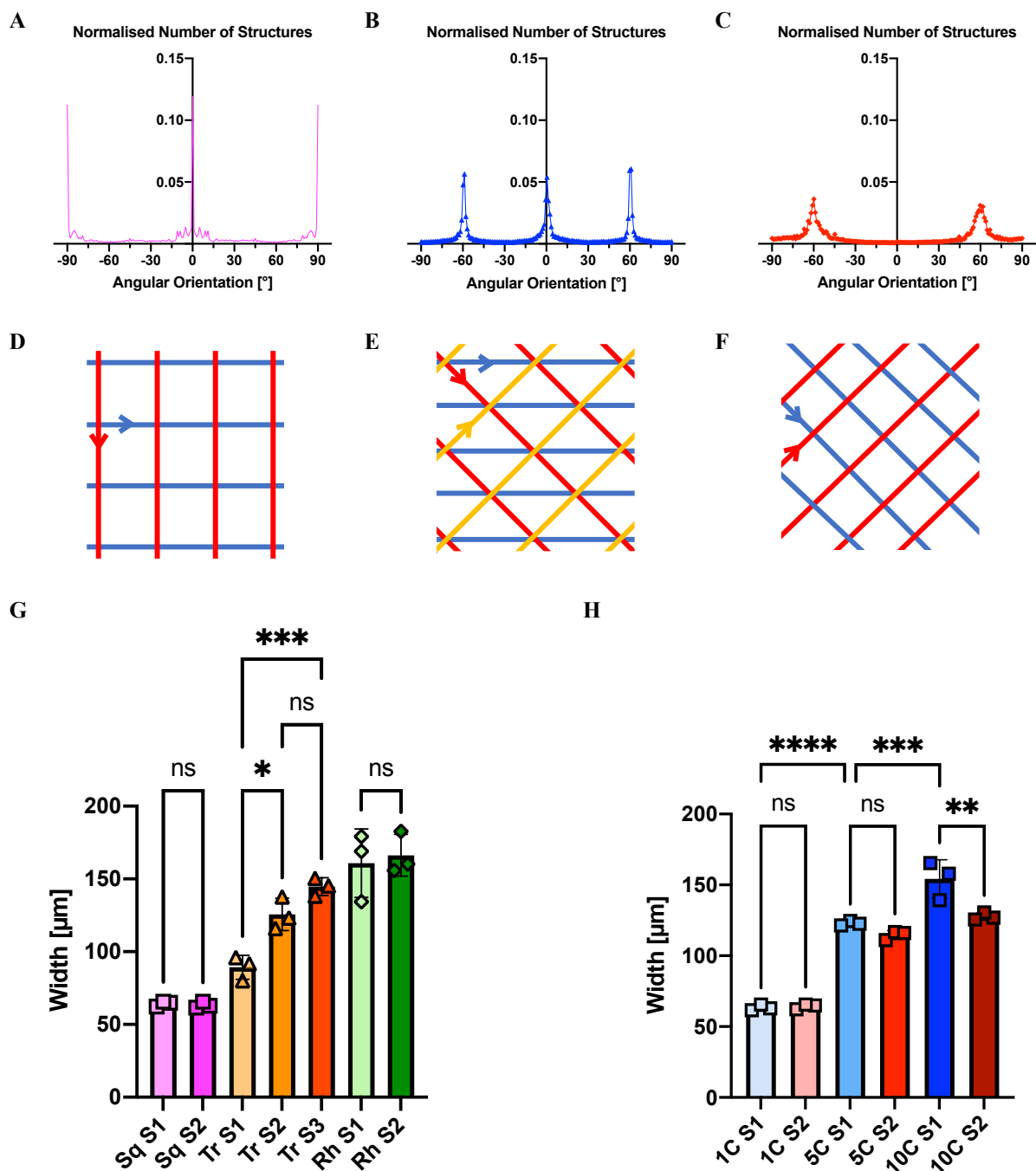


Figure 4-19: Scaffold characterization. Homogeneity of fiber directionality and fiber strand jetting order for **A, D**) squares, **B, E**) triangles, and **C, F**) rhombuses. Color-coded jetting order with blue being the first fiber strand jetted (S1), followed by red (S2), and yellow (S3). Fiber width analysis impacted by jetting order of **G**) various geometries after one cycle and **H**) squares after one, five, and ten cycles c.

4.2.3. Tensile Tests of PEGDA-PAA Scaffolds

Mechanical stimulations are known to influence vascular differentiation.^[220] Hence, studying and understanding the impact of mechanical stimulation is crucial for vascular tissue engineering purposes. Static or uniaxial cyclic stretching were applied to test and investigate the hydrogel scaffold's stretchability. Mechanical experiments were performed on scaffolds with square geometry due to their fiber strand homogeneity throughout the scaffold. Tensile tests were conducted in a bioreactor, as seen in **Figure 4-20A**. For easier handling of the scaffolds to clamp them into the bioreactor, the hydrogel scaffolds were sandwiched between two 3D-printed frames. The frame, which further ensured a uniform force transfer onto the scaffold, was then clamped into the setup. First, stress-to-failure tests were conducted. Therefore, a scaffold was mounted in the bioreactor, and a uniaxial force was applied, stretching the scaffold upwards. The scaffolds were both tested in air and 37°C water.

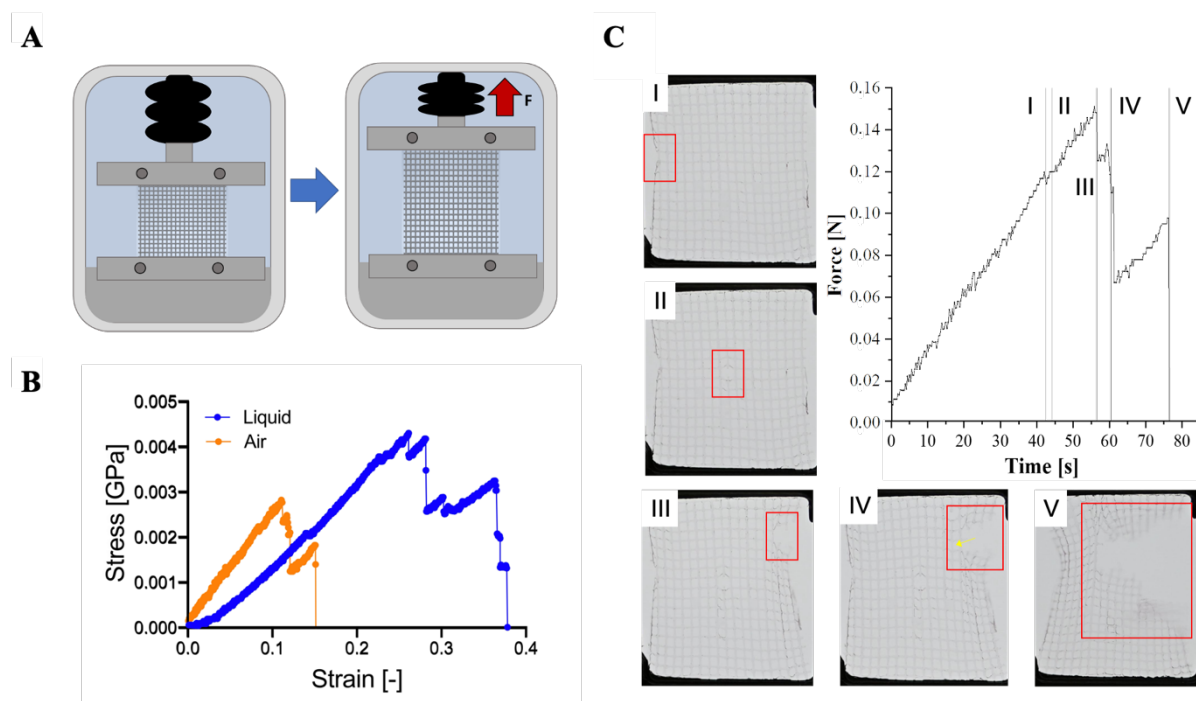


Figure 4-20: Mechanical stimulation of hydrogel scaffolds. A) Schematic setup of tensile test. B) Stress-strain curves of scaffolds stretched in air or liquid ($n = 5$ for all groups). C) Failure analysis and impact of individual failure points on force on a hydrogel scaffold in liquid.

Scaffolds after one, five, and ten cycles were tested. However, only scaffolds after five cycles could be analyzed, as the other two scaffold types immediately broke without data output. Scaffolds in liquid noticeably break after a strain of $\varepsilon = 0.26 \pm 0.03$ and reach stress values of $\sigma = 0.004 \pm 0.001$ GPa (**Figure 4-20B**). The Young's modulus for these scaffolds is $E = 0.017 \pm 0.005$ GPa, comparable to values measured for tendons and skin.^[221] In the air medium, on the other hand, scaffolds tear earlier after $\varepsilon = 0.11 \pm 0.08$ and only reach 66% of the stress values, which scaffolds in liquid can resist. Consequently, these scaffolds have a 41.2% higher Young's modulus of $E = 0.024 \pm 0.009$ GPa than the ones in liquid. Moreover, scaffolds in the air medium tear within $t = 32.5 \pm 21.5$ s and in two stages, as seen by the force drops. In contrast, scaffolds in the liquid medium tear in five stages and last 2.2 times longer ($t = 72.5 \pm 4.8$ s), which is expected since the hydrogels remain fully hydrated. In the air medium, scaffolds started to dry causing microfractures that represented a weak spot for the external force that was applied for the monotonic load to fracture experiments. Further, the scaffold dried irregularly, resulting in high tear variations between the tested scaffolds, as seen by the high standard deviation of the fracture time for scaffolds in the air. **Figure 4-20C** presents the force drops of one scaffold after five jetting cycles uniaxially stretched in a liquid medium. The images show the respective scaffold failures indicated by the numbers I-V. The first failure, failure I, is a tear of one vertical strand. The strand breakage is in the direction of the applied force. Located in the middle and on the outer left side of the scaffold, failure I does not significantly affect the measured force, as the force only drops by 0.005 N. The tear type of failure II is similar to the first one and appears in the middle of the scaffold. However, the tear of failure II does not impact the stability of the scaffold, as no change in force is measured. In contrast to the tear of failure III, which results in a force drop of 0.02 N. The four-fold higher force drop compared to failure I is due to the simultaneous breakage of three vertical strands. Based on the created weak point, failure IV continues the breakage by

expanding the tear into the vertical direction of the applied force. Tearing a second scaffold row, as indicated by the arrow, results in a stress drop of 0.07 N. The last and most significant tear that completely breaks the scaffold is failure V, which reduces the stress by 0.10 N until the force drops to zero. Applying an external force in the vertical direction of the scaffold does not only change the entire scaffold dimension but also inherently each pore. The dimensional change of individual pores was investigated by assessing the ratio of width and height changes. Therefore, images were processed with a written code in Matlab, as seen in **Figure 4-21A**. First, the original image was transformed into a binary one to remove unevenness and light effects, which can interfere with the analysis and lead to false measurements. Pseudo-coloring then gives an indication of the quality of the binary image as individual pores are highlighted in various colors. Pores, which strand is not fully closed due to imaging flaws will be seen as bigger pores as two individual pores are detected as one.

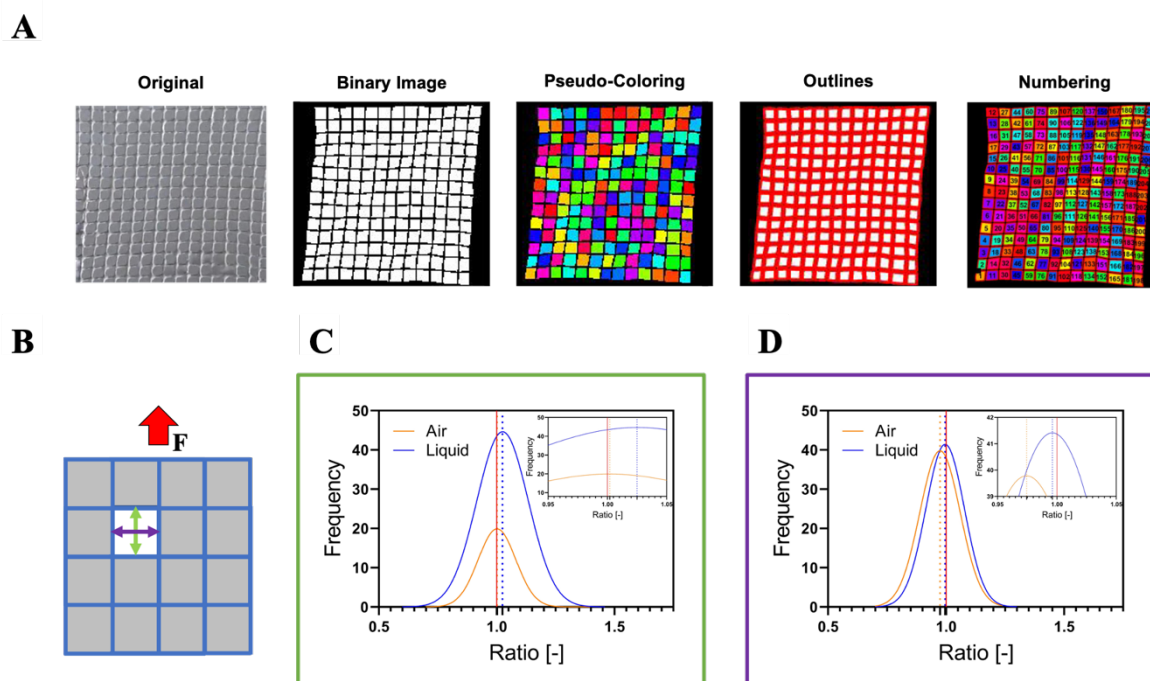


Figure 4-21: Pore size distribution of stretched scaffolds with square geometry. A) Stepwise image analysis via Matlab to obtain individual pore size dimensions. B) Schematics of pore change induced by a vertical force. Green arrow shows change in height. Purple arrow shows width change. C) Height and D) width ratio of individual pores ($n = 4$ for all groups).

After outlining the individual pores, the pores are numbered in the final step with an output of their respective dimensions. The change in height and width is determined by a ratio of the respective pore dimensions before and after the applied force. As seen in **Figure 4-21C**, the height of the pores in the liquid medium increases due to the vertical force and results in a ratio of 1.03 ± 0.11 , while the scaffolds in the air medium have a ratio of 1.00 ± 0.08 . A ratio of “1.0” indicates no change in the pore dimensions after applying the external force. Pores, which size increases after mechanical stimulation result in ratios above “1.0”. Accordingly, the ratio is below “1.0” when the pore size is smaller after stretching compared to no stimulus, like the width ratios of pores, in both media, air, and liquid. In the latter medium, the pores do not significantly become narrower, as the ratio is 1.00 ± 0.08 . In the air medium, on the other hand, the ratio decreases to 0.97 ± 0.08 . Scaffolds in the air medium become stiffer and less stretchable, which is seen by the height pore ratio. The vertical strands do not stretch with the applied force, resulting in insignificant changes in height dimensions. Instead, changes in the width dimensions are more evident.

Uniaxial cyclic stretching of the hydrogel scaffolds was performed in the air and liquid medium to further characterize the hydrogel’s stretchability over long mechanical stimulations. Therefore, the scaffolds were stretched at a frequency of 1 Hz over a distance of 1 mm for 2 hours. The frequency and liquid temperature of 37°C were chosen to closely mimic physiological conditions as cells *in vivo* are constantly exposed to pulsatile shear and tensile stresses.^[222] Research, including cardiac but also endothelial cells, often use a frequency of 1 Hz to stimulate the cells.^[222-223] **Figure 4-22** shows the force measurements of scaffolds, which were stimulated by uniaxial cyclic stretching. For both media types, the scaffolds run through 7,274 stretching cycles. Scaffolds in the liquid medium even out after 3,000 cycles and remain intact until the end of the experiment. Before reaching 3,000 cycles, force measurements are irregular due to inaccurate pre-stretching, which normally keeps the

entire scaffold under tension for full force transfer onto the scaffold. In the air medium, on the other hand, two clearly visible force drops can be seen at cycle 752, and between cycle 2,000 and 3,000 (**Figure 4-22B**). These drops indicate that scaffolds in the air medium tear during the cyclic tests. The results correspond to the previous ones from the monotonic to fracture experiments, which suggest that scaffolds dry in air, leading to reduced stretchability and increased weak points.

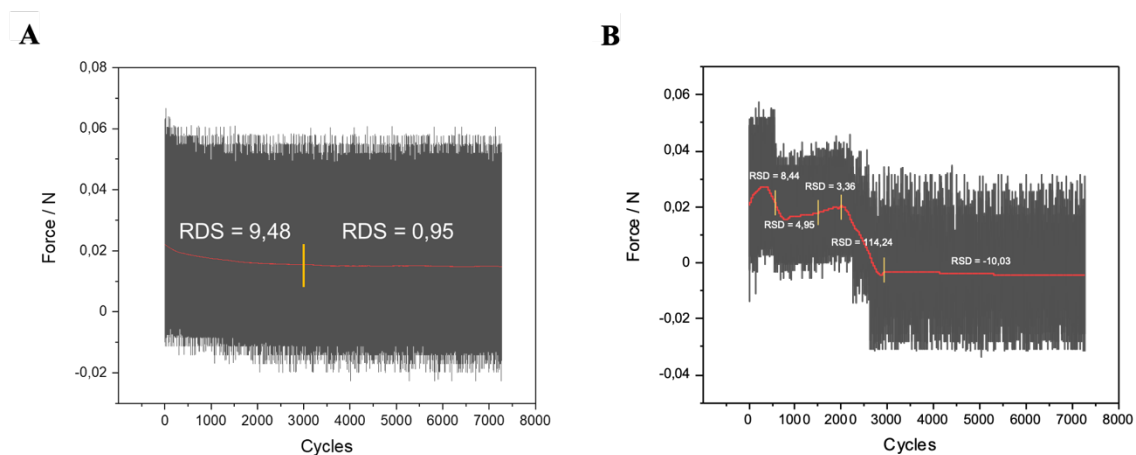


Figure 4-22: Force measurements of cyclic tests in E) liquid and F) air with relative standard deviation (RSD). Scaffolds in both media run through 7,274 stretching cycles. In liquid, the scaffolds remain intact until the end of the experiments, while in the air medium, the scaffolds tear, as seen in the visible force drops.

4.2.4. Cell Culture

To assess the impact of mechanical stimulation on cells for vascular tissue engineering, endothelial cells, and support cells were co-cultured on the PEGDA-PAA hydrogel scaffolds. In collaboration with the Levenberg group, human adipose microvascular endothelial cells (HAMECs) and dental pulp stem cells (DPSCs) were seeded onto the square geometry scaffolds, whereby the latter were used as support cells. Co-culturing two cell types has the advantage that these cell types release signaling molecules, which promote tubulogenesis and

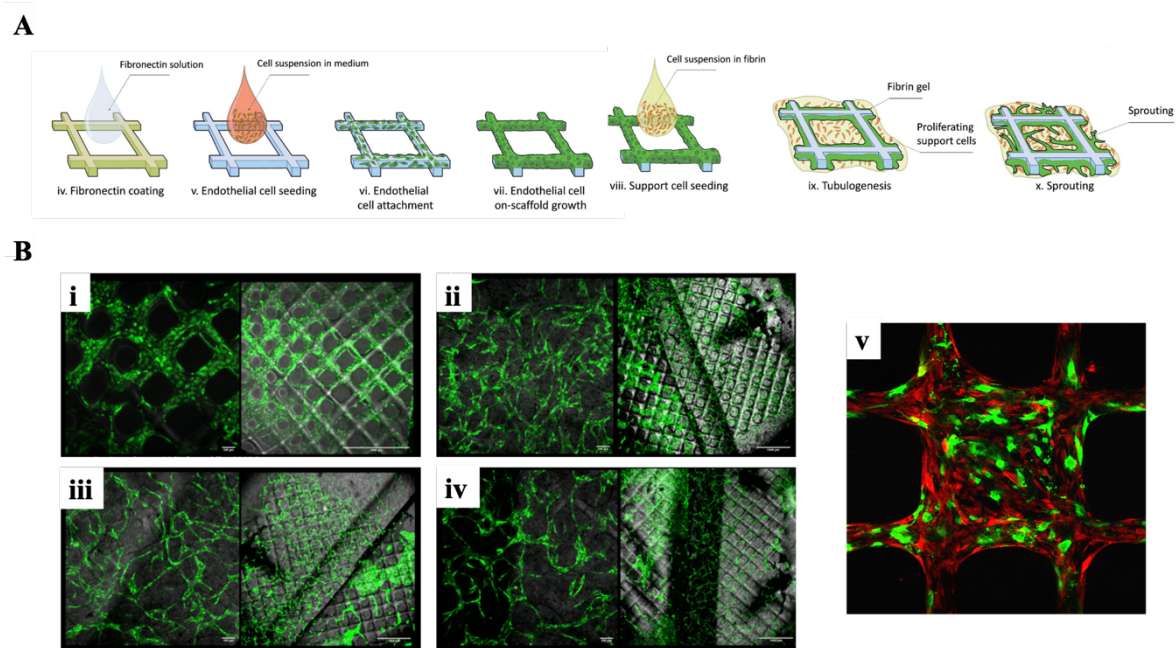


Figure 4-23: Scaffold biocompatibility for vascular tissue engineering. A) 3D two-step cell seeding protocol.^[6] B) CLSM images of HAMECs on **i**) day 2, **ii**) day 5, **iii**) day 7, **iv**) day 9 and **v**) on day 10 with DPSCs. Images taken by M.Sc. Oryan Karni Katovich.

sprouting due to their cross-talk. Moreover, vessel migration, stabilization, and differentiation, as well as the maturation of the SCs, are induced by co-culturing.^[224] The cell seeding protocol is a 3D two-step process,^[6] as seen in **Figure 4-23A**. Therefore, the scaffolds are coated with a fibronectin solution, which is an ECM glycoprotein commonly used to promote cell differentiation to other substrates.^[225] A cell suspension of 10^5 HAMECs in 25 μ L of cell medium was seeded onto the fibronectin-coated hydrogel scaffolds. On day two, as seen in **Figure 4-23Bi**, the cells attached to the scaffold and reached a confluence. The cells continue to grow along the seeded scaffolds, which takes up to nine days. The second seeding step includes the cell seeding of the SCs. Hence, 10^5 SCs were suspended in a fibrin pre-gel solution and finally added on top of the endothelialized scaffolds filling the scaffold pores (**Figure 4-23Bv**). Further studies need to investigate the impact of mechanical stimulation on the sprouting of the seeded cells once they start to proliferate. Therefore, the

hydrogel scaffolds can be mechanically stimulated by the bioreactor, similar to the uniaxial stretching experiments.

The stretchable PEGDA-PAA hydrogel scaffolds show great mechanical properties and present a cell-friendly environment, which enables further studies on vessel sprouting coupled with mechanical stimulation. The ease of handling and versatility to fabricate complex hydrogel scaffold geometry allows for studying the complex mechanism of blood vessel sprouting and migration and has the potential to drive and significantly improve tissue engineering as understanding sprouting decisions can help to mimic specific vascular architecture. Especially understanding mechanical cues and their impact on the sprouting decisions and directions enables the rational design of hierarchical vascular networks and allows the control of angiogenesis. Moreover, organ transplantation can be improved by the vascular architecture assisting the implant's survival and functional integration within the host body. In general, more suitable 3D environments can be designed to recreate a specific target tissue.

4.3. EHD Jetting of SF-Graphene Fibers

SF is a natural protein-based biomaterial that has emerged as a promising material for a wide range of applications beyond textiles due to its exceptional physical and chemical properties. In the last decade, extensive research has been done on silk for drug delivery purposes, as the material can be easily tailored in terms of degradability and functionalization for the regeneration of tissues. SF shows excellent thermal stability^[226] making it a promising material for electronic and optical applications, such as flexible electronics, sensors or photonics.^[227] Further, silk's biocompatibility and biodegradability make it an attractive alternative to synthetic materials. The ease of processing enables the fabrication into various forms, like films, matrices, and hydrogels.^[99, 105] However, silk is mainly known for its natural occurrence in the form of fibers. Its high tensile strength outperforms materials such as Kevlar in terms of toughness. The strength-to-density ratio of silk has been up to ten times higher than steel.^[228] Nonetheless, it has been a challenge to achieve these excellent properties found in native silk fibers in artificial ones. Their unique attributes based on the specific secondary and hierarchical structure are composed of highly crystalline beta-sheet domains interconnected by amorphous regions. While the beta-sheets provide rigidity and strength, amorphous domains are responsible for the elasticity and flexibility of the material. These specific structures have been difficult to mimic in artificially-made silk fibers, as the appropriate structures are lost during the fabrication process.^[229] Various research groups have aimed at manipulating the structure during silk regeneration. The Hudson group, for instance, applied compressive lateral force via hand drawing on wet-spun fibers similar to the spinning process of insects to achieve comparable properties to native fibers or even higher.^[230] Others have reported the reinforcement of silk fibers or membranes by graphene, graphene oxide or carbon nanotubes.^[231] Graphene is a 2D material that consists of carbon atoms arranged in a hexagonal lattice. Its high surface area and thermal conductivity enable

graphene to efficiently transfer heat, leading to rapid temperature changes. Especially the absorption and conversion of NIR light into thermal heat has been exploited for drug delivery and actuation systems. Combining graphene's thermal and mechanical properties with the one's of silk, bicompartamental silk and graphene fibers were fabricated, which can be triggered by light ($\lambda_{IR} = 850$ nm and $\lambda_{green} = 565$ nm) for actuation applications. In this chapter, Bianca Posselt and Dr. Erik Strandberg performed circular dichroism (CD) experiments. Dr. Stefan Heißler supported this dissertation by measuring Raman spectra. Valentin Tschan and Dr. Klaus-Peter Weiss helped with the mechanical tests of the fibers.

4.3.1. SF Concentration for EHD Jetting

Various concentrations of SF ranging from 10.0 – 50.0% w/v in Milli-Q water have been investigated for EHD jetting to determine the lowest possible SF concentration to create a stable fiber jet. For fiber actuation via NIR light, a lower SF concentration of the fiber is desired, as the fiber remains more flexible than at a higher concentration, which tends to make the fiber more rigid. Therefore, respective amounts of lyophilized SF were added and thoroughly mixed in Milli-Q water until fully dissolved. The solution with the lowest SF concentration of 10.0% w/v could not be jetted. Irrespective of the applied voltage U ranging from -10 – +10 kV, the viscosity was too low for jetting. Adjustments of other parameters, as seen in **Table 4-1**, such as needle tip-to-collector plate distance and a high flow rate of up to $80.0 \mu\text{L h}^{-1}$, were unsuccessful. Instead, the solution droplet detached from the metallic needle before a Taylor cone could be formed in a dripping manner (**Figure 4-24A**). Increasing the concentration to 20.0% w/v SF enabled particle spraying at a distance of 7.0 cm and after applying a positive voltage of $U = 4.0$ kV. However, the jet was unstable, resulting in interchangeable particle and fiber jetting. As seen in **Figure 4-24B**, particles and,

Table 4-1: EHD jetting conditions of various SF concentrations.

SF concentration [w/v]	Voltage [kV]	Distance [kV]	Flow rate [$\mu\text{L/h}$]	Result
10.0%	-10.0 – +10.0	0.5 – 10.0	80.0	No jet, low viscosity, dripping
20.0%	+4.0	7.0	60.0	Unstable jet, particles/fibers
30.0%	+5.0	3.0	20.0	Unstable whipping jet, beaded fibers
40.0%	+ 3.5	3.0	10.0	Unstable whipping jet, beaded fibers
50.0%	+ 1.7	1.0	10.0	Stable jet, homogenous fibers

to some extent, thin fibers with beads are created with average diameters of $d = 16.5 \pm 4.1 \mu\text{m}$, while the average fiber diameter is $d = 3.9 \pm 2.6 \mu\text{m}$. Starting at an SF concentration of 30.0% w/v, a higher amount of voltage, $U = +5.0 \text{ kV}$, was needed to fabricate more fiber-like structures. Nonetheless, beads are also observed even if to a lesser but greater extent, in terms of diameters ($d = 75.6 \pm 16.9 \mu\text{m}$). The same applies to the solution with 40.0% w/v SF, which shows comparable jetting results with inhomogeneous fiber diameters (**Figure 4-24C, D**). Both concentrations create fibers that are jetted in an unstable “whipping” and “coiling” manner, similar to the ones reported in the literature.^[232] Moreover, the solvent, in this case, water, did not fully evaporate during the jetting process. Consequently, the fibers were not fully dry once deposited on the collector plate, merging overlaid fibers and resulting in non-cylindrical but rather flattened fibers. Further, the two

solutions were more viscous than the previous ones, enabling a lower flow rate of 20.0 and 10.0 $\mu\text{L h}^{-1}$ for 30.0% and 40.0% w/v, respectively. The only difference between the two concentrations is that a lower voltage of $U = +3.5$ kV is applied to the higher concentrated solution of 40.0% w/v SF, as higher voltages increase the jet instability in terms of whipping, creating fibers with smaller bead diameters of $d = 8.8 \pm 4.3$ μm and $d = 21.1 \pm 4.0$ μm , respectively. In contrast, individual and cylindrical fibers could be jetted with the highest SF concentration of 50.0% w/v, as seen in **Figure 4-24E**. Due to its higher viscosity compared to the other solutions with lower SF concentrations, a lower voltage of $U = +1.7$ kV, as well as a flow rate of 10 $\mu\text{L h}^{-1}$, enables great control over the jet.

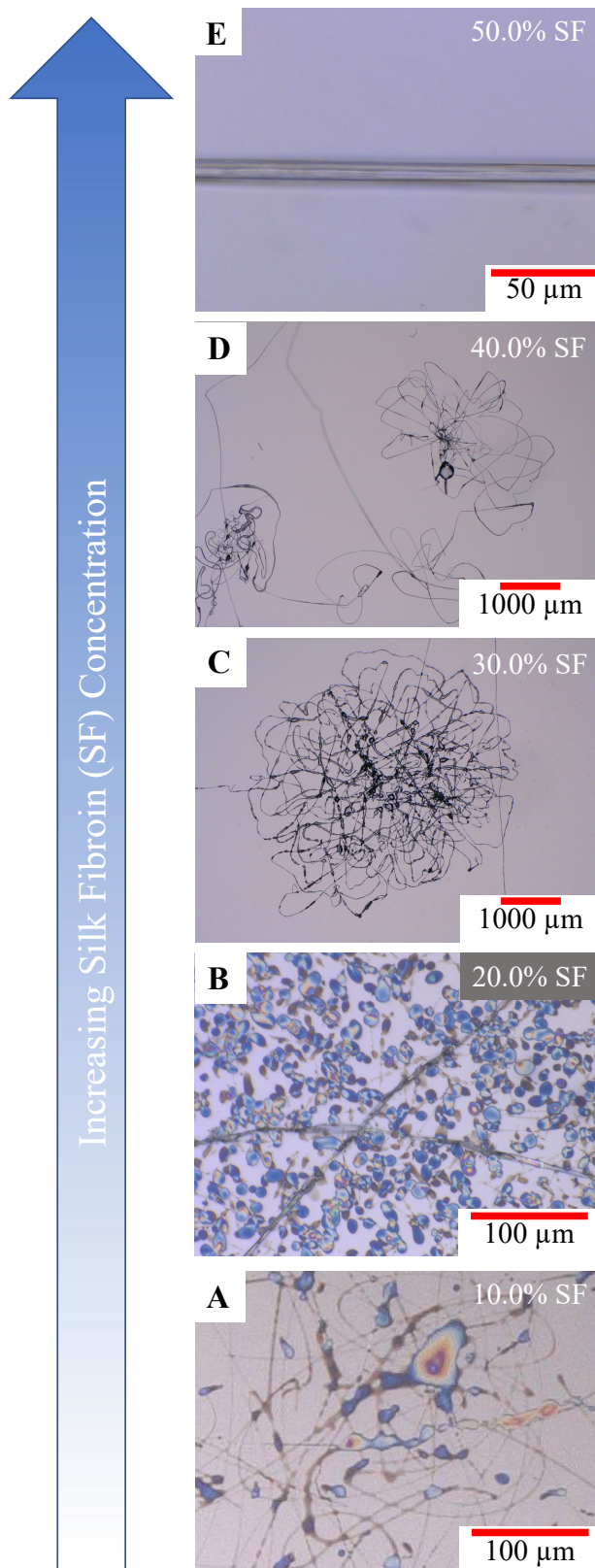


Figure 4-24: EHD jetting of various SF concentration in Milli-Q water. A) 10.0% w/v SF does not create a jet due to its low viscosity, resulting in dripping. B) 20.0% w/v SF creates an unstable jet with particles and fibers. C) 30.0% w/v SF and D) 40.0% w/v SF have an unstable whipping jet, creating beaded fibers. E) 50.0% w/v SF creates a stable jet fabricating homogeneous fiber.

4.3.2. Characterization of SF Fibers

SF is composed of anti-parallel beta-sheet structures, which are arranged in stacked and layered patterns. Polarized light microscopy (PLM) is used to analyze the beta-sheet structure of the fibrous protein. The SF fiber shown in **Figure 4-25A** is observed under a bright-field microscope. Under PLM, the same sample is shown in **Figure 4-25B**. However, no colored structures can be seen and the image appears dark. This lack of transmitted light is due to the non-crystalline and amorphous regions within the SF fiber, which lack a well-defined structure. Instead, a more random arrangement of amino acid residues can be found. As the

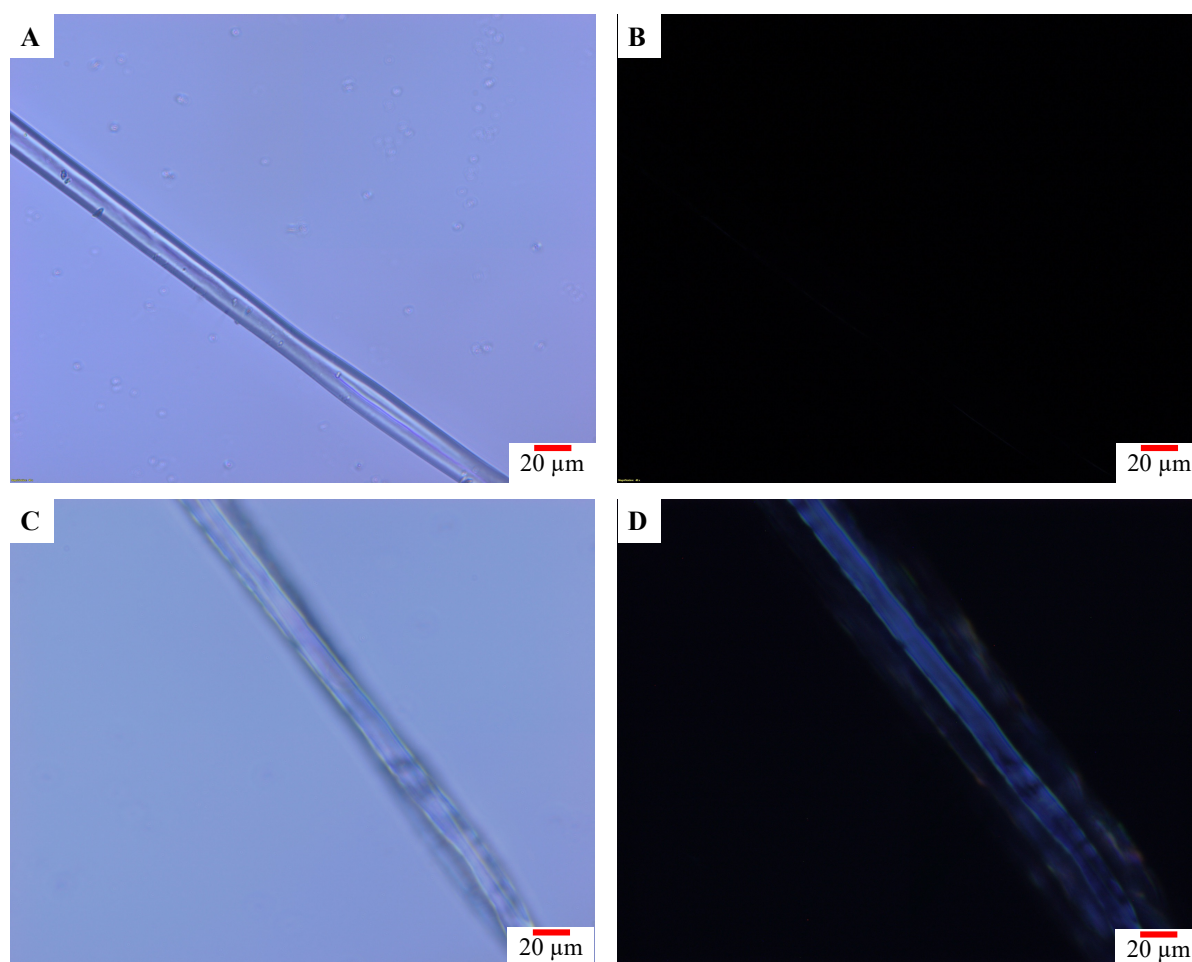


Figure 4-25: EHD jetted SF fibers under A, C) bright field microscope and B, D) polarized light microscope. Fibers treated with MeOH (C, D) exhibit birefringence.

refractive indices of amorphous regions are isotropic, no birefringence is caused once the polarized light passes the sample and the fiber appears dark. Moreover, as-jettted SF fibers are water soluble and instantly dissolve once exposed to water. Therefore, SF fibers were treated with methanol vapor, as methanol increases the hydrogen bonding between the protein chains and the formation of more stable beta-sheet structures, making the SF fibers water insoluble. In particular, these crystalline regions of SF consist of anti-parallel beta-sheets, which are formed by hydrogen bonds between the carbonyl oxygen of one amino acid and the amide hydrogen of the next amino acid in the sequence. This induced conformational transition from random coils to anti-parallel beta sheets, can also be seen under PLM. The methanol-treated SF fiber in **Figure 4-25C**, already shows more interference patterns than the untreated, as-jettted SF fiber. Under PLM, the effect of methanol on the secondary structure of SF is more evident with the fiber appearing birefringent (**Figure 4-25D**). This birefringence is due to the crystalline structure of SF, as polarized light interferes with those regions and splits the light into two different refractive indices while passing through the fiber.^[233]

The secondary structure is verified with CD performed by Bianca Posselt and Dr. Erik Strandberg. As seen in **Figure 4-26A**, both samples, methanol-treated SF fiber and solution, show a beta-sheet structure with typical positive and negative bands around 195 and 218 nm, respectively.^[234] The methanol-treated SF fiber, however, has a lower signal which is assumed to be due to fast sedimentation of SF fibers during the CD measurement. As reported by Lee et al., environmental factors and preparation conditions highly affect the conformation transition behavior of SF, which explains the beta-sheet spectrum of SF solutions instead of a random coil one.^[235]

Raman spectroscopy was performed by Dr. Stefan Heißler for further conformational characterization of untreated, and methanol-treated SF fibers, as well as solution. Raman spectra I and II in **Figure 4-26B** show spectra of SF solution and untreated SF fibers,

respectively. In both spectra the amide I band appears at 1659 cm^{-1} , while the amide III region shows complex maxima detectable at 1276 and 1245 cm^{-1} . These maxima match the ones reported for the metastable Silk I form.^[1c-e, 5] Silk I is the natural state of SF, in which SF is amorphous and soluble. This state can be induced by drying the silk protein, similar to EHD jetting SF in which water evaporates during the fabrication process. As mentioned above, the as-jetted SF fibers instantly dissolve upon exposure to water, which further supports the findings that spectra I and II show amorphous regions. Especially the maxima of amide I at 1659 cm^{-1} and amide III at 1245 cm^{-1} indicate random coil conformation of these samples.^[236] Spectrum III, on the other hand, shows the spectrum of methanol-treated fibers and suggests that methanol changes the spectra of the treated fiber, as new maxima appear or were shifted. In accordance with literature, the amide I band, for instance, shifts the band from 1659 cm^{-1} to 1663 cm^{-1} and becomes narrower than the one found in the other two spectra due to the methanol treatment.^[1c] Further, the amide III region shows new maxima detected at 1262 and 1236 cm^{-1} . Other peaks, however, appear to be sensitive to the methanol treatment as they disappear from the spectrum. More specifically, bands at 1107 , 938 and 865 cm^{-1} disappear, inducing a reduction in the intensity of the band at 855 cm^{-1} . A new band, on the other hand, appears at 1084 cm^{-1} . In agreement with results reported by others, the amide I and III bands appearing at 1663 and 1236 cm^{-1} are attributed to beta-sheet conformation and the more stable Silk II form verifying the conformational change due to methanol treatment.^[237] These results are in accordance with the previously reported observations that methanol-treated fibers are water insoluble as the insolubility of SF is due to the highly ordered and tightly packed beta-sheet structure of the protein.

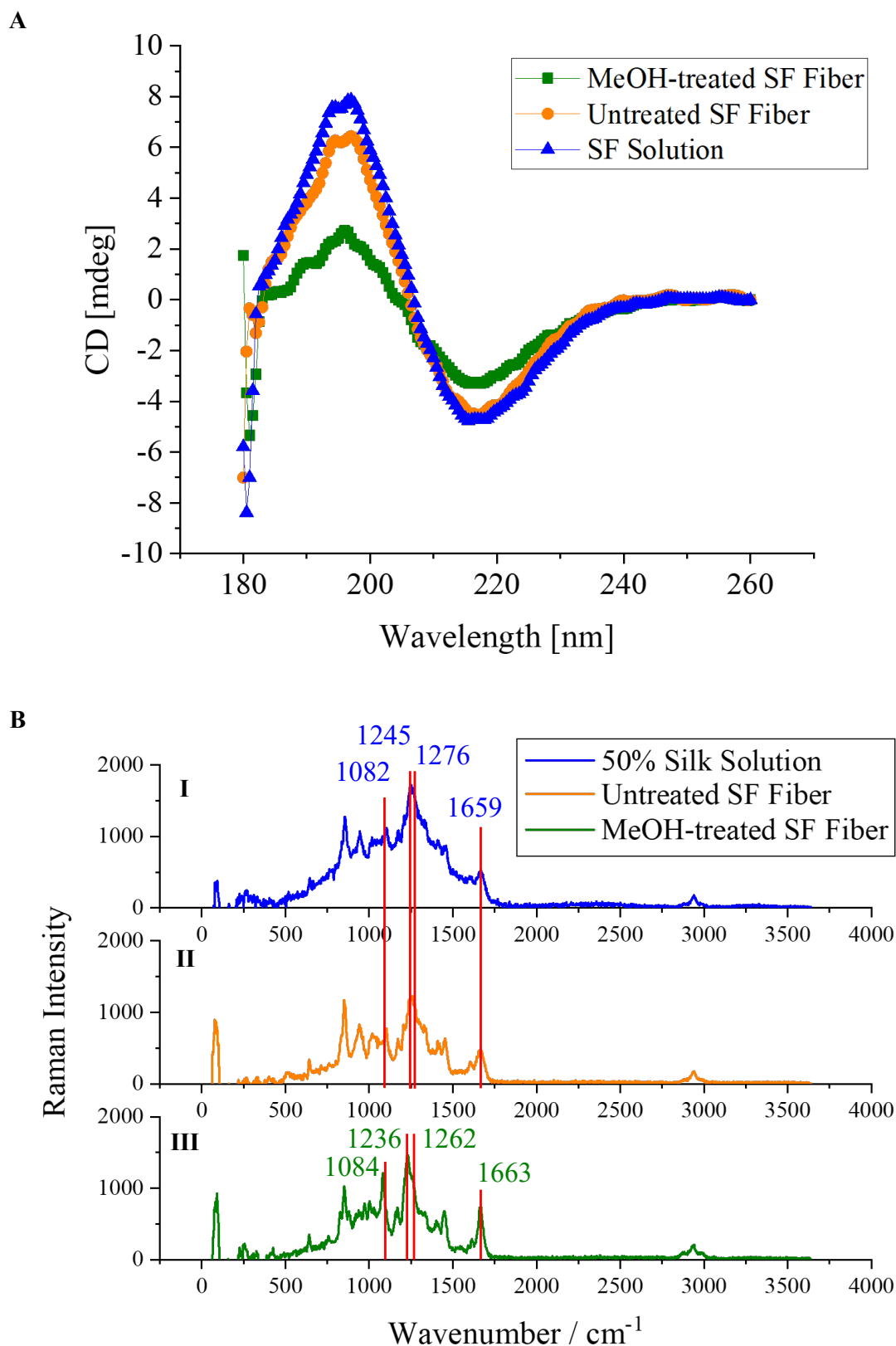


Figure 4-26: SF Secondary Structure Analysis. A) Circular dichroism of untreated and methanol-treated SF fibers and SF solution measured by B. Posselt & Dr. E. Strandberg. B) Raman spectroscopy of untreated, methanol-treated SF fibers, and SF solution. Untreated SF fiber and 50.0% silk solution show maxima of metastable Silk I form.^[5] MeOH-treated SF fiber shows new and shifted bands attributed to beta-sheet conformation and the more stable Silk II form due to methanol treatment. Spectra measured by Dr. S. Heißler.

4.3.3. Pre-Treatment of Graphene

Pre-treating graphene is a crucial step to dispersing and incorporating graphene with other materials, such as polymer solutions. Many research groups have focused on the dispersion of graphene by oxidating graphene to render it polar.^[238] The oxidation process introduces oxygen functional groups, such as hydroxyl (-OH) and epoxy (-O-) to the graphene surface, increasing the material's hydrophilicity. The introduced oxygen functional groups, however, significantly alter the material's electronic properties by disrupting the bonding scheme in the basal plane. More specifically, as the groups can form polar bonds with other molecules, an uneven charge distribution across the graphene surface is observed, transforming a highly electrically conductive material into an insulating or semi-conductive one. Chemical or thermal reduction can remove the oxides.^[239] Nonetheless, the original electrical conductivity cannot be recovered, as structural defects remain.^[240] Other groups have evaluated the graphene dispersion in a number of solvents or aqueous surfactant solutions.^[241] Based on literature, various dispersants have been investigated in this chapter to find a suitable graphene dispersant that is compatible for further processing with SF. Prior to the addition of dispersants, graphene is wet-ground with methanol and further processed via reflux to remove any residual impurities or contaminants from the graphene surface. Glycerol and EG have been explored as potential graphene dispersants due to their reported properties as plasticizers that can also act as lubricants.^[242] Plasticizers are often added to polymer matrices to increase a material's flexibility and plasticity. In this case, glycerol and EG act as dispersants of graphene by reducing the interfacial stress between graphene and polymer matrix to improve the material's toughness. Both plasticizers, however, denature the protein as soon as low concentrations of SF are added to the mixture, resulting in agglomerations of graphene and SF, as seen in **Figure 4-27A, B**. Low-concentrated SF is added to the mixtures for better annealing with the higher concentrated SF solution at a later stage.

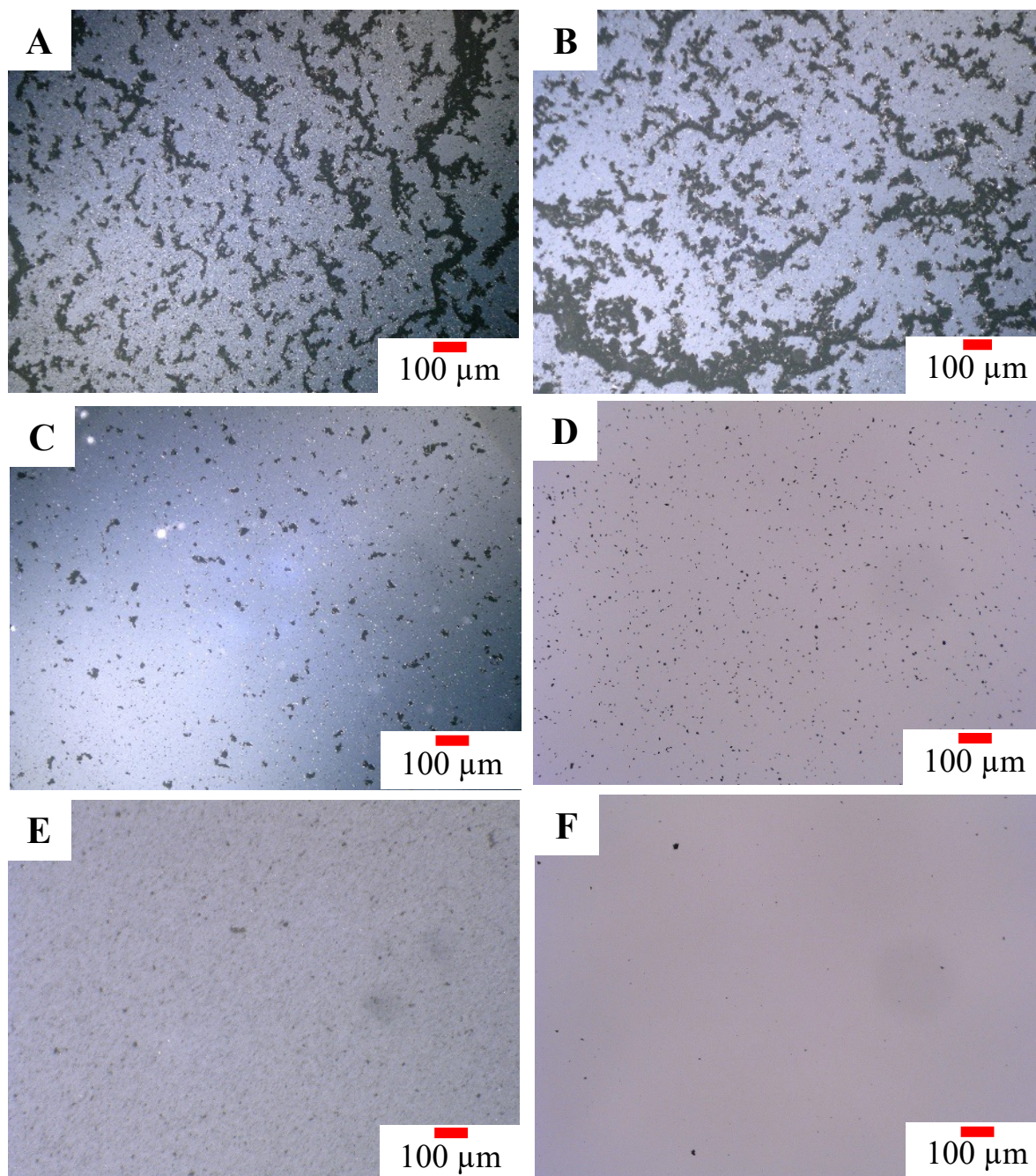


Figure 4-27: Graphene dispersion with A) Glycerol (1.00 w/v) and B) Ethylene Glycol (1.00 w/v) denature SF, resulting in SF and graphene agglomerations. C) Soy lecithin (1.00 w/v) and ethanol (0.01% v/v) result in agglomerations as ethanol denatures SF D) Soy Lecithin (1.00 w/v) induces smaller graphene aggregations. E) Polysorbate 20 (1.00 w/v), a non-ionic surfactant, stabilizes the graphene dispersion in liquid medium, but denatures SF as dispersion turns milky. F) Calcium lignosulfonate (1.00% w/v) and cremophor (0.125% v/v) shows great graphene dispersion and SF compatibility.

Solvents like ethanol, however, which has successfully been used as graphene dispersant,^[243] also denature SF, similar to the previous two plasticizers. Irrespective of the amount, as little as 0.01% v/v ethanol, and in combination with soy lecithin, a natural dispersant from the food industry, which can improve the dispersibility of graphene in organic solvents due to its high affinity for ethanol, SF instantly denatures once exposed to the solvent (**Figure 4-27C**). Soy lecithin is a natural non-ionic surfactant showing great graphene dispersion and compatibility with SF, as no protein denaturation is observed. Soy lecithin, a phospholipid mixture, is amphiphilic, having both hydrophobic and hydrophilic regions. While the hydrophobic regions can interact with the hydrophobic regions of the graphene sheets, the hydrophilic regions interact with the liquid medium. Thus, soy lecithin molecules create a layer surrounding the graphene sheets to form a stable dispersion. The shielding further reduces the surface energy of graphene sheets, which reduces re-aggregation and the tendency to form larger clusters. Many research groups have shown the successful use of (non-ionic) surfactants as graphene dispersants.^[244] Nonetheless, as seen in **Figure 4-27D**, smaller graphene aggregations remain after dispersion with soy lecithin, which was already seen before the addition of SF (data not shown). Another dispersant used in the food industry is polysorbate 20, commercially also known as Tween 20. The non-ionic surfactant acts like soy lecithin and other non-ionic surfactants by adsorbing onto the surface of the graphene sheets and stabilizing the dispersion in a liquid medium. The graphene is well dispersed and shows fewer agglomerates than soy lecithin. Regardless of the effective graphene dispersion, the mixture turned milky and cloudy once SF was added, indicating protein denaturation, as seen in **Figure 4-27E**, even if to a far lesser extent than glycerol or EG. Calcium lignosulfonate, a water-soluble anionic polyelectrolyte polymer, is also used as a plasticizer. Yet, mainly for making concrete.^[245] In terms of graphene dispersion and in combination with another non-ionic surfactant, cremophor, which stabilizes emulsions of non-polar materials in water,

calcium lignosulfonate shows great dispersion properties, as well as SF compatibility with fewer graphene agglomerates than soy lecithin (**Figure 4-27F**). As graphene mixtures with soy lecithin and calcium lignosulfonates showed the greatest potential regarding graphene dispersion and SF compatibility, their ability of graphene dispersion was assessed by analyzing the graphene particle sizes. As seen in **Figure 4-28A**, 98.4% of the graphene surface area within the soy lecithin mixture are in the range of 10.0–100.0 μm^2 , while almost 83.0% of the graphene particles within the calcium lignosulfonate mixture are smaller with surface areas in the range of 0.1–10.0 μm^2 . Based on these results, the graphene mixture with calcium lignosulfonate was chosen for further processing via ultrasonication. Graphene particle sizes significantly decreased, as seen in **Figure 4-28B**, with 43.2% having particle surface areas in the lower range of 0.01 and 0.1 μm^2 . Other concentrations of calcium lignosulfonate did not significantly change the

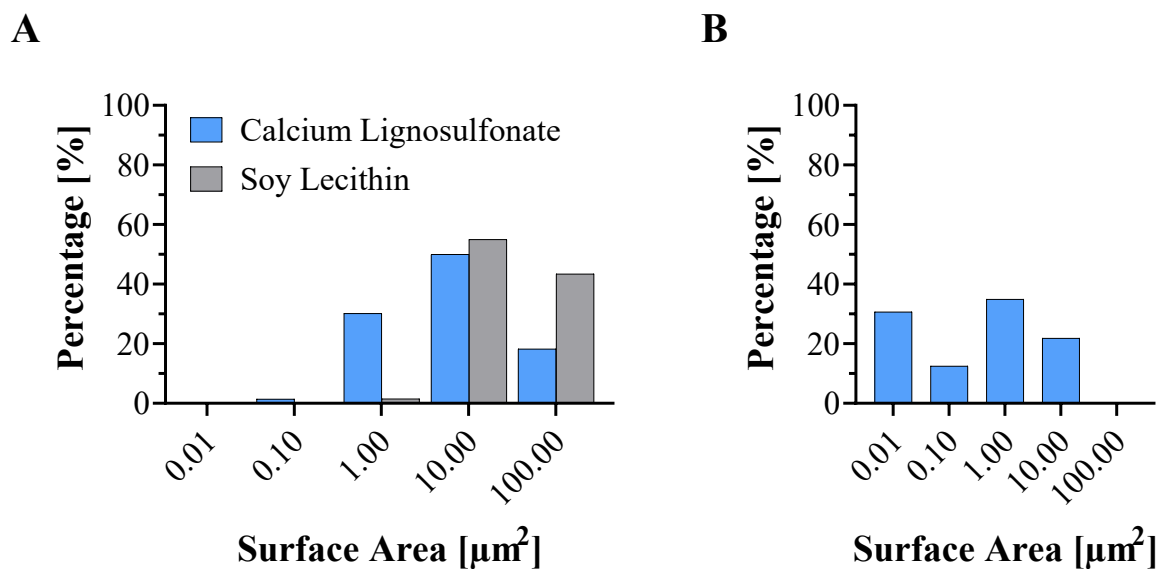


Figure 4-28: Particle Surface Area Distribution of Graphene Dispersions. **A)** Before ultrasonication calcium lignosulfonate induces smaller graphene agglomerates compared to soy lecithin. **B)** After ultrasonication with calcium lignosulfonate, graphene particle sizes decrease in the lower range of 0.01 and 0.1 μm^2 .

graphene dispersion. Therefore, the lowest concentration was chosen to keep the concentration of the additives as low as possible to prevent interference while jetting, as surfactants lower the surface tension, which can negatively impact the EHD jetting.

4.3.4. Fabrication of Bicompartamental SF-Graphene Fibers

Bicompartamental SF-graphene fibers are created via EHD co-jetting, as explained in **Chapter 4.1.1**. Therefore, 50.0% w/v SF was prepared in Milli-Q water. For the actuating solution, pre-treated graphene (6.7% w/v) dispersed in calcium lignosulfonate (1.0% w/v) and cremophore (0.125% v/v), was added to the aforementioned solution of SF. The other compartment only consists of 50.0% w/v SF, as seen in **Figure 4-29A**. Homogeneous fibers with diameters of 18.0 μm are fabricated with uniform and equally sized compartments. Higher concentrations of calcium lignosulfonate or cremophore were investigated for pre-treating graphene. However, as mentioned in **Chapter 4.3.3**, higher concentrations of these non-ionic surfactants did not significantly improve the graphene dispersion. Instead, EHD jetting was highly impacted, as the surface tension of the jetting solution was too low, preventing the fabrication of bicompartamental fibers. As a result, only the neat SF compartment was uniformly jetted, while the graphene containing jet was unstable. The solution was rather dripping and did not form a stable Taylor cone. For water insolubility and higher mechanical strengths, the bicompartamental fibers were treated with methanol vapor to transform the random coils into more stable beta-sheets.

The graphene within the actuating compartment and its unique thermal properties enables the actuation of the bicompartamental fiber once the fiber is exposed to NIR light, as seen in **Figure 4-29B**. More specifically, graphene has the ability to absorb and quickly release heat. Upon NIR exposure, graphene absorbs the heat within the actuating compartment and induces an expansion of the SF within the compartment. The other compartment consisting of

the neat SF, remains unaffected and bends due to the actuation of the other compartment. The light-responsive actuation of the bicompartamental fibers is reversible once the trigger is removed. In the case, where the NIR light source is turned off, the bicompartamental fiber returns to its initial state. The actuation of bicompartamental SF fibers is investigated in **Chapter 4.3.6**.

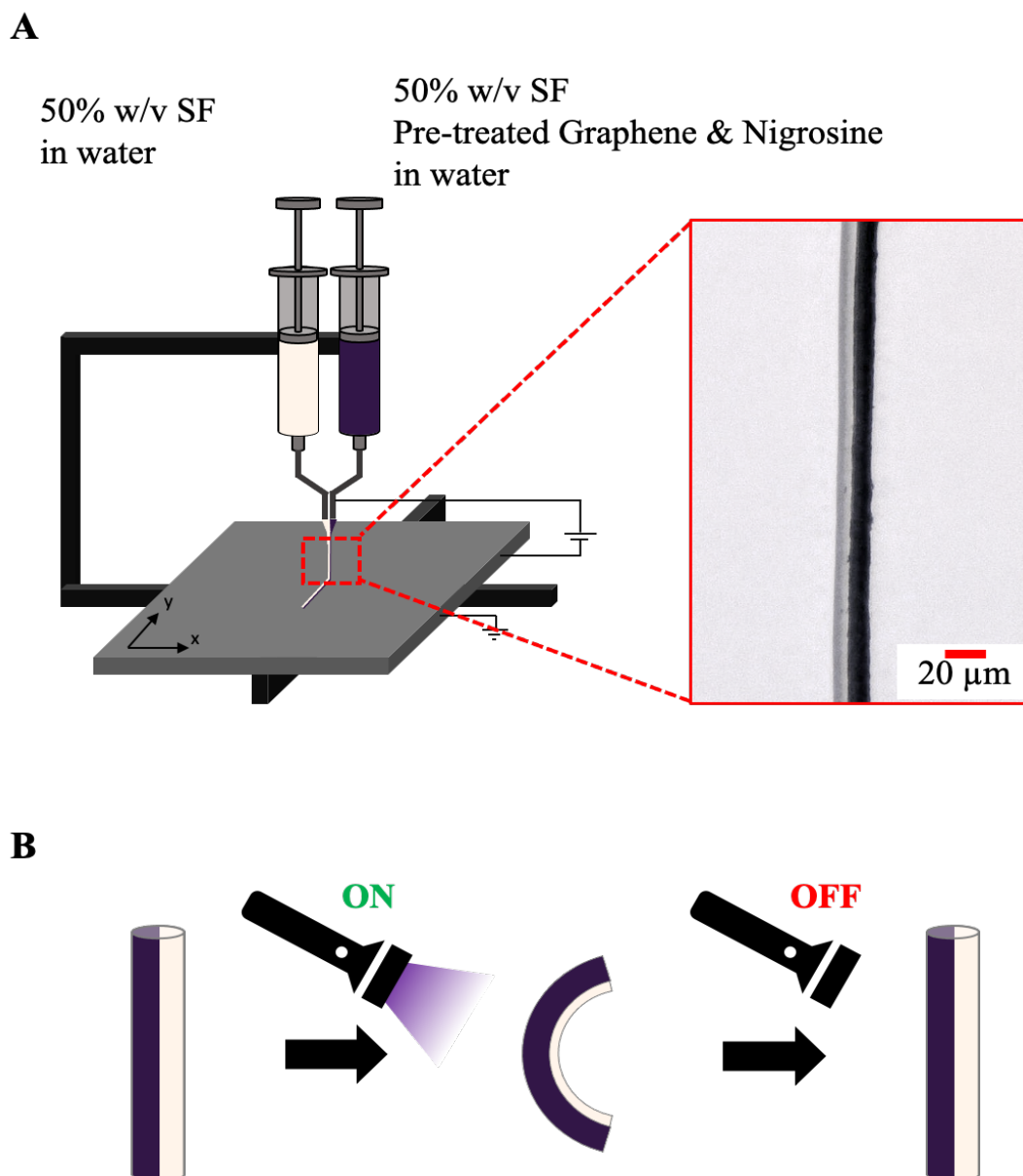


Figure 4-29: EHD Co-jet writing of light-responsive SF-graphene fibers. **A)** Schematic setup for bicompartamental fiber preparation via jet writing of 50.0% w/v SF and 50.0% w/v SF with pre-treated graphene, calcium lignosulfonate (1.00% w/v) and cremophore (0.125% v/v). **B)** Reversible shape reconfigurability mechanism due to geometric anisotropy and heat absorbance of graphene resulting in the induced expansion of SF.

Raman spectroscopy was performed to investigate potential impacts of the EHD jetting process on the graphene. **Figure 4-30** shows Raman spectroscopy spectra of pristine graphene and bicompartamental SF-graphene fiber excited with a laser of a wavelength of $\lambda = 532$ nm. Both spectra exhibit two bands at 1350 cm^{-1} and 1582 cm^{-1} , which are graphene's characteristic features, also known as D and G band, respectively.^[4] The latter, the G band, indicates the degree of the graphitization of the graphene layer. Moreover, the quality of graphene can be derived from the intensity of the G band as it is related to the number of sp^2 carbon atoms in the graphene layer. In contrast, the D band gives an indication of the degree of disorder or defects in the graphene layer. Similar to the G band, the intensity of the D band indicates the quality of the graphene. In this case, however, the D band

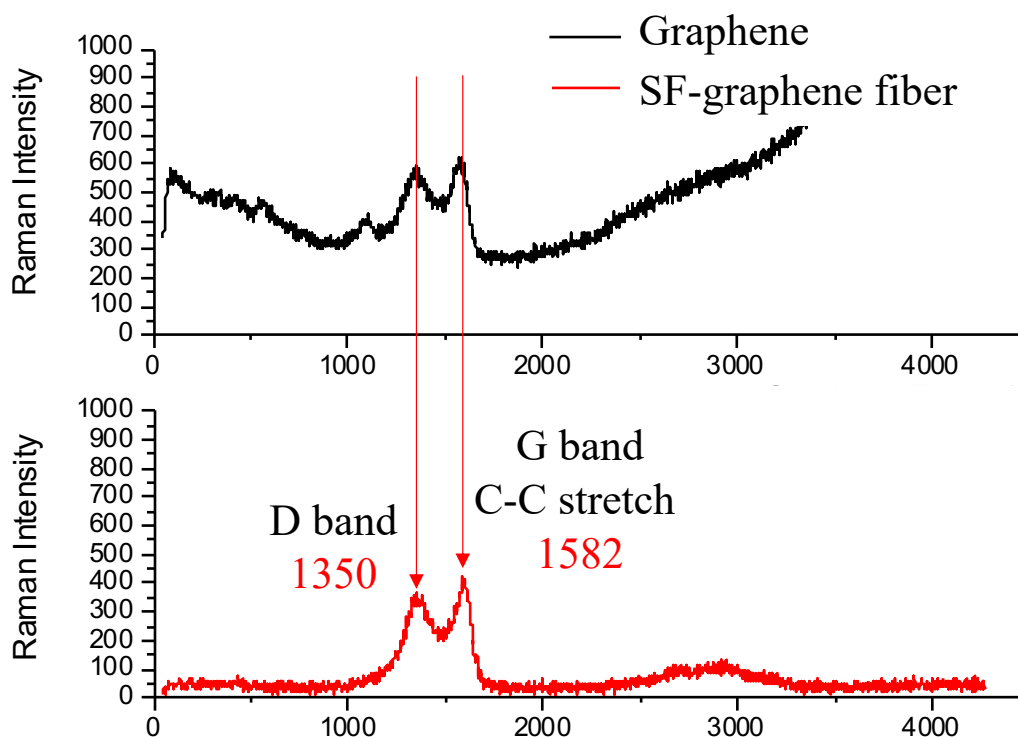


Figure 4-30: Raman Spectroscopy of Graphene. Excitation of bicompartamental SF-graphene fiber and pristine graphene at $\lambda = 532$ nm show graphene's characteristic D and G band at 1350 cm^{-1} and 1582 cm^{-1} , respectively.^[4] EHD jetting process does not impact graphene. Spectra measured by Dr. S. Heißler.

intensity is related to the number of defects or sp^3 -hybridized carbon atoms in the graphene lattice. Considering the two bands, an intensity ratio of both I_D/I_G , is often used to measure the quality of graphene. A higher G band intensity I_G than the one of the D band I_D , therefore, indicates high-quality graphene without any impact of SF or due to the EHD jetting process on graphene, as seen in the bands.

4.3.5. Mechanical Tests of SF-Graphene Fibers

SF fibers were mounted in a tensile tester (Landmark® 370.10 servohydraulic test systems, MTS Systems GmbH) to assess their mechanical strengths and properties. Valetin Tschan and Dr. Klaus-Peter Weiss supported these mechanical tests. Due to the thin fiber diameters, the scotch tape was used to transfer and mount the fibers for tensile testing with a load cell of 5 kN. Untreated and methanol-treated SF fibers, as well as bicompartmental SF and graphene fibers of equal length (5.0 cm), were individually tested under monotonic load to fracture experiments, in which the lower clamp is vertically moved downwards. The fracture point of an untreated SF fiber is indicated by the yellow arrow in **Figure 4-31AII**. As seen in the force-displacement graph in **Figure 4-31B**, the untreated SF fibers break at a force value of $F = 8.26 \pm 4.85$ mN. As expected, and compared to other samples, untreated SF fibers break at the lowest force measured since untreated silk fibers are mainly in the random coil conformation with some alpha helices.^[246] The lower fraction of beta-sheet structures in silk I is often disrupted or distorted due to the more random arrangement of protein chains. This random and irregular structure is responsible for the low crystallinity and thus, induces poor mechanical strengths and stability within this fiber type.^[230a, 247] Moreover, the standard deviation is the highest amongst all tested fiber types due to large structural variations between individual fibers. The methanol-treated fibers, on the other hand, can withstand higher forces up to an average value of $F = 10.40 \pm 1.43$ mN until breaking after a

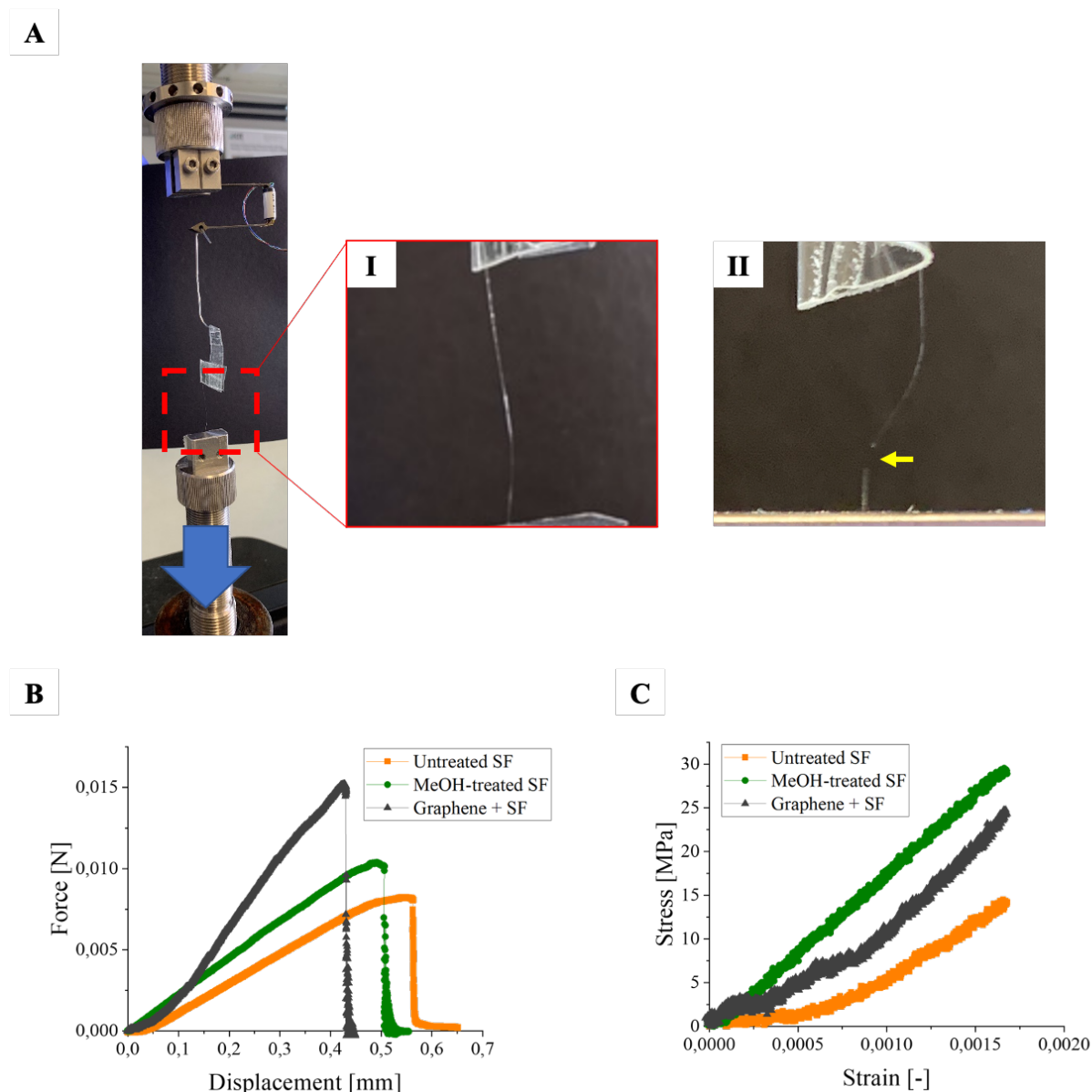


Figure 4-31: Tensile Tests of (bicompartmental) SF fibers. A) Setup of mechanical tests. SF fiber I) before and II) after tensile test. B) Force-displacement graph of tested fibers with untreated SF fibers in the random coil conformation breaking at the lowest force. C) Stress-strain curves of tested fibers show untreated SF-fibers exhibiting highest elasticity. ($n = 3$ for all groups). Experiments supported by V. Tschan & Dr. K.-P. Weiss.

displacement of $d = 0.55 \pm 0.24$ mm. Their higher fraction of beta-sheet structures results in higher mechanical strength compared to the untreated SF fibers. Natural silk fibers, nonetheless, which were degummed, meaning that the fibers only consist of SF without sericin, can withstand up to 12-fold higher forces than the artificially regenerated fibers

fabricated via EHD jet writing.^[248] These results are in accordance with literature, as artificial fiber regeneration often lacks the ability to highly align the protein chains along the fiber axis. One common approach, however, to match the mechanical properties of native silk is to mechanically draw spun fibers to achieve higher alignment. Therefore, SF fibers are extruded through a small orifice, mostly into a coagulation bath consisting of methanol or ethanol. By controlling the speed of the spinneret and the rate of fiber collection, the protein chains are oriented in a particular direction, resulting in drawn fibers with a high degree of alignment.^[249] Alignment via an electric field, like electrospinning, has also been reported as an effective approach. In this case of EHD jet writing, however, it is assumed that the needle tip-to-collector plate distance is too short for the protein chains to align along the fiber axis. The last fiber type, bicompartmental fibers with graphene, can withstand the greatest force with an average value of $F = 15.21 \pm 3.27$ mN. Several studies have demonstrated the increased mechanical strength of SF composite materials due to the incorporation of graphene.^[250] At the same time, however, these fibers break after the shortest displacement with an average value of $d = 0.46 \pm 0.08$ mm since the incorporation of graphene can lead to a reduction in the elasticity of SF fibers. In particular, graphene is a stiff material, which can limit the SF fiber's ability to stretch and deform under stress. In **Figure 4-31C**, this brittleness of the bicompartmental fibers is confirmed by the high Young's modulus $E = 19.31 \pm 1.86$ GPa, which is 3.2-times greater compared to SF-graphene films, as reported by Ling et al.^[250b] The same applies to methanol-treated SF fibers, which ordered and crystalline structures are responsible for their mechanical strength and a higher level of stiffness. At the same time, this strength and stiffness come at the expense of the SF's elasticity which is reduced and seen in the lower Young's modulus $E = 18.16 \pm 2.42$ GPa. As expected, the untreated SF fibers are the most elastic fiber type among all tested fiber types. Their more amorphous and less crystalline form of SF, compared to silk II as seen in

methanol-treated fibers, enables more movement and flexibility, resulting in the lowest Young's modulus $E = 11.40 \pm 5.87$ GPa, which is in accordance with values reported in literature.^[251]

4.3.6. Light-Triggered Actuation

In this chapter, the actuation ability of bicompartmental SF fibers was investigated. Therefore, various bicompartmental SF fibers with graphene, nigrosine dye, or a combination of both were one-sidedly exposed to NIR ($\lambda = 850$ nm, $P = 3.2$ W) or green light ($\lambda = 565$ nm, $P = 3.2$ W). The displacement from its initial position was measured after irradiating the graphene-containing compartment of the fibers for a total of 3.0 seconds until no further actuation was observed.

First, various graphene concentrations ranging from 2.0 – 17.0% w/v were explored to investigate which concentration induces the greatest actuation response. Concentrations exceeding 8.0% w/v, however, were unsuited for jetting as high graphene concentrations resulted in shortcuts or needle clogging. The results show that an increase in graphene concentration does not increase the actuation response. On the contrary, higher concentrations can result in a decrease in fiber displacement upon light irradiation. Concentrations of 7.5% w/v, for instance, displaced the fiber by 60.3 ± 0.3 μm for NIR laser, while a concentration of 6.7% w/v achieved $x = 72.4 \pm 5.2$ μm . An increase in graphene concentration increases light absorption, which subsequently results in higher thermal conversion. Nonetheless, this comes with a trade-off of the fiber's flexibility as higher graphene concentrations stiffen the fiber. Thus, the increase in heat and, consequently, expansion of SF is not sufficient enough to overcome the higher stiffness. Similar, but the other way around is seen in lower graphene concentrations. While lower graphene concentrations have a lower impact on the flexibility of SF, thermal conversion is not high

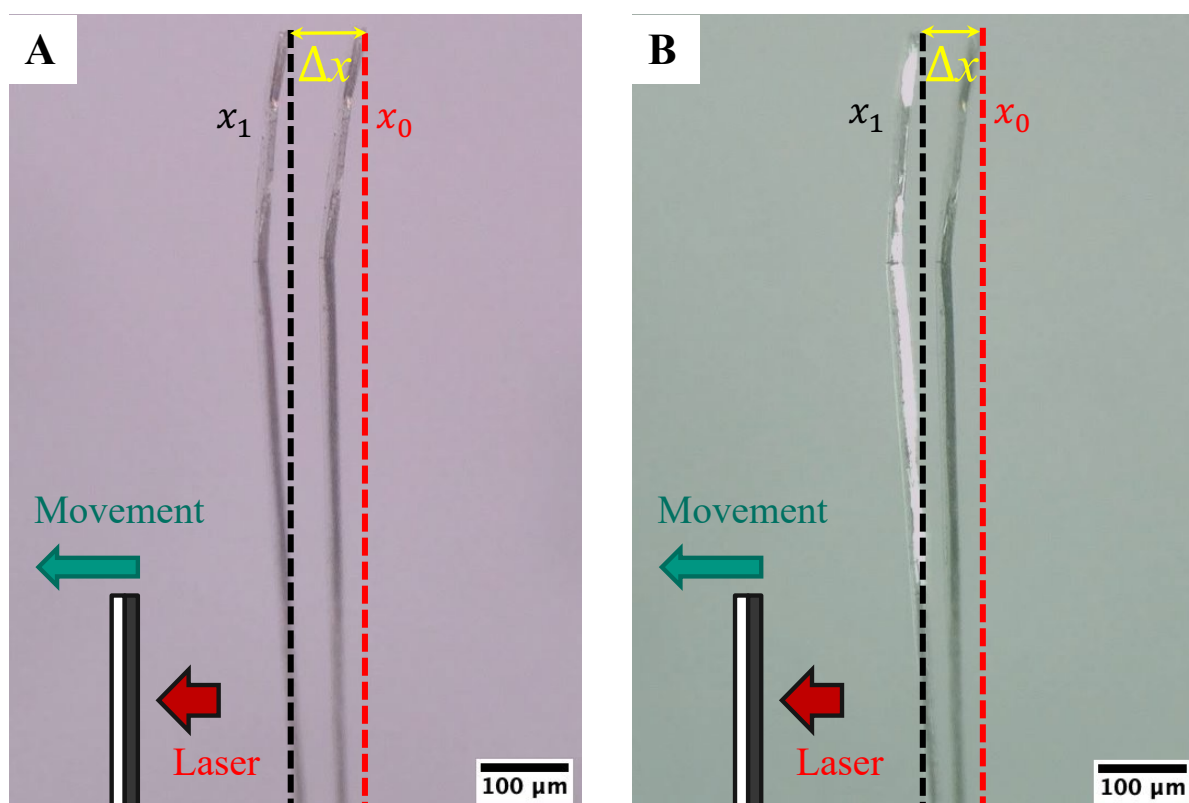


Figure 4-32: Reversible actuation of SF-graphene bicompartmental fibers with A) NIR ($\lambda = 850$ nm) or B) green ($\lambda = 565$ nm) LED laser exposing the graphene compartment, which induces the SF within the compartment to expand, resulting in a fiber actuation in which the fiber moves from its initial position x_0 (red dotted line) to x_1 (black dotted line) while the laser is on. Once the laser is off, the fiber moves from x_1 back to its initial position x_0 . The total fiber displacement due to the actuated movement is Δx .

enough to significantly trigger an actuation response. Displacements of $30.1 \pm 0.4 \mu\text{m}$ for NIR laser were observed for bicompartmental SF-graphene fibers with 2.0% w/v graphene concentrations. Therefore, all further graphene-containing fibers were fabricated with a concentration of 6.7% w/v. An overlay image is seen in **Figure 4-32A**, which shows the bicompartmental fiber before and after NIR light exposure. The fiber moved $75.0 \mu\text{m}$ from its initial position and away from the light source, in this case, towards the left. NIR exposure from the left side onto the pristine SF compartment results in the same direction of fiber movement as previously described (**Figure S 1**, Supporting Information). Thus, irrespective of the compartment being exposed to the NIR light, the graphene-containing compartment

expands. Control experiments with monocompartmental SF fibers were performed, which did not show any movement upon IR exposure. A green light source was used to irradiate the same bicompartamental SF-graphene fiber to investigate the fiber's behavior under another wavelength. As seen in **Figure 4-32B**, the fiber also moves away from the light source. Under the green wavelength, however, the fiber moved 27.6% less from its initial position than under NIR irradiation (displacement $x = 53.4 \mu\text{m}$). In both cases, nonetheless, and irrespective of the wavelength, the graphene-containing compartment expands while the pristine SF compartment remains unchanged. Graphene can absorb and quickly release heat upon exposure to NIR light, transferring the heat within the compartment to SF, which extends with increasing temperature.^[252] The reduced actuation response under green light compared to NIR light is due to the different absorption characteristics of graphene, resulting in a lower temperature increase within the fiber. Graphene shows strong absorption in the NIR region in which the photon energy is transferred to the graphene lattice.^[253] As a result, its temperature increases and leads to heat generation, while graphene has weaker absorption in the green region, generating less heat.^[173a, 254] Consequently, SF expands to a smaller extent than under NIR exposure.

To further enhance the actuation response of bicompartamental SF-graphene fibers, nigrosine was explored as potential dope to increase NIR light absorption. Nigrosine is a common biological stain for tissues and cells,^[255] which is often used due to its strong light-absorbing abilities as a dye.^[256] Many research groups have harnessed the dye's absorption capabilities for applications such as optical limiters.^[257] Others, on the other hand, utilized the dye's absorption for thermal conversion^[258] in applications like photothermal therapy against cancer^[259] or NIR light-triggered actuations.^[14a, 260] UV-vis spectroscopy of nigrosine was performed and compared to the spectra of pristine SF. As seen in **Figure 4-33**, pristine SF

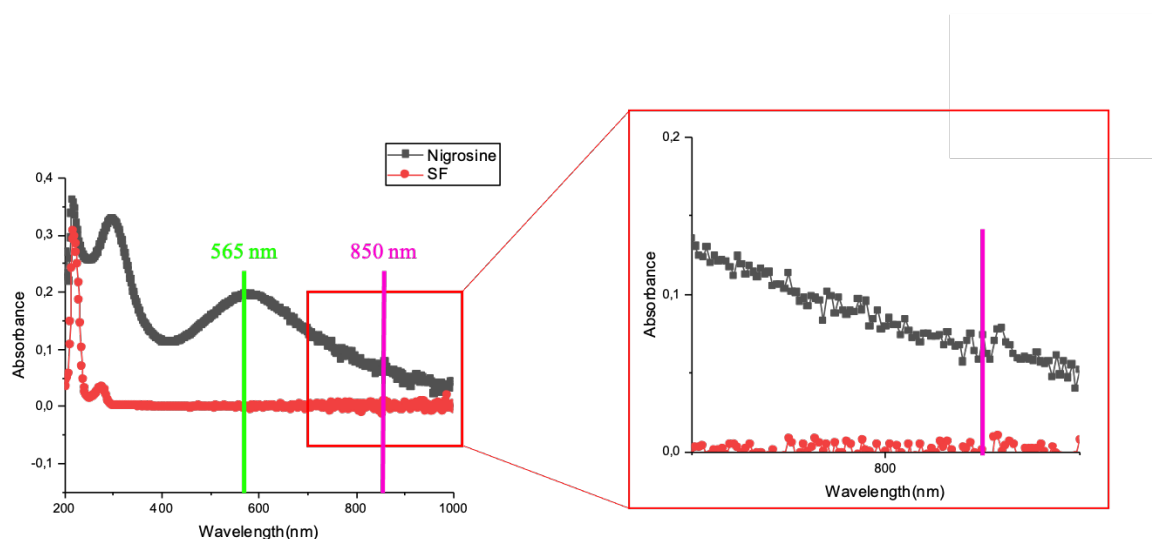


Figure 4-33: UV-Vis of Nigrosine Dye and Pristine SF. Green laser wavelength at $\lambda = 565$ nm (green line) and NIR laser wavelength at $\lambda = 850$ nm (pink line) show maximum absorption peak around 300 nm for both, nigrosine and SF. The green laser lies within nigrosine's shoulder peak in the range of 500 – 650 nm. Inset shows nigrosine's higher absorbance of NIR laser than SF.

does not absorb at any other wavelength but in the range of 200 – 300 nm. More specifically, maximal absorbance is observed at 223 nm, and another shoulder peak is observed at a wavelength of 273 nm. The main chromophores absorbing in the UV region are likely the aromatic amino acids, tyrosine, phenylalanine, and tryptophan, which are present in the silk chain.^[261] Nigrosine, on the other hand, shows a maximum absorption peak around 300 nm and another shoulder peak in the range of 500 – 650 nm. While the wavelength of the green laser lies well within the shoulder peak, the wavelength of the NIR laser is located at the lower end of the peak. Nonetheless, compared to pristine SF, nigrosine still has a higher absorbance at 850 nm than SF, as seen in the inset of **Figure 4-33**. Adding nigrosine to the SF-graphene solution neither changed the viscosity nor any other property that could potentially impact the jetting process, as the dye is water soluble and was easily incorporated. Various concentrations ranging from 1.0 – 5.0% w/v were investigated. Higher nigrosine concentrations than 1.0% w/v, however, did not significantly increase the actuation response. Therefore, bicompartamental SF fibers containing 1.0% w/v nigrosine were fabricated to

investigate the absorbance capabilities of nigrosine itself. Similar to previous light-triggered actuation experiments, the nigrosine-containing compartment of the bicompartamental fibers was exposed to NIR or green laser. With $d = 9.0 \pm 0.4 \mu\text{m}$, SF-nigrosine bicompartamental's fiber diameter is half as wide as SF-graphene bicompartamental ones due to graphene's solid nature. NIR laser induces an actuation resulting in a displacement of $x = 32.9 \pm 1.4 \mu\text{m}$, which is 2.2-fold less than the displacement induced in SF-graphene-induced fiber (**Figure 4-34A**). The green laser, on the other hand, induces 5.4-fold greater actuation and displacement of $x = 177.4 \pm 7.0 \mu\text{m}$ than triggered by NIR (**Figure 4-34B**). This significantly greater displacement compared to the NIR laser is expected, as the wavelength of the green laser lies within nigrosine's maximal absorption. Next, a combination of nigrosine and graphene is investigated to synergize and maximize the actuation response. Like bicompartamental SF-graphene fibers, these bicompartamental SF-graphene-nigrosine combinatorial fibers have a wider fiber diameter of $d = 18.0 \pm 0.2 \mu\text{m}$. As seen in **Figure 4-34C**, irradiation of the NIR laser induces a displacement from its initial position by $x = 89.4 \pm 0.8 \mu\text{m}$, which is 19.0% more than bicompartamental SF-graphene fibers without nigrosine. Under green laser, the actuation of the combinatorial bicompartamental fiber increases by another 30.0% ($x = 127.7 \pm 8.6 \mu\text{m}$) compared to SF-graphene ones under NIR irradiation (**Figure 4-34D**). In a direct comparison between all fiber types, the combinatorial fiber consisting of SF, graphene, and nigrosine outperforms all other fiber types if irradiated by NIR laser by 19.0 – 63.2%. With the green laser, however, bicompartamental SF-nigrosine fibers achieve the greatest actuation than any other fiber type. These results were expected as nigrosine's great absorption of green light is combined with the absence of graphene, which stiffens the fiber and reduces the actuation. As graphene-containing bicompartamental fibers have larger diameters than the other fiber types, the actuation displacement is divided by the

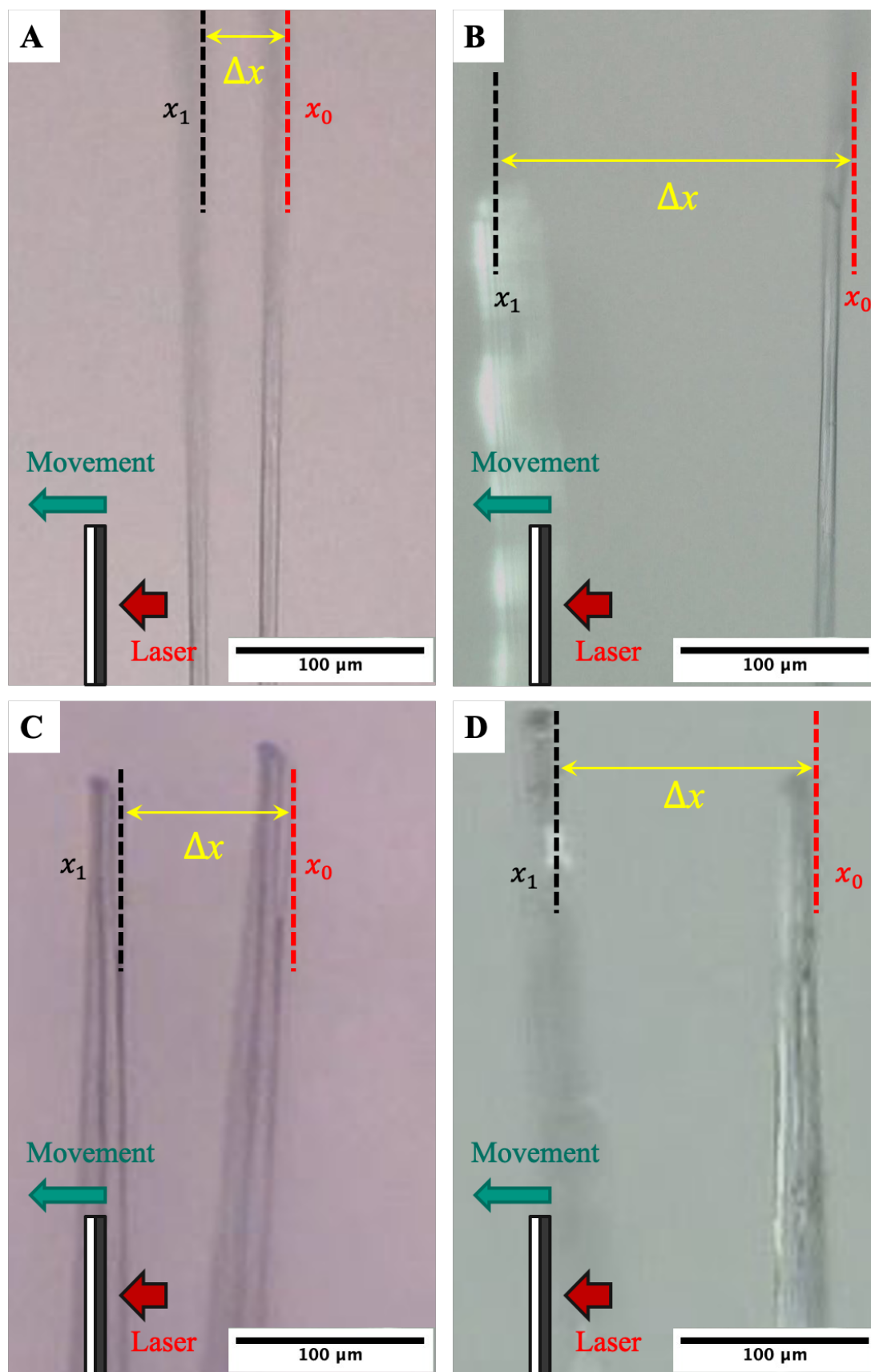


Figure 4-34: Light-triggered actuation of bicompartmental A, B) SF-nigrosine fibers and C, D) SF-graphene-nigrosine under A, C) NIR and B, D) green laser light. Light irradiation on the right fiber compartment induces a movement away from the light, towards the left side.

respective fiber diameter or surface area for better comparison between the groups (Table 4-2). Bicompartmental SF-nigrosine fibers remain the fiber type with the greatest actuation ($x/d = 19.7 \pm 0.8$). Under NIR laser, it even outperforms SF-graphene fibers under green laser irradiation by 13.5% ($x/d = 3.2 \pm 0.2$). The combinatorial fiber, as well, remains the fiber type with the greatest actuation under NIR laser exposure. Despite nigrosine's relatively low absorption at a wavelength of 850 nm compared to 565 nm, doping the SF-graphene compartment with nigrosine resulted in better actuation responses. Additional experiments with nigrosine and lower graphene concentrations should be performed to further optimize the actuation response of combinatorial fibers by adjusting the graphene-nigrosine concentration ratio. The light-responsive bicompartmental fibers show great potential for applications within the soft robotics field, as they allow for precise control when exposed to a specific wavelength of light. At the same time, these materials can be used as sensors as they can detect light and induce a response. As a potential smart switch, for instance, the actuating material can indicate an increase in temperature or overheating by bending and thus closing circuits upon NIR irradiation, which turns on signaling light-

Table 4-2: Actuation displacement of bicompartmental SF fibers under NIR and green laser. (n = 3 for all groups)

Material	Trigger	Displacement x [μm]	Diameter d [μm]	Area A [μm^2]	x/d	x/A
Dye	IR	32.9 ± 1.4	8.9 ± 0.3	62.3 ± 4.1	3.7 ± 0.3	0.5 ± 0.1
	Green	177.4 ± 7.0	9.0 ± 0.4	63.7 ± 5.8	19.7 ± 0.8	2.8 ± 0.2
Graphene	IR	72.4 ± 5.2	18.0 ± 0.2	253.6 ± 5.8	4.0 ± 0.2	0.3 ± 0.0
	Green	57.8 ± 2.9	18.0 ± 0.1	254.5 ± 2.3	3.2 ± 0.2	0.2 ± 0.0
Combi	IR	89.4 ± 0.8	18.0 ± 0.0	253.5 ± 1.3	5.0 ± 0.1	0.4 ± 0.0
	Green	127.7 ± 8.6	17.8 ± 0.2	247.9 ± 5.7	7.2 ± 0.5	0.5 ± 0.0

emitting diodes (LEDs). Another possible application is the incorporation of these fibers into textiles, which can be life-saving for the military sector. Haptic responses triggered by NIR light, which weapon sighting sources use, can alarm combat warriors of potential aiming. Moreover, future research on these bicompartmental fibers should focus on dual-light responsive actuators in which one compartment contains SF and nigrosine and will actuate under green laser exposure. The other compartment, on the other hand, consisting of SF, graphene, and nigrosine, will respond under the NIR laser, enabling a directed actuation response depending on the light.

5. Conclusion and Outlook

The main objective of this dissertation was to create and combine novel materials via electrohydrodynamic (EHD) (co)-jetting for stimuli-responsive applications and tissue engineering. Synthetic as well as natural materials were explored, which were chosen based on their differences in one or more properties to harness architectural inhomogeneity in the form of bicompartamental fibers. Combining this architectural inhomogeneity with mechanical mismatches, mechanical actuation responses, or shape reconfigurability upon exposure to various triggers, such as pH or light, could be enabled or even enhanced. Moreover, the precise control of the jet writing procedure allowed tuning scaffold geometries, which manipulated the properties of the used material.

In **Chapter 4.1**, EHD co-jet writing has been employed to design bicompartamental fibers that consist of poly(acrylic acid) (PAA), which have different crosslinker concentrations. The crosslinker is responsible for the distinct swelling of the two compartments once triggered by the actuating solution. Adding the actuating solution onto the bicompartamental hydrogel fibers namely creates an acidic-to-neutral environmental condition, which deprotonates the acrylate groups and induces swelling. Moreover, the difference in crosslinker concentration is responsible for the differential swelling of the compartments, which ultimately results in interfacial tension and forces the fiber to undergo shape reconfiguration. The controlled fiber deposition via 3D jet writing enables the design of a specific geometry inspired by a spiderweb, which allows the shape reconfiguration in a directed manner that, in turn, is inspired by a carnivorous plant. The platform's capability of actively transporting and collecting particles that mimic analytes from a large surface to a small sensing area shrinking by 99.0%, significantly enhanced analyte detectability by a 57-fold increase. This bicompartamental fiber network has also shown high separation selectivity

between various surface properties of $95 \pm 3\%$. This platform overcomes mass transport limitations currently faced in conventional microanalytical systems and establishes technological progress over the aforementioned analytical methods in terms of flexibility, specificity, and costs. Nonetheless, future studies need to investigate the platform's sensitivity as well as specificity in the presence of non-target proteins and other components within the sample solution for possible biosensing applications, as complex sample solutions can impact the fiber reconfigurability and hence, detection function. Immobilization of specific analyte binding partners via chemical vapor deposition (CVD) onto the fibers might enable the detection of more complex target analytes.

The aim of the work in **Chapter 4.2** was to design stretchable hydrogel scaffolds to study the impact of mechanical stimuli on seeded cells. Therefore, hydrogels consisting of poly(ethylene glycol diacrylate) (PEGDA) and PAA were 3D jet written via EHD jetting with pore geometries of squares, triangles, and rhombuses of various angles and heights. Once the scaffolds were UV-crosslinked, the influence of the different pore geometries on the fiber diameters and the overall homogeneity within the scaffolds were investigated. Rhombuses and triangles showed the least homogeneous fibers with widths of $w = 163.55 \pm 16.12 \mu\text{m}$ and $w = 107.46 \pm 19.84 \mu\text{m}$, respectively. The squared geometry, on the other hand, showed the thinnest and most homogeneous fibers with average widths of $w = 63.82 \pm 1.61 \mu\text{m}$. Thus, square-shaped scaffolds were fabricated with greater heights by repeating the jetting cycles five to ten times, which achieved heights of $h = 21.98 \pm 3.70 \mu\text{m}$ and $h = 29.51 \pm 1.70$, respectively. The height and jetting order of the strands, S1 and S2, also impacted the fiber widths. After five cycles, for instance, the fiber width doubled compared to the ones after one cycle. The width of fiber strands S1 and S2 remained equal within the same jetting cycle. After ten cycles, however, S1 measured fiber widths of $w = 154.23 \pm 10.99 \mu\text{m}$ and were 17.5% larger than the ones of S2, as the latter was immediately crosslinked once jetted,

preventing the uncrosslinked solution from running and flattening. Next, the square-shaped hydrogel scaffolds were mechanically tested and remained intact after 10% stretching of their initial size for 2 hours. Further, scaffolds, after five jetting cycles noticeably, broke after a strain value of $\varepsilon = 0.26 \pm 0.03$ and reached a stress value of $\sigma = 0.004 \pm 0.001$ GPa. Finally, endothelial and support cells were co-cultured on the PEGDA-PAA hydrogel scaffolds. The scaffold showed great biocompatibility and no toxicity as the seeded endothelial cells attached to the scaffold, reached a confluence, and continued to grow, which took up to nine days. The second seeding step then included the seeding of support cells, which also attached and proliferated. Overall, the hydrogel scaffolds showed great potential in terms of biocompatibility and stretchability. However, further studies need to investigate the impact of mechanical stimulation on the sprouting of the seeded cells. Therefore, the hydrogel scaffolds can be mechanically stimulated by a bioreactor to further study the complex mechanism of blood vessel sprouting and migration to drive and significantly improve tissue engineering. Understanding mechanical cues and their impact on the sprouting decisions and directions offers opportunities to enable the rational design of hierarchical vascular networks that allow the control of angiogenesis. In general, more suitable 3D environments can be designed to recreate specific tissues or improve organ transplantation as vascular architecture assists the implant's survival and functional integration within the host body.

In **Chapter 4.3**, light-responsive silk fibroin (SF) fibers were designed via EHD co-jetting. Therefore, a protocol to pre-treat graphene was developed to homogeneously disperse graphene within the SF solution. Various material combinations for the actuating compartment were explored, such as SF-graphene, SF-nigrosine, and a combination of both, SF-graphene-nigrosine. Their actuation responsiveness towards near-infrared (NIR) ($\lambda = 850$ nm, $P = 3.2$ W) and green laser light ($\lambda = 565$ nm, $P = 3.2$ W) was investigated. As graphene and nigrosine both absorb within the wavelengths of the used light sources, the

absorbed light is converted into heat. The thermal conversion subsequently induced an expansion of the SF within the compartment. The other compartment, on the other hand, consisting of pristine SF, remained unchanged as the heat induction through the light sources was not sufficient enough compared to the actuating compartment. As a result, the bicompartamental fiber mechanically actuated and bent towards the pristine SF compartment. Irrespective of the compartment being exposed to the light, an actuation was always induced in the graphene and/or nigrosine-containing compartment by SF expansion. Under NIR irradiation the actuating compartment consisting of SF, graphene, and nigrosine with 50.0% w/v, 6.7% w/v, and 1.0% w/v, respectively, exhibited the greatest actuation response ($x/d = 5.0 \pm 0.1$). Therefore, the fiber displacement from their initial position was measured and divided by their diameter. Under green laser, however, bicompartamental SF-nigrosine fibers exhibited the greatest actuation response with $x/d = 19.7 \pm 0.8$. In general, these light-responsive fibers offer promising opportunities in the field of soft robotics, as they provide precise control when detecting and responding to a specific wavelength of light. Incorporated into textiles, these fibers can induce haptic responses if triggered by NIR light, as utilized by weapon sighting sources and can serve as life-saver by alarming combat warriors. The fibers show potential for dual-light responsive actuators in which one compartment responds to NIR, while the other responds to green light. Such fibers can actuate in a directed manner depending on the light.

List of Tables

TABLE 2-1: COMMON STIMULI AND THEIR APPLICATIONAL FIELD	9
TABLE 2-2: OVERVIEW OF SOFT ACTUATORS	28
TABLE 2-3: PROPERTIES OF GRAPHENE AND ITS DERIVATIVES.	34
TABLE 3-1: USED CHEMICALS AND MATERIALS.....	35
TABLE 3-2: LIST OF USED INSTRUMENTS	36
TABLE 3-3: LIST OF USED SOFTWARE.....	37
TABLE 3-4: LIST OF POLYMER SOLUTIONS FOR JETTING	39
TABLE 4-1: EHD JETTING CONDITIONS OF VARIOUS SF CONCENTRATIONS.	95
TABLE 4-2: ACTUATION DISPLACEMENT OF BICOMPARTMENTAL SF FIBERS UNDER NIR AND GREEN.....	118

List of Figures

FIGURE 2-1: SCHEMATICS OF THE ELECTROHYDRODYNAMIC (EHD) CO-JETTING PROCESS. THE PROCESS ENABLES THE FABRICATION OF PARTICLES OR FIBERS VIA ELECTROSPRAYING OR ELECTROSPINNING RESPECTIVELY.	4
FIGURE 2-2: SEM IMAGES OF DIFFERENT SCAFFOLD GEOMETRIES FABRICATED VIA 3D JET WRITING. ^[3]	6
FIGURE 2-3: OVERVIEW OF BIOCHEMICAL, CHEMICAL AND PHYSICAL STIMULI.	7
FIGURE 2-4: CONFORMATIONAL CHANGES DUE TO APPLIED STIMULI. A) DISULFIDE BOND CLEAVAGE DUE TO HIGH GLUTATHIONE CONCENTRATION. B) AZOBENZENE ISOMERIZATION BETWEEN STABLE TRANS AND META-STABLE CIS STATE. C) PH-DEPENDENT HYDROGEL SWELLING.	12
FIGURE 2-5: ANISOTROPIC SHAPE-SHIFTING OF MULTICOMPARTMENTAL MICROCYLINDERS. A) IRREVERSIBLE SHAPE-SHIFTING OF PLGA/PMMA MICROCYLINDERS DUE TO HEATING. B) REVERSIBLE SHAPE-SHIFTING OF HYDROGEL/PLGA MICROCYLINDERS DUE TO SWELLING AND DESWELLING DEPENDING ON THE WATER OR DRY STATE, RESPECTIVELY. C) REVERSIBLE SHAPE-SHIFTING OF PEO/PVCI MICROCYLINDERS DUE TO SWELLING AND DESWELLING DEPENDING ON THE DIOXANE OR DRY STATE, RESPECTIVELY. FIGURE ADAPTED WITH PERMISSION FROM: ^[9]	14
FIGURE 2-6: THERMO-RESPONSIVE BILAYERS FOR REVERSIBLE CAPTURE AND RELEASE OF MICROPARTICLES. A) FILMS CONSISTING OF POLYCAPROLACTONE (PCL) AND POLY(N-ISOPROPYLACRYLAMIDE-CO-4-ACRYLOYLBENZOPHENONE) (POLY(NIPAM-ABP) WITH INCORPORATED MAGNETIC NANOPARTICLES IN AN UNACTUATED STATE AT ELEVATED TEMPERATURES. B) ENCAPSULATION OF MICROPARTICLES AT REDUCED TEMPERATURES VIA SELF-ROLLING MECHANISM. C) RELEASE OF MICROPARTICLES AT ELEVATED TEMPERATURES. ^[8]	15
FIGURE 2-7: STIMULI-RESPONSIVE PLANTS. A-C) MIMOSA PUDICA. LEAFLETS CLOSING DUE TO TOUCH INDUCED TRIGGER. TIME-LAPSE BETWEEN EACH IMAGE IS ABOUT 1 SECOND. D, E) DIONAEA MUSCIPULA ELLIS (VENUS FLYTRAP). D) LEAVES ARE DIVIDED INTO UPPER (UL) AND THE LOWER LEAF (LL). E) THE UPPER LEAF CONSISTS OF TWO LOBES; WHICH CENTER IS RED COLORED AND HAS THREE SENSITIVE TRIGGER HAIRS (ARROWS). ^[7]	18
FIGURE 2-8: GRAPHENE AND ITS DERIVATIVES. A) GRAPHENE. B) GRAPHENE OXIDE. C) REDUCED GRAPHENE OXIDE.	30
FIGURE 3-1: SCHEMATIC OF FIBER FORCE MEASUREMENT.	44
FIGURE 4-1: DROSERA CAPENSIS L. (DROSERACEAE). A) BEFORE AND B) AFTER ACTUATION ENTRAPPING AN INSECT. ^[1]	52
FIGURE 4-2: EHD CO-JET WRITING OF PH-RESPONSIVE POLYMER FIBERS. A) SCHEMATIC SETUP FOR BICOMPARTMENTAL FIBER PREPARATION VIA JET WRITING. B) SHAPE RECONFIGURABILITY MECHANISM DUE TO SWELLING ANISOTROPY. LIGHT MICROSCOPY IMAGES OF ACTUATING BICOMPARTMENTAL PAA FIBERS. SCALE BAR 200 μm . ^[2]	53
FIGURE 4-3: CONFOCAL IMAGES OF BICOMPARTMENTAL POLY(ACRYLIC ACID) (PAA) FIBER. IN RED, COMPARTMENT A WITH 20% ETHYLENE GLYCOL (EG); IN GREEN, COMPARTMENT B WITH 0.5% EG. A) BEFORE ACTUATION. SCALE BAR 10 μm . B) AFTER ACTUATION. COMPARTMENT B SWELLS FIVE TIMES MORE THAN COMPARTMENT A. SCALE BAR 10 AND 100 μm , RESPECTIVELY. ADAPTED FROM ^[2]	54
FIGURE 4-4: PH-DEPENDENT SWELLING OF MONO- AND BICOMPARTMENTAL FIBERS. A) SWELLING FACTOR ($N = 5$ FOR ALL GROUPS). B) CURVATURE ($N = 5$ FOR ALL GROUPS). ALL DATA IN ARE REPRESENTED AS MEAN \pm S.E.M. ADAPTED FROM ^[2] . 56	56
FIGURE 4-5: SHAPE RECONFIGURATION PROPERTIES OF BICOMPARTMENTAL FIBERS. A) CIRCULARITY ($N = 5$ FOR ALL GROUPS) AND B) ASPECT RATIO OF RECONFIGURED FIBERS ($N = 5$ FOR ALL GROUPS). AN ASPECT RATIO VALUE "1.0" INDICATES A CIRCLE, WHILE VALUE "0.0" IS INDICATING AN INCREASINGLY ELONGATED POLYGON. C) BENDING STRAIN OF BICOMPARTMENTAL FIBERS ($N = 5$ FOR ALL GROUPS). ALL DATA IN ARE REPRESENTED AS MEAN \pm S.E.M. ADAPTED FROM ^[2]	58
FIGURE 4-6: SCHEMATIC OF THE CHAMBER SETUP FOR DIRECTED PARTICLE TRANSPORT. RANDOMLY PLACED MICROSPHERES DEPOSITED ON THE SCAFFOLD, WHICH IS ACTUATED BY AN INDUCED BUFFER EXCHANGE FROM PH 3.0 – PH 7.0 VIA SYRINGE PUMPS.	62
FIGURE 4-7: DIRECTED TRANSPORT FOR ANALYTE COLLECTION. A) SCHEMATIC SETUP OF THE PH-RESPONSIVE SCAFFOLDS AND SPHERES WITHIN A CHAMBER. BRIGHT-FIELD AND SEM IMAGES OF FIBER STRUCTURES AND SPHERES BEFORE (B, D) AND AFTER (C, E) THE ACTUATION. SCALE BAR 1000 AND 500 μm , RESPECTIVELY. ^[2]	63
FIGURE 4-8: PARTICLE TRANSPORT DUE TO FIBER RECONFIGURATION OF A) CONTROL, B) 10 μm , C) 50 μm , AND D) 200 μm . ADAPTED FROM ^[2]	64
FIGURE 4-9: QUANTITATIVE REPRESENTATION OF RELATIVE SURFACE AREA COVERAGE OVER A RELATIVE TIME OF A) CONTROL, B) 10 μm , C) 50 μm , AND D) 200 μm SPHERES. TRENDLINE CONTROL ($y = -0.9724x + 0.9542$; $R^2 = 0.9902$), 10 μm SPHERES ($y = -0.9807x + 0.9318$; $R^2 = 0.9714$), 50 μm SPHERES ($y = -0.8486x + 1.0157$; $R^2 = 0.9973$), 200 μm SPHERES ($y = 0.6076x^2 - 1.4141x + 0.938$; $R^2 = 0.9821$). ADAPTED FROM ^[2]	65
FIGURE 4-10: FIBER RECONFIGURATION. A) FIBER VELOCITY AND B) RECONFIGURATION RESPONSE OF ACTUATED FIBERS WITH 10 μm , 50 μm , 200 μm SPHERES, AND CONTROL. ADAPTED FROM ^[2]	67

- FIGURE 4-11: ISOTROPY AND DIVERSION ANGLE MEASUREMENT. A)** ROI SELECTED REGIONS OF POST-PROCESSED IMAGES WITH TRACKMATE TO MEASURE THE ISOTROPY OF FIBERS WITH PARTICLES. RED INDICATING THE ISOTROPY SCORE. **B)** SCHEMATICS OF THE DIVERSION ANGLE MEASUREMENT. SOLID LINE INDICATING THE ACTUATED FIBER PATH. DOTTED LINE SHOWS THE UNACTUATED FIBER PATH. 68
- FIGURE 4-12: ANISOTROPY AND DIVERSION ANGLE. ANGULAR DISTRIBUTION OF ACTUATED FIBERS A)** WITHOUT SPHERES (N=30 FOR ALL GROUPS) AND **B)** WITH 200 μM SPHERES (N=30 FOR ALL GROUPS). **C)** QUANTITATIVE ANALYSIS OF DIVERSION ANGLE (N = 30 FOR ALL GROUPS). **D)** QUANTITATIVE ANALYSIS OF ANISOTROPY (N = 30 FOR ALL GROUPS). FOR (C) AND (D), SIGNIFICANT DIFFERENCE: ****p < 0.0001 (UNPAIRED T-TEST). ADAPTED FROM [2] 69
- FIGURE 4-13: INCREASED FLUORESCENCE INTENSITY DUE TO ENHANCED ANALYTE COLLECTION. A-D)** MICROSCOPY IMAGES AND E-H) SCATTER PLOTS AND 2D KERNEL DENSITY ESTIMATION PLOTS OF 10 μM SPHERES BEFORE (A, B, E, F) AND AFTER (C, D, G, H) THE ACTUATION. SCALE BARS 20 μM . ADAPTED FROM [2] 71
- FIGURE 4-14: EFFICIENCY OF DIRECTED PARTICLE TRANSPORT. A)** STANDARD CURVE OF FLUORESCENCE INTENSITY SIGNAL OF VARIOUS PARTICLE CONCENTRATIONS (C = 0.025, 0.05, 0.1, 0.25, 0.5, 1, 2.5, 5, 10, 15, 20, 25, 30, 35, 40, 45, 50, 60, AND 70 $\mu\text{G mL}^{-1}$; N = 3 FOR ALL GROUPS). **B)** FLUORESCENCE ENHANCEMENT FACTOR OF SPHERES AFTER ACTUATION DEPENDING ON THE INITIAL PARTICLE CONCENTRATION (C = 1, 5, 10, 15, 20, 25, 30, 35, 40, 45, AND 50 $\mu\text{G mL}^{-1}$; N = 3 FOR ALL GROUPS). **C)** SCAFFOLD TRANSPORT EFFICIENCY OF SPHERES (N = 3 FOR ALL GROUPS). DATA IN (B) AND (C) ARE REPRESENTED AS MEAN \pm S.E.M. ADAPTED FROM [2] 72
- FIGURE 4-15: SCAFFOLD SELECTIVITY FOR ANALYTE SEPARATION. SCATTER AND 2D KERNEL DENSITY ESTIMATION PLOTS OF NON-BINDING (A, B) AND BINDING (C, D) SPHERES. E)** SELECTIVITY OF NON-BINDING AND BINDING SPHERES (N = 3 FOR ALL GROUPS). CONCENTRATION OF NON-BINDING SPHERES REMAINED CONSTANT (C = 10 $\mu\text{G mL}^{-1}$). DATA IN (E) ARE REPRESENTED AS MEAN \pm S.E.M. [2] 74
- FIGURE 4-16: FIBER RECONFIGURABILITY IN COMPLEX SOLUTIONS. A)** BEFORE AND **B)** AFTER THE ADDITION OF 10% FETAL BOVINE SERUM-BASED MEDIUM. SCALE BARS 20 μM . ADAPTED FROM [2] **C)** IONIC STRENGTH IMPACT ON SWELLING BEHAVIOR OF BICOMPARTMENTAL FIBERS. [10] 77
- FIGURE 4-17: SCHEMATICS OF STRETCHABLE PEGDA-PAA HYDROGEL SCAFFOLDS FABRICATION. EHD JET WRITING OF THE HYDROGEL INK ONTO THE X-Y CONTROLLED COLLECTOR PLATE INTO PRE-PROGRAMMED STRUCTURES. CROSSLINKING VIA UV LAMP ($\lambda = 365 \text{ nm}$) UNDER NITROGEN GAS. MORE MATERIAL CAN BE DEPOSITED ON THE PREVIOUSLY JETTED AND CROSSLINKED LAYER TO CREATE 3D STRUCTURE. STEPS CAN BE REPEATED CYCLICALLY. 80**
- FIGURE 4-18: COMPLEX SCAFFOLD GEOMETRIES OF PEGDA-PAA HYDROGEL SCAFFOLDS. A, B)** SQUARES WITH 90 AND 45 ORIENTATIONS. **C)** TRIANGLES. **D, E)** RHOMBUSES WITH VARIOUS ANGLE COMBINATIONS (60°, 120° AND 10° 170°, RESPECTIVELY). **F, G)** LINES JETTED ACROSS RHOMBUS AND SQUARES, RESPECTIVELY. **H, I)** CURVED STRUCTURES. 81
- FIGURE 4-19: SCAFFOLD CHARACTERIZATION. HOMOGENEITY OF FIBER DIRECTIONALITY AND FIBER STRAND JETTING ORDER FOR A, D)** SQUARES, **B, E)** TRIANGLES, AND **C, F)** RHOMBUSES. COLOR-CODED JETTING ORDER WITH BLUE BEING THE FIRST FIBER STRAND JETTED (S1), FOLLOWED BY RED (S2), AND YELLOW (S3). FIBER WIDTH ANALYSIS IMPACTED BY JETTING ORDER OF **G)** VARIOUS GEOMETRIES AFTER ONE CYCLE AND **H)** SQUARES AFTER ONE, FIVE, AND TEN CYCLES C. 85
- FIGURE 4-20: MECHANICAL STIMULATION OF HYDROGEL SCAFFOLDS. A)** SCHEMATIC SETUP OF TENSILE TEST. **B)** STRESS-STRAIN CURVES OF SCAFFOLDS STRETCHED IN AIR OR LIQUID (N = 5 FOR ALL GROUPS). **C)** FAILURE ANALYSIS AND IMPACT OF INDIVIDUAL FAILURE POINTS ON FORCE ON A HYDROGEL SCAFFOLD IN LIQUID. 86
- FIGURE 4-21: PORE SIZE DISTRIBUTION OF STRETCHED SCAFFOLDS WITH SQUARE GEOMETRY. A)** STEPWISE IMAGE ANALYSIS VIA MATLAB TO OBTAIN INDIVIDUAL PORE SIZE DIMENSIONS. **B)** SCHEMATICS OF PORE CHANGE INDUCED BY A VERTICAL FORCE. GREEN ARROW SHOWS CHANGE IN HEIGHT. PURPLE ARROW SHOWS WIDTH CHANGE. **C)** HEIGHT AND **D)** WIDTH RATIO OF INDIVIDUAL PORES (N = 4 FOR ALL GROUPS). 88
- FIGURE 4-22: FORCE MEASUREMENTS OF CYCLIC TESTS IN E) LIQUID AND F) AIR WITH RELATIVE STANDARD DEVIATION (RSD). SCAFFOLDS IN BOTH MEDIA RUN THROUGH 7,274 STRETCHING CYCLES. IN LIQUID, THE SCAFFOLDS REMAIN INTACT UNTIL THE END OF THE EXPERIMENTS, WHILE IN THE AIR MEDIUM, THE SCAFFOLDS TEAR, AS SEEN IN THE VISIBLE FORCE DROPS. 90**
- FIGURE 4-23: SCAFFOLD BIOCOMPATIBILITY FOR VASCULAR TISSUE ENGINEERING. A)** 3D TWO-STEP CELL SEEDING PROTOCOL. [6] **B)** CLSM IMAGES OF HAMECS ON i) DAY 2, ii) DAY 5, iii) DAY 7, iv) DAY 9 AND v) ON DAY 10 WITH DPSCs. IMAGES TAKEN BY M.Sc. ORYAN KARNI KATOVICH..... 91
- FIGURE 4-24: EHD JETTING OF VARIOUS SF CONCENTRATION IN MILLI-Q WATER. A)** 10.0% w/v SF DOES NOT CREATE A JET DUE TO ITS LOW VISCOSITY, RESULTING IN DRIPPING. **B)** 20.0% w/v SF CREATES AN UNSTABLE JET WITH PARTICLES AND FIBERS. **C)** 30.0% w/v SF AND **D)** 40.0% w/v SF HAVE AN UNSTABLE WHIPPING JET, CREATING BEADED FIBERS. **E)** 50.0% w/v SF CREATES A STABLE JET FABRICATING HOMOGENEOUS FIBER. 97
- FIGURE 4-25: EHD JETTED SF FIBERS UNDER A, C) BRIGHT FIELD MICROSCOPE AND B, D) POLARIZED LIGHT MICROSCOPE. FIBERS TREATED WITH MeOH (C, D) EXHIBIT BIREFRINGENCE. 98**
- FIGURE 4-26: SF SECONDARY STRUCTURE ANALYSIS. A)** CIRCULAR DICHROISM OF UNTREATED AND METHANOL-TREATED SF FIBERS AND SF SOLUTION MEASURED BY B. POSSELT & DR. E. STRANDBERG. **B)** RAMAN SPECTROSCOPY OF UNTREATED, METHANOL-TREATED SF FIBERS, AND SF SOLUTION. UNTREATED SF FIBER AND 50.0% SILK SOLUTION SHOW MAXIMA OF METASTABLE SILK

- I FORM.^[5] MEOH-TREATED SF FIBER SHOWS NEW AND SHIFTED BANDS ATTRIBUTED TO BETA-SHEET CONFORMATION AND THE MORE STABLE SILK II FORM DUE TO METHANOL TREATMENT. SPECTRA MEASURED BY DR. S. HEIßLER. 101
- FIGURE 4-27: GRAPHENE DISPERSION WITH A) GLYCEROL (1.00 w/v) AND B) ETHYLENE GLYCOL (1.00 w/v) DENATURE SF, RESULTING IN SF AND GRAPHENE AGGLOMERATIONS. C) SOY LECITHIN (1.00 w/v) AND ETHANOL (0.01% v/v) RESULT IN AGGLOMERATIONS AS ETHANOL DENATURES SF D) SOY LECITHIN (1.00 w/v) INDUCES SMALLER GRAPHENE AGGREGATIONS. E) POLYSORBAT 20 (1.00 w/v), A NON-IONIC SURFACTANT, STABILIZES THE GRAPHENE DISPERSION IN LIQUID MEDIUM, BUT DENATURES SF AS DISPERSION TURNS MILKY. F) CALCIUM LIGNOSULFONATE (1.00% w/v) AND CREMOPHOR (0.125% v/v) SHOWS GREAT GRAPHENE DISPERSION AND SF COMPATIBILITY..... 103**
- FIGURE 4-28: PARTICLE SURFACE AREA DISTRIBUTION OF GRAPHENE DISPERSIONS. A) BEFORE ULTRASONICATION CALCIUM LIGNOSULFONATE INDUCES SMALLER GRAPHENE AGGLOMERATES COMPARED TO SOY LECITHIN. B) AFTER ULTRASONICATION WITH CALCIUM LIGNOSULFONATE, GRAPHENE PARTICLE SIZES DECREASE IN THE LOWER RANGE OF 0.01 AND 0.1 μm^2 105**
- FIGURE 4-29: EHD CO-JET WRITING OF LIGHT-RESPONSIVE SF-GRAPHENE FIBERS. A) SCHEMATIC SETUP FOR BICOMPARTMENTAL FIBER PREPARATION VIA JET WRITING OF 50.0% w/v SF AND 50.0% w/v SF WITH PRE-TREATED GRAPHENE, CALCIUM LIGNOSULFONATE (1.00% w/v) AND CREMOPHORE (0.125% v/v). B) REVERSIBLE SHAPE RECONFIGURABILITY MECHANISM DUE TO GEOMETRIC ANISOTROPY AND HEAT ABSORBANCE OF GRAPHENE RESULTING IN THE INDUCED EXPANSION OF SF. ... 107**
- FIGURE 4-30: RAMAN SPECTROSCOPY OF GRAPHENE. EXCITATION OF BICOMPARTMENTAL SF-GRAPHENE FIBER AND PRISTINE GRAPHENE AT $\lambda = 532$ NM SHOW GRAPHENE'S CHARACTERISTIC D AND G BAND AT 1350 cm^{-1} AND 1582 cm^{-1} , RESPECTIVELY.^[4] EHD JETTING PROCESS DOES NOT IMPACT GRAPHENE. SPECTRA MEASURED BY DR. S. HEIßLER. 108**
- FIGURE 4-31: TENSILE TESTS OF (BICOMPARTMENTAL) SF FIBERS. A) SETUP OF MECHANICAL TESTS. SF FIBER I) BEFORE AND II) AFTER TENSILE TEST. B) FORCE-DISPLACEMENT GRAPH OF TESTED FIBERS WITH UNTREATED SF FIBERS IN THE RANDOM COIL CONFORMATION BREAKING AT THE LOWEST FORCE. C) STRESS-STRAIN CURVES OF TESTED FIBERS SHOW UNTREATED SF-FIBERS EXHIBITING HIGHEST ELASTICITY. (N = 3 FOR ALL GROUPS). EXPERIMENTS SUPPORTED BY V. TSCHAN & DR. K.-P. WEISS. . 110**
- FIGURE 4-32: REVERSIBLE ACTUATION OF SF-GRAPHENE BICOMPARTMENTAL FIBERS WITH A) NIR ($\lambda = 850$ NM) OR B) GREEN ($\lambda = 565$ NM) LED LASER EXPOSING THE GRAPHENE COMPARTMENT, WHICH INDUCES THE SF WITHIN THE COMPARTMENT TO EXPAND, RESULTING IN A FIBER ACTUATION IN WHICH THE FIBER MOVES FROM ITS INITIAL POSITION x_0 (RED DOTTED LINE) TO x_1 (BLACK DOTTED LINE) WHILE THE LASER IS ON. ONCE THE LASER IS OFF, THE FIBER MOVES FROM x_1 BACK TO ITS INITIAL POSITION x_0 . THE TOTAL FIBER DISPLACEMENT DUE TO THE ACTUATED MOVEMENT IS Δx 113**
- FIGURE 4-33: UV-VIS OF NIGROSINE DYE AND PRISTINE SF. GREEN LASER WAVELENGTH AT $\lambda = 565$ NM (GREEN LINE) AND NIR LASER WAVELENGTH AT $\lambda = 850$ NM (PINK LINE) SHOW MAXIMUM ABSORPTION PEAK AROUND 300 NM FOR BOTH, NIGROSINE AND SF. THE GREEN LASER LIES WITHIN NIGROSINE'S SHOULDER PEAK IN THE RANGE OF 500 – 650 NM. INSET SHOWS NIGROSINE'S HIGHER ABSORBANCE OF NIR LASER THAN SF. 115**
- FIGURE 4-34: LIGHT-TRIGGERED ACTUATION OF BICOMPARTMENTAL A, B) SF-NIGROSINE FIBERS AND C, D) SF-GRAPHENE-NIGROSINE UNDER A, C) NIR AND B, D) GREEN LASER LIGHT. LIGHT IRRADIATION ON THE RIGHT FIBER COMPARTMENT INDUCES A MOVEMENT AWAY FROM THE LIGHT, TOWARDS THE LEFT SIDE. 117**

References

- [1] a) C. A. La Porta, M. C. Lionetti, S. Bonfanti, S. Milan, C. Ferrario, D. Rayneau-Kirkhope, M. Beretta, M. Hanifpour, U. Fascio, M. Ascagni, *Proceedings of the National Academy of Sciences* **2019**, 116, 18777; b) P. R. Coulet, L. J. Blum, *Biosensor principles and applications*, CRC Press, **2019**; c) P. Monti, G. Freddi, A. Bertoluzza, N. Kasai, M. Tsukada, *Journal of Raman Spectroscopy* **1998**, 29, 297; d) M. Ishida, T. Asakura, M. Yokoi, H. Saito, *Macromolecules* **1990**, 23, 88; e) P. Monti, P. Taddei, G. Freddi, T. Asakura, M. Tsukada, *Journal of Raman Spectroscopy* **2001**, 32, 103.
- [2] K. Cu, A. Steier, M. Klaiber, M. Franzreb, J. Lahann, *Advanced Functional Materials* **2022**, 32, 2204080.
- [3] J. H. Jordahl, L. Solorio, H. Sun, S. Ramcharan, C. B. Teeple, H. R. Haley, K. J. Lee, T. W. Eyster, G. D. Luker, P. H. Krebsbach, *Advanced Materials* **2018**, 30, 1707196.
- [4] A. Jorio, E. H. M. Ferreira, M. V. Moutinho, F. Stavale, C. A. Achete, R. B. Capaz, *physica status solidi (b)* **2010**, 247, 2980.
- [5] B. Frushour, J. Koenig, *Biopolymers: Original Research on Biomolecules* **1975**, 14, 2115.
- [6] A. A. Szklanny, L. Debbi, U. Merdler, D. Neale, A. Muñiz, B. Kaplan, S. Guo, J. Lahann, S. Levenberg, *Advanced Functional Materials* **2020**, 30, 1901335.
- [7] L. C. T. Scorza, M. C. Dornelas, *Plant signaling & behavior* **2011**, 6, 1979.
- [8] S. Zakharchenko, N. Puretskiy, G. Stoychev, M. Stamm, L. Ionov, *Soft Matter* **2010**, 6, 2633.
- [9] K. J. Lee, J. Yoon, S. Rahmani, S. Hwang, S. Bhaskar, S. Mitragotri, J. Lahann, *Proceedings of the National Academy of Sciences* **2012**, 109, 16057.
- [10] R. C. Disela, *M. Sc. Master thesis*, Karlsruhe Institute of Technology, **2019**.
- [11] a) J. Hoque, N. Sangaj, S. Varghese, *Macromolecular bioscience* **2019**, 19, 1800259; b) A. Chilkoti, T. Christensen, J. A. MacKay, *Current opinion in chemical biology* **2006**, 10, 652; c) A. Pourjavadi, R. Heydarpour, Z. M. Tehrani, *New Journal of Chemistry* **2021**, 45, 15705.
- [12] a) R. T. Shafranek, S. C. Millik, P. T. Smith, C.-U. Lee, A. J. Boydston, A. Nelson, *Progress in Polymer Science* **2019**, 93, 36; b) P. Theato, B. S. Sumerlin, R. K. O'Reilly, T. H. Epps III, *Chemical Society Reviews* **2013**, 42, 7055.

- [13] a) A. Yarin, *Mathematical Modelling of Natural Phenomena* **2008**, 3, 1; b) R. Yerushalmi, A. Scherz, M. E. van der Boom, H.-B. Kraatz, *Journal of Materials Chemistry* **2005**, 15, 4480.
- [14] a) L. Chen, X. Wei, Y. Sun, Y. Xue, J. Wang, Q. Wu, C. Ma, X. Yang, G. Duan, F. Wang, *Chemical Engineering Journal* **2022**, 446, 137072; b) M.-C. Chen, Z.-W. Lin, M.-H. Ling, *ACS nano* **2016**, 10, 93; c) H. Jiang, S. Kelch, A. Lendlein, *Advanced Materials* **2006**, 18, 1471; d) Y. Yu, M. Nakano, T. Ikeda, *Nature* **2003**, 425, 145.
- [15] a) I. Banerjee, D. Mishra, T. Das, T. K. Maiti, *Journal of biomaterials science, polymer Edition* **2012**, 23, 111; b) Z. Deng, Z. Zhen, X. Hu, S. Wu, Z. Xu, P. K. Chu, *Biomaterials* **2011**, 32, 4976; c) H. Ding, P. Tan, S. Fu, X. Tian, H. Zhang, X. Ma, Z. Gu, K. Luo, *Journal of Controlled Release* **2022**, 348, 206; d) L.-c. Dong, A. S. Hoffman, *Journal of Controlled Release* **1991**, 15, 141.
- [16] a) H. Feil, Y. Bae, J. Feijen, S. W. Kim, *Macromolecules* **1992**, 25, 5528; b) S. Gao, A. Zhou, B. Cao, J. Wang, F. Li, G. Tang, Z. Jiang, A. Yang, R. Xiong, J. Lei, *New Journal of Chemistry* **2021**, 45, 13056; c) T. Okano, Y. H. Bae, S. W. Kim, *Pulsed and self-regulated drug delivery* **1990**, 17.
- [17] a) J. Ge, E. Neofytou, T. J. Cahill III, R. E. Beygui, R. N. Zare, *ACS nano* **2012**, 6, 227; b) X. Shi, Y. Zheng, C. Wang, L. Yue, K. Qiao, G. Wang, L. Wang, H. Quan, *RSC Advances* **2015**, 5, 41820.
- [18] a) W. L. Zhang, H. J. Choi, *Polymers* **2014**, 6, 2803; b) D. Wang, W. Xie, Q. Gao, H. Yan, J. Zhang, J. Lu, B. Liaw, Z. Guo, F. Gao, L. Yin, *Small* **2019**, 15, 1900511.
- [19] S. Guragain, B. P. Bastakoti, V. Malgras, K. Nakashima, Y. Yamauchi, *Chemistry–A European Journal* **2015**, 21, 13164.
- [20] a) M. Qu, X. Jiang, X. Zhou, C. Wang, Q. Wu, L. Ren, J. Zhu, S. Zhu, P. Tebon, W. Sun, *Advanced healthcare materials* **2020**, 9, 1901714; b) V. Taresco, C. Alexander, N. Singh, A. K. Pearce, *Advanced Therapeutics* **2018**, 1, 1800030; c) A. Alsuraifi, A. Curtis, D. A. Lamprou, C. Hoskins, *Pharmaceutics* **2018**, 10, 136; d) X. Zhao, J. Bai, W. Yang, *Cancer Biology & Medicine* **2021**, 18, 319; e) F. Andrade, M. M. Roca-Melendres, E. F. Durán-Lara, D. Rafael, S. Schwartz Jr, *Cancers* **2021**, 13, 1164; f) L. Li, Z. Yang, X. Chen, *Accounts of Chemical Research* **2020**, 53, 2044.
- [21] a) X. S. Chen, J. J. Moon, J. Cheon, Vol. 53, ACS Publications, 2020, 2763; b) X. Ma, X. Li, J. Shi, M. Yao, X. Zhang, R. Hou, N. Shao, Q. Luo, Y. Gao, S. Du, *Advanced Healthcare Materials* **2019**, 8, 1900661.

- [22] Y. Huang, L. Zou, J. Wang, Q. Jin, J. Ji, *Wiley Interdisciplinary Reviews: Nanomedicine and Nanobiotechnology* **2022**, 14, e1775.
- [23] S. Thamphiwatana, V. Fu, J. Zhu, D. Lu, W. Gao, L. Zhang, *Langmuir* **2013**, 29, 12228.
- [24] a) L. Hines, K. Petersen, G. Z. Lum, M. Sitti, *Advanced materials* **2017**, 29, 1603483; b) P. Polygerinos, Z. Wang, J. T. Overvelde, K. C. Galloway, R. J. Wood, K. Bertoldi, C. J. Walsh, *IEEE Transactions on Robotics* **2015**, 31, 778; c) K. Suzumori, S. Endo, T. Kanda, N. Kato, H. Suzuki, presented at Proceedings 2007 IEEE international conference on robotics and automation **2007**.
- [25] a) Y. Lee, W. Song, J.-Y. Sun, *Materials Today Physics* **2020**, 15, 100258; b) Z. Li, Y. Zhou, T. Li, J. Zhang, H. Tian, *View* **2022**, 3, 20200112.
- [26] a) Y. Sun, L. Chen, Y. Jiang, X. Zhang, X. Yao, S. Soh, *Materials Horizons* **2019**, 6, 160; b) C. Yoon, *Nano Convergence* **2019**, 6, 1.
- [27] a) K. Yoshida, H. Onoe, *Advanced Intelligent Systems* **2020**, 2, 2000095; b) S. V. Nikolov, P. D. Yeh, A. Alexeev, *ACS Macro Letters* **2015**, 4, 84.
- [28] a) W. Francis, A. Dunne, C. Delaney, L. Florea, D. Diamond, *Sensors and Actuators B: Chemical* **2017**, 250, 608; b) Y. Chen, Y. Zhang, H. Li, J. Shen, F. Zhang, J. He, J. Lin, B. Wang, S. Niu, Z. Han, *Nano Today* **2023**, 49, 101764.
- [29] E. Karshalev, R. Kumar, I. Jeerapan, R. Castillo, I. Campos, J. Wang, *Chemistry of Materials* **2018**, 30, 1593.
- [30] K. Malachowski, J. Breger, H. R. Kwag, M. O. Wang, J. P. Fisher, F. M. Selaru, D. H. Gracias, *Angewandte Chemie International Edition* **2014**, 53, 8045.
- [31] C. M. Magin, D. L. Alge, K. S. Anseth, *Biomedical Materials* **2016**, 11, 022001.
- [32] S.-E. Kim, P. W. Lee, J. K. Pokorski, *ACS macro letters* **2017**, 6, 593.
- [33] C. Chen, Y. Liu, H. Wang, G. Chen, X. Wu, J. Ren, H. Zhang, Y. Zhao, *ACS nano* **2018**, 12, 10493.
- [34] T. G. Park, A. S. Hoffman, *Macromolecules* **1993**, 26, 5045.
- [35] S. K. Singh, A. Subramanian, *RSC Advances* **2020**, 10, 25022.
- [36] S. Rahmani, J. Lahann, *MRS Bulletin* **2014**, 39, 251.
- [37] K. H. Choi, M. Zubair, H. W. Dang, *Japanese Journal of Applied Physics* **2014**, 53, 05HB02.
- [38] Y. Liang, J. Yong, Y. Yu, A. Nirmalathas, K. Ganesan, R. Evans, B. Nasr, E. Skafidas, *ACS nano* **2019**, 13, 13957.

- [39] Y. Ahn, S. Park, G. Kim, Y. Hwang, C. Lee, H. Shin, J. Lee, *Current Applied Physics* **2006**, 6, 1030.
- [40] K. Shigeta, Y. He, E. Sutanto, S. Kang, A.-P. Le, R. G. Nuzzo, A. G. Alleyne, P. M. Ferreira, Y. Lu, J. A. Rogers, *Analytical chemistry* **2012**, 84, 10012.
- [41] a) M. S. Onses, E. Sutanto, P. M. Ferreira, A. G. Alleyne, J. A. Rogers, *Small* **2015**, 11, 4237; b) T. D. Brown, N. Habibi, D. Wu, J. Lahann, S. Mitragotri, *ACS Biomaterials Science & Engineering* **2020**, 6, 4916.
- [42] a) M. De, P. S. Ghosh, V. M. Rotello, *Advanced Materials* **2008**, 20, 4225; b) O. V. Salata, *Journal of nanobiotechnology* **2004**, 2, 1.
- [43] a) D. A. Groneberg, M. Giersig, T. Welte, U. Pison, *Current drug targets* **2006**, 7, 643; b) D. F. Emerich, C. G. Thanos, *Journal of drug targeting* **2007**, 15, 163.
- [44] a) C. P. Reis, R. J. Neufeld, A. J. Ribeiro, F. Veiga, *Nanomedicine: Nanotechnology, Biology and Medicine* **2006**, 2, 8; b) K. S. Soppimath, T. M. Aminabhavi, A. R. Kulkarni, W. E. Rudzinski, *Journal of controlled release* **2001**, 70, 1.
- [45] a) N. Kumar, M. N. Ravikumar, A. Domb, *Advanced drug delivery reviews* **2001**, 53, 23; b) L. Illum, S. Davis, R. Müller, E. Mak, P. West, *Life sciences* **1987**, 40, 367; c) J. M. Harris, R. B. Chess, *Nature reviews Drug discovery* **2003**, 2, 214.
- [46] J. Zeleny, *Physical Review* **1914**, 3, 69.
- [47] N. Bhardwaj, S. C. Kundu, *Biotechnology advances* **2010**, 28, 325.
- [48] a) S. Vijayavenkataraman, S. Zhang, W. F. Lu, J. Y. H. Fuh, *Journal of Materials Research* **2018**, 33, 1999; b) W. J. Li, C. T. Laurencin, E. J. Caterson, R. S. Tuan, F. K. Ko, *Journal of Biomedical Materials Research: An Official Journal of The Society for Biomaterials, The Japanese Society for Biomaterials, and The Australian Society for Biomaterials and the Korean Society for Biomaterials* **2002**, 60, 613.
- [49] a) H.-J. Jin, S. V. Fridrikh, G. C. Rutledge, D. L. Kaplan, *Biomacromolecules* **2002**, 3, 1233; b) J. Jia, Y.-Y. Duan, S.-H. Wang, S.-F. Zhang, Z.-Y. Wang, *Journal of US-China Medical Science* **2007**, 4, 52.
- [50] J. Zeng, X. Xu, X. Chen, Q. Liang, X. Bian, L. Yang, X. Jing, *Journal of controlled release* **2003**, 92, 227.
- [51] a) E.-R. Kenawy, G. L. Bowlin, K. Mansfield, J. Layman, D. G. Simpson, E. H. Sanders, G. E. Wnek, *Journal of controlled release* **2002**, 81, 57; b) J. Kost, R. Langer, *Advanced drug delivery reviews* **2012**, 64, 327; c) K. Kim, Y. K. Luu, C.

- Chang, D. Fang, B. S. Hsiao, B. Chu, M. Hadjiargyrou, *Journal of controlled release* **2004**, 98, 47.
- [52] a) I. Bružauskaitė, D. Bironaitė, E. Bagdonas, E. Bernotienė, *Cytotechnology* **2016**, 68, 355; b) B. D. Boyan, T. W. Hummert, D. D. Dean, Z. Schwartz, *Biomaterials* **1996**, 17, 137.
- [53] a) J. E. Dennis, S. E. Haynesworth, R. G. Young, A. I. Caplan, *Cell transplantation* **1992**, 1, 23; b) H. Nakahara, V. M. Goldberg, A. I. Caplan, *Clinical Orthopaedics and Related Research®* **1992**, 276, 291.
- [54] P. Eggli, W. Moller, R. Schenk, *Clinical Orthopaedics and Related Research®* **1988**, 232, 127.
- [55] T. Shirakura, T. J. Kelson, A. Ray, A. E. Malyarenko, R. Kopelman, *ACS macro letters* **2014**, 3, 602.
- [56] K. Asaka, K. Oguro, *Journal of Electroanalytical Chemistry* **2000**, 480, 186.
- [57] P. M. Xulu, G. Filipcsei, M. Zrinyi, *Macromolecules* **2000**, 33, 1716.
- [58] H. S. Kim, A. J. Crosby, *Advanced materials* **2011**, 23, 4188.
- [59] a) W. Gao, J. M. Chan, O. C. Farokhzad, *Molecular pharmaceutics* **2010**, 7, 1913; b) Y. J. Zhu, F. Chen, *Chemistry—An Asian Journal* **2015**, 10, 284.
- [60] a) H. Chen, D. Liu, Z. Guo, *Chemistry Letters* **2016**, 45, 242; b) R. Li, F. Peng, J. Cai, D. Yang, P. Zhang, *Asian journal of pharmaceutical sciences* **2020**, 15, 311.
- [61] a) G. Lee, Y. S. Choi, H.-J. Yoon, J. A. Rogers, *Matter* **2020**, 3, 1031; b) J. Niu, Z. Chen, J. Zhao, G. Cui, *Science China Materials* **2022**, 65, 2060.
- [62] Z. Deng, R. Yu, B. Guo, *Materials Chemistry Frontiers* **2021**, 5, 2092.
- [63] X. Zhang, S. Soh, *Advanced Materials* **2017**, 29, 1606483.
- [64] a) C. Zhang, H. Deng, Y. Xie, C. Zhang, J. W. Su, J. Lin, *Small* **2019**, 15, 1904224; b) Q. Zhang, X. Liu, L. Duan, G. Gao, *Chemical Engineering Journal* **2019**, 365, 10.
- [65] V. Trovato, S. Sfameni, G. Rando, G. Rosace, S. Libertino, A. Ferri, M. R. Plutino, *Molecules* **2022**, 27, 5709.
- [66] J. P. Mercier, G. Zambelli, W. Kurz, *Introduction to materials science*, Elsevier, **2012**.
- [67] J. C.-M. Li, *Microstructure and properties of materials*, world scientific, **1996**.
- [68] a) Z. Wang, C. Yang, Z. Yang, C. E. Brown, B. P. Hollebone, S. A. Stout, in *Standard handbook oil spill environmental forensics*, Elsevier **2016**, p. 131; b) C. Dugave, L. Demange, *Chemical reviews* **2003**, 103, 2475.

- [69] a) T. G. Fox Jr, P. J. Flory, *Journal of the American Chemical Society* **1948**, 70, 2384; b) R. H. Colby, L. J. Fetters, W. W. Graessley, *Macromolecules* **1987**, 20, 2226.
- [70] J. March, **1968**.
- [71] D. Yang, W. Chen, J. Hu, *The Journal of Physical Chemistry B* **2014**, 118, 12311.
- [72] Y. Li, Q. Wu, M. Kang, N. Song, D. Wang, B. Z. Tang, *Biomaterials* **2020**, 232, 119749.
- [73] S. Mura, J. Nicolas, P. Couvreur, *Nature materials* **2013**, 12, 991.
- [74] Y. Liu, L. Qiao, S. Zhang, G. Wan, B. Chen, P. Zhou, N. Zhang, Y. Wang, *Acta biomaterialia* **2018**, 66, 310.
- [75] Y. Gao, K. Y. Wong, A. Ahiabu, M. J. Serpe, *Journal of Materials Chemistry B* **2016**, 4, 5144.
- [76] C. J. Barrett, J.-i. Mamiya, K. G. Yager, T. Ikeda, *Soft Matter* **2007**, 3, 1249.
- [77] a) G. Stoychev, S. Zakharchenko, S. Turcaud, J. W. Dunlop, L. Ionov, *ACS nano* **2012**, 6, 3925; b) H. Lee, C. Xia, N. X. Fang, *Soft Matter* **2010**, 6, 4342; c) Y. Ma, Y. Zhang, B. Wu, W. Sun, Z. Li, J. Sun, *Angewandte Chemie* **2011**, 123, 6378; d) G. Stoychev, S. Turcaud, J. W. Dunlop, L. Ionov, *Advanced Functional Materials* **2013**, 23, 2295.
- [78] K. Balani, V. Verma, A. Agarwal, R. Narayan, *Biosurfaces: a materials science and engineering perspective*, John Wiley & Sons, **2015**.
- [79] a) Y. Zhang, L. Ionov, *Langmuir* **2015**, 31, 4552; b) A. Kirillova, R. Maxson, G. Stoychev, C. T. Gomillion, L. Ionov, *Advanced Materials* **2017**, 29, 1703443; c) G. Stoychev, C. Reuther, S. Diez, L. Ionov, *Angewandte Chemie* **2016**, 128, 16340.
- [80] S. Moon, M. S. Jones, E. Seo, J. Lee, L. Lahann, J. H. Jordahl, K. J. Lee, J. Lahann, *Science advances* **2021**, 7, eabf5289.
- [81] J.-W. Yoo, S. Mitragotri, *Proceedings of the National Academy of Sciences* **2010**, 107, 11205.
- [82] J. Lee, T. H. Park, K. J. Lee, J. Lahann, *Macromolecular rapid communications* **2016**, 37, 73.
- [83] A. Azam, K. E. Laflin, M. Jamal, R. Fernandes, D. H. Gracias, *Biomedical microdevices* **2011**, 13, 51.
- [84] a) K.-U. Jeong, J.-H. Jang, D.-Y. Kim, C. Nah, J. H. Lee, M.-H. Lee, H.-J. Sun, C.-L. Wang, S. Z. Cheng, E. L. Thomas, *Journal of Materials Chemistry* **2011**, 21, 6824; b)

- S. M. Felton, M. T. Tolley, B. Shin, C. D. Onal, E. D. Demaine, D. Rus, R. J. Wood, *Soft Matter* **2013**, 9, 7688.
- [85] M. Jamal, A. M. Zarafshar, D. H. Gracias, *Nature communications* **2011**, 2, 527.
- [86] L. Verhage, G. C. Angenent, R. G. Immink, *Trends in plant science* **2014**, 19, 583.
- [87] A. Huxley, 1992.
- [88] A. G. Volkov, T. Adesina, V. S. Markin, E. Jovanov, *Plant physiology* **2008**, 146, 694.
- [89] A. G. Volkov, H. Carrell, T. Adesina, V. S. Markin, E. Jovanov, *Plant Signaling & Behavior* **2008**, 3, 490.
- [90] a) W. R. Fagerberg, D. Allain, *American Journal of Botany* **1991**, 78, 647; b) A. G. Volkov, M.-R. Pinnock, D. C. Lowe, S. G. Ma'Resha, V. S. Markin, *Journal of plant physiology* **2011**, 168, 109; c) A. G. Volkov, T. Adesina, E. Jovanov, *Plant signaling & behavior* **2007**, 2, 139.
- [91] C. Darwin, F. Darwin, *Insectivorous Plants*, J. Murray, **1888**.
- [92] L. Xu, G. Gu, presented at 2017 24th International Conference on Mechatronics and Machine Vision in Practice (M2VIP) **2017**.
- [93] W. Hong, A. Almomani, Y. Chen, R. Jamshidi, R. Montazami, *Materials* **2017**, 10, 664.
- [94] H. Lim, T. Park, J. Na, C. Park, B. Kim, E. Kim, *NPG Asia Materials* **2017**, 9, e399.
- [95] J. B. Park, J. D. Bronzino, *Biomaterials: principles and applications*, crc press, **2002**.
- [96] S. D. Bruck, *The International Journal of Artificial Organs* **1990**, 13, 469.
- [97] a) R. Langer, D. A. Tirrell, *Nature* **2004**, 428, 487; b) D. G. Anderson, J. A. Burdick, R. Langer, *Science* **2004**, 305, 1923.
- [98] a) O. S. Fenton, K. N. Olafson, P. S. Pillai, M. J. Mitchell, R. Langer, *Advanced Materials* **2018**, 30, 1705328; b) R. Langer, N. A. Peppas, *AIChE Journal* **2003**, 49, 2990.
- [99] C. Vepari, D. L. Kaplan, *Progress in polymer science* **2007**, 32, 991.
- [100] D. M. Phillips, L. F. Drummy, D. G. Conrady, D. M. Fox, R. R. Naik, M. O. Stone, P. C. Trulove, H. C. De Long, R. A. Mantz, *Journal of the American chemical society* **2004**, 126, 14350.
- [101] a) B. Kundu, R. Rajkhowa, S. C. Kundu, X. Wang, *Advanced drug delivery reviews* **2013**, 65, 457; b) C. Z. Zhou, F. Confalonieri, M. Jacquet, R. Perasso, Z. G. Li, J. Janin, *Proteins: Structure, Function, and Bioinformatics* **2001**, 44, 119.

- [102] a) H.-J. Jin, D. L. Kaplan, *Nature* **2003**, 424, 1057; b) R. E. Marsh, R. B. Corey, L. Pauling, *Biochimica et Biophysica acta* **1955**, 16, 1; c) Y. Takahashi, M. Gehoh, K. Yuzuriha, *International journal of biological macromolecules* **1999**, 24, 127.
- [103] a) Y. Suzuki, *Biochemical Differentiation in Insect Glands* **1977**, 1; b) Y. Tashiro, T. Morimoto, S. Matsuura, S. Nagata, *The Journal of cell biology* **1968**, 38, 574.
- [104] a) D. Kaplan, K. McGrath, *Protein-based materials*, Springer Science & Business Media, **1997**; b) J. Magoshi, S. Nakamura, *Journal of Polymer Science: Polymer Physics Edition* **1985**, 23, 227.
- [105] a) J. G. Hardy, L. M. Römer, T. R. Scheibel, *Polymer* **2008**, 49, 4309; b) D. N. Rockwood, R. C. Preda, T. Yücel, X. Wang, M. L. Lovett, D. L. Kaplan, *Nature protocols* **2011**, 6, 1612.
- [106] N. Kasoju, U. Bora, *Advanced healthcare materials* **2012**, 1, 393.
- [107] a) V. Karageorgiou, L. Meinel, S. Hofmann, A. Malhotra, V. Volloch, D. Kaplan, *Journal of Biomedical Materials Research Part A: An Official Journal of The Society for Biomaterials, The Japanese Society for Biomaterials, and The Australian Society for Biomaterials and the Korean Society for Biomaterials* **2004**, 71, 528; b) P. C. Bessa, M. Casal, R. Reis, *Journal of tissue engineering and regenerative medicine* **2008**, 2, 81.
- [108] A. Mescher, *Translate by: Naderan M, Naderan M, Noori Moogehi SMH. 1st. Tehran: Teimourzadeh Publications* **2011**.
- [109] C. Li, C. Vepari, H.-J. Jin, H. J. Kim, D. L. Kaplan, *Biomaterials* **2006**, 27, 3115.
- [110] S. Y. Park, C. S. Ki, Y. H. Park, H. M. Jung, K. M. Woo, H. J. Kim, *Tissue Engineering Part A* **2010**, 16, 1271.
- [111] a) X. Zhang, C. B. Baughman, D. L. Kaplan, *Biomaterials* **2008**, 29, 2217; b) L. Soffer, X. Wang, X. Zhang, J. Kluge, L. Dorfmann, D. L. Kaplan, G. Leisk, *Journal of Biomaterials Science, Polymer Edition* **2008**, 19, 653; c) X. Zhang, X. Wang, V. Keshav, X. Wang, J. T. Johanas, G. G. Leisk, D. L. Kaplan, *Biomaterials* **2009**, 30, 3213.
- [112] R. Lanza, R. Langer, J. P. Vacanti, A. Atala, *Principles of tissue engineering*, Academic press, **2020**.
- [113] M. S. Chapekar, *Journal of Biomedical Materials Research: An Official Journal of The Society for Biomaterials, The Japanese Society for Biomaterials, and The*

- Australian Society for Biomaterials and the Korean Society for Biomaterials* **2000**, 53, 617.
- [114] A. Crupi, A. Costa, A. Tarnok, S. Melzer, L. Teodori, *European journal of immunology* **2015**, 45, 3222.
- [115] a) R. E. Horch, J. Kopp, U. Kneser, J. Beier, A. D. Bach, *Journal of cellular and molecular medicine* **2005**, 9, 592; b) W. H. Eaglstein, V. Falanga, *Clinical therapeutics* **1997**, 19, 894; c) D. W. Hutmacher, *Biomaterials* **2000**, 21, 2529; d) B. D. Boyan, C. H. Lohmann, J. Romero, Z. Schwartz, *Clinics in plastic surgery* **1999**, 26, 629.
- [116] S. Heydarkhan-Hagvall, K. Schenke-Layland, A. P. Dhanasopon, F. Rofail, H. Smith, B. M. Wu, R. Shemin, R. E. Beygui, W. R. MacLellan, *Biomaterials* **2008**, 29, 2907.
- [117] Y. Ikada, *Journal of the Royal Society Interface* **2006**, 3, 589.
- [118] D. Eberli, *Regenerative Medicine and Tissue Engineering: Cells and Biomaterials*, BoD–Books on Demand, **2011**.
- [119] B. Weber, M. Y. Emmert, R. Schoenauer, C. Brokopp, L. Baumgartner, S. P. Hoerstrup, presented at Seminars in immunopathology **2011**.
- [120] B.-S. Kim, D. J. Mooney, *Trends in biotechnology* **1998**, 16, 224.
- [121] D. Schmidt, U. A. Stock, S. P. Hoerstrup, *Philosophical Transactions of the Royal Society B: Biological Sciences* **2007**, 362, 1505.
- [122] M. S. B. Reddy, D. Ponnamma, R. Choudhary, K. K. Sadasivuni, *Polymers* **2021**, 13, 1105.
- [123] T. Hoshiba, H. Lu, N. Kawazoe, G. Chen, *Expert opinion on biological therapy* **2010**, 10, 1717.
- [124] a) J. R. Jones, L. L. Hench, *Journal of Biomedical Materials Research Part B: Applied Biomaterials: An Official Journal of The Society for Biomaterials, The Japanese Society for Biomaterials, and The Australian Society for Biomaterials and the Korean Society for Biomaterials* **2004**, 68, 36; b) Y. Zhang, M. Zhang, D. Cheng, S. Xu, C. Du, L. Xie, W. Zhao, *Biomaterials Science* **2022**.
- [125] a) Q. L. Loh, C. Choong, **2013**; b) E. M. Christenson, W. Soofi, J. L. Holm, N. R. Cameron, A. G. Mikos, *Biomacromolecules* **2007**, 8, 3806.
- [126] Y. Ikada, *Tissue engineering: fundamentals and applications*, Elsevier, **2011**.
- [127] K. Whang, K. Healy, *Methods of tissue engineering* **2002**, 697.

- [128] S. Sahoo, L. T. Ang, J. C. H. Goh, S. L. Toh, *Journal of Biomedical Materials Research Part A: An Official Journal of The Society for Biomaterials, The Japanese Society for Biomaterials, and The Australian Society for Biomaterials and the Korean Society for Biomaterials* **2010**, 93, 1539.
- [129] a) F.-M. Chen, M. Zhang, Z.-F. Wu, *Biomaterials* **2010**, 31, 6279; b) J. E. Babensee, L. V. McIntire, A. G. Mikos, *Pharmaceutical research* **2000**, 17, 497.
- [130] a) M. W. Laschke, M. D. Menger, *Biotechnology advances* **2016**, 34, 112; b) G. K. Naughton, *Annals of the New York Academy of Sciences* **2002**, 961, 372.
- [131] a) D. I. f. N. e.V; b) D. I. f. N. e.V.
- [132] a) V. Mani, T. Beduk, W. Khushaim, A. E. Ceylan, S. Timur, O. S. Wolfbeis, K. N. Salama, *TrAC Trends in Analytical Chemistry* **2021**, 135, 116164; b) H. A. Byrne, K. L. Tieszen, S. Hollis, T. L. Dornan, J. P. New, *Diabetes care* **2000**, 23, 500; c) M. Sekar, M. Pandiaraj, S. Bhansali, N. Ponpandian, C. Viswanathan, *Scientific reports* **2019**, 9, 403.
- [133] U. Guth, W. Vonau, J. Zosel, *Measurement Science and Technology* **2009**, 20, 042002.
- [134] a) D. R. Reyes, D. Iossifidis, P.-A. Auroux, A. Manz, *Analytical chemistry* **2002**, 74, 2623; b) Y. Song, B. Lin, T. Tian, X. Xu, W. Wang, Q. Ruan, J. Guo, Z. Zhu, C. Yang, *Analytical chemistry* **2018**, 91, 388; c) F. Wieland, R. Bruch, M. Bergmann, S. Partel, G. A. Urban, C. Dincer, *Polymers* **2020**, 12, 104.
- [135] a) A. Sitt, H. Hess, *Nano letters* **2015**, 15, 3341; b) P. Katira, H. Hess, *Nano letters* **2010**, 10, 567; c) M. Lin, J. Wang, G. Zhou, J. Wang, N. Wu, J. Lu, J. Gao, X. Chen, J. Shi, X. Zuo, *Angewandte Chemie* **2015**, 127, 2179; d) X. Qu, F. Yang, H. Chen, J. Li, H. Zhang, G. Zhang, L. Li, L. Wang, S. Song, Y. Tian, *ACS applied materials & interfaces* **2017**, 9, 16026.
- [136] a) R. J. White, H. S. White, ACS Publications, 2005; b) P. E. Sheehan, L. J. Whitman, *Nano letters* **2005**, 5, 803; c) M. Zhao, X. Wang, D. Nolte, *Biomedical Optics Express* **2010**, 1, 983.
- [137] T. Nitta, H. Hess, *Cellular and Molecular Bioengineering* **2013**, 6, 109.
- [138] a) S. Ramachandran, K. H. Ernst, G. D. Bachand, V. Vogel, H. Hess, *Small* **2006**, 2, 330; b) D. Inoue, T. Nitta, A. M. R. Kabir, K. Sada, J. P. Gong, A. Konagaya, A. Kakugo, *Nature communications* **2016**, 7, 1; c) A. J. Wollman, C. Sanchez-Cano, H. M. Carstairs, R. A. Cross, A. J. Turberfield, *Nature nanotechnology* **2014**, 9, 44.

- [139] R. Ibusuki, T. Morishita, A. Furuta, S. Nakayama, M. Yoshio, H. Kojima, K. Oiwa, K. y. Furuta, *Science* **2022**, 375, 1159.
- [140] a) T. J. Grove, K. A. Puckett, N. M. Brunet, G. Mihajlovic, L. A. McFadden, P. Xiong, S. von Molnár, T. S. Moerland, P. B. Chase, *IEEE Transactions on Advanced Packaging* **2005**, 28, 556; b) R. Seetharam, Y. Wada, S. Ramachandran, H. Hess, P. Satir, *Lab on a Chip* **2006**, 6, 1239; c) M. A. Rahman, C. Reuther, F. W. Lindberg, M. Mengoni, A. Salhotra, G. Heldt, H. Linke, S. Diez, A. Månsson, *Nano letters* **2019**, 19, 7155; d) M. Lard, L. Ten Siethoff, S. Kumar, M. Persson, G. Te Kronnie, H. Linke, A. Månsson, *Biosensors and Bioelectronics* **2013**, 48, 145.
- [141] a) S. Zhang, S. J. Kieffer, C. Zhang, A. G. Alleyne, P. V. Braun, *Advanced Materials* **2018**, 30, 1803140; b) N. Yonet-Tanyeri, R. C. Evans, H. Tu, P. V. Braun, *Advanced Materials* **2011**, 23, 1739; c) H.-J. Koo, K. V. Waynant, C. Zhang, P. V. Braun, *ACS applied materials & interfaces* **2014**, 6, 14320; d) T. H. Tsai, M. A. Ali, Z. Jiang, P. V. Braun, *Angewandte Chemie International Edition* **2017**, 56, 5001; e) S. Zhang, C. Zhang, H. Chen, S. J. Kieffer, F. Neubrech, H. Giessen, A. G. Alleyne, P. V. Braun, *Angewandte Chemie* **2019**, 131, 18333.
- [142] S. M. Desai, R. Singh, in *Long Term Properties of Polyolefins*, Springer **2004**, p. 231.
- [143] J. M. Goddard, J. Hotchkiss, *Progress in polymer science* **2007**, 32, 698.
- [144] a) N. Inagaki, *Plasma surface modification and plasma polymerization*, CRC press, **2014**; b) S. Morgenthaler, C. Zink, N. D. Spencer, *Soft matter* **2008**, 4, 419.
- [145] D. Rus, M. T. Tolley, *Nature* **2015**, 521, 467.
- [146] C. Lee, M. Kim, Y. J. Kim, N. Hong, S. Ryu, H. J. Kim, S. Kim, *International Journal of Control, Automation and Systems* **2017**, 15, 3.
- [147] K. Jung, J. C. Koo, Y. K. Lee, H. R. Choi, *Bioinspiration & biomimetics* **2007**, 2, S42.
- [148] N. El-Atab, R. B. Mishra, F. Al-Modaf, L. Joharji, A. A. Alsharif, H. Alamoudi, M. Diaz, N. Qaiser, M. M. Hussain, *Advanced Intelligent Systems* **2020**, 2, 2000128.
- [149] J. Shintake, S. Rosset, B. Schubert, D. Floreano, H. Shea, *Advanced materials* **2016**, 28, 231.
- [150] a) S. Shian, D. R. Clarke, *Soft Matter* **2016**, 12, 3137; b) E. Torenbeek, *Synthesis of subsonic airplane design: an introduction to the preliminary design of subsonic general aviation and transport aircraft, with emphasis on layout, aerodynamic design, propulsion and performance*, Springer Science & Business Media, **2013**.

- [151] a) X. Zhang, G. Zhang, K. Nakamura, S. Ueha, *Sensors and Actuators A: Physical* **2011**, 169, 206; b) G. A. Hollinger, J. M. Briscoe, presented at Proceedings of the 2005 IEEE International Conference on Robotics and Automation **2005**; c) T. Ho, S. Lee, *Journal of Bionic Engineering* **2009**, 6, 29; d) A. Ming, Y. Huang, Y. Fukushima, M. Shimojo, presented at 2008 IEEE International Conference on Robotics and Biomimetics **2009**.
- [152] a) D. D. Chin, L. Y. Matloff, A. K. Stowers, E. R. Tucci, D. Lentink, *Journal of the Royal Society Interface* **2017**, 14, 20170240; b) A. Hedenström, G. Norevik, K. Warfvinge, A. Andersson, J. Bäckman, S. Åkesson, *Current Biology* **2016**, 26, 3066; c) Q. Pei, R. Pelrine, S. Stanford, R. Kornbluh, M. Rosenthal, *Synthetic Metals* **2003**, 135, 129.
- [153] a) E. D'Anna, G. Valle, A. Mazzoni, I. Strauss, F. Iberite, J. Patton, F. M. Petrini, S. Raspopovic, G. Granata, R. Di Iorio, *Science Robotics* **2019**, 4, eaau8892; b) G. Valle, E. D'Anna, I. Strauss, F. Clemente, G. Granata, R. Di Iorio, M. Controzzi, T. Stieglitz, P. M. Rossini, F. M. Petrini, *Frontiers in bioengineering and biotechnology* **2020**, 8, 287; c) L. Zollo, G. Di Pino, A. L. Ciancio, F. Ranieri, F. Cordella, C. Gentile, E. Noce, R. A. Romeo, A. Dellacasa Bellingegni, G. Vadalà, *Science robotics* **2019**, 4, eaau9924.
- [154] a) M. Loeffe, C. M. Schumacher, U. B. Lustenberger, W. J. Stark, *Soft Robotics* **2015**, 2, 33; b) N. W. Bartlett, M. T. Tolley, J. T. Overvelde, J. C. Weaver, B. Mosadegh, K. Bertoldi, G. M. Whitesides, R. J. Wood, *Science* **2015**, 349, 161; c) R. F. Shepherd, A. A. Stokes, J. Freake, J. Barber, P. W. Snyder, A. D. Mazzeo, L. Cademartiri, S. A. Morin, G. M. Whitesides, *Angewandte Chemie International Edition* **2013**, 52, 2892.
- [155] a) C. Pawashe, S. Floyd, M. Sitti, *Applied Physics Letters* **2009**, 94, 164108; b) Z. Ye, S. Régnier, M. Sitti, *IEEE Transactions on Robotics* **2013**, 30, 3; c) J. Kim, S. E. Chung, S.-E. Choi, H. Lee, J. Kim, S. Kwon, *Nature materials* **2011**, 10, 747; d) M. Khoo, C. Liu, *Sensors and Actuators A: Physical* **2001**, 89, 259; e) E. Diller, J. Zhuang, G. Zhan Lum, M. R. Edwards, M. Sitti, *Applied Physics Letters* **2014**, 104, 174101.
- [156] a) J. S. Evans, Y. Sun, B. Senyuk, P. Keller, V. M. Pergamenschik, T. Lee, I. I. Smalyukh, *Physical review letters* **2013**, 110, 187802; b) X. Liu, R. Wei, P. T. Hoang, X. Wang, T. Liu, P. Keller, *Advanced Functional Materials* **2015**, 25, 3022; c) X. Liu,

- X. Wang, T. Liu, P. Keller, *Macromolecules* **2016**, 49, 8322; d) K. Hon, D. Corbett, E. Terentjev, *The European Physical Journal E* **2008**, 25, 83; e) Z. Qin, J. C. Bischof, *Chemical Society Reviews* **2012**, 41, 1191.
- [157] a) Y. Hu, J. Liu, L. Chang, L. Yang, A. Xu, K. Qi, P. Lu, G. Wu, W. Chen, Y. Wu, *Advanced Functional Materials* **2017**, 27, 1704388; b) L. Chen, M. Weng, P. Zhou, L. Zhang, Z. Huang, W. Zhang, *Nanoscale* **2017**, 9, 9825; c) R. Yin, W. Xu, M. Kondo, C.-C. Yen, J.-i. Mamiya, T. Ikeda, Y. Yu, *Journal of Materials Chemistry* **2009**, 19, 3141; d) C. Li, Y. Liu, X. Huang, H. Jiang, *Advanced Functional Materials* **2012**, 22, 5166; e) J. J. Wie, M. R. Shankar, T. J. White, *Nature communications* **2016**, 7, 13260.
- [158] a) E. B. Dolan, C. Varela, K. Mendez, W. Whyte, R. Levey, S. Robinson, E. Maye, J. O'dwyer, R. Beatty, A. Rothman, *Science Robotics* **2019**, 4, eaax7043; b) H. Yang, B. S. Yeow, Z. Li, K. Li, T.-H. Chang, L. Jing, Y. Li, J. S. Ho, H. Ren, P.-Y. Chen, *Science Robotics* **2019**, 4, eaax7020; c) M. Su, R. Xie, Y. Zhang, X. Kang, D. Huang, Y. Guan, H. Zhu, *Applied Sciences* **2019**, 9, 2999.
- [159] a) G. Antonelli, Springer, 2014; b) K. C. Galloway, K. P. Becker, B. Phillips, J. Kirby, S. Licht, D. Tchernov, R. J. Wood, D. F. Gruber, *Soft robotics* **2016**, 3, 23; c) Y. Feng, T. Ide, H. Nabae, G. Endo, R. Sakurai, S. Ohno, K. Suzumori, *Robomech Journal* **2021**, 8, 1.
- [160] a) L. Ionov, *Materials Today* **2014**, 17, 494; b) E. Wang, M. S. Desai, S.-W. Lee, *Nano letters* **2013**, 13, 2826; c) J. C. Breger, C. Yoon, R. Xiao, H. R. Kwag, M. O. Wang, J. P. Fisher, T. D. Nguyen, D. H. Gracias, *ACS applied materials & interfaces* **2015**, 7, 3398; d) V. Magdanz, G. Stoychev, L. Ionov, S. Sanchez, O. G. Schmidt, *Angewandte Chemie* **2014**, 126, 2711; e) H.-W. Huang, M. S. Sakar, A. J. Petruska, S. Pané, B. J. Nelson, *Nature communications* **2016**, 7, 12263.
- [161] a) M. L. Dezaki, M. Bodaghi, A. Serjouei, S. Afazov, A. Zolfagharian, *Sensors and Actuators A: Physical* **2022**, 345, 113779; b) K. E. Wilkes, P. K. Liaw, K. E. Wilkes, *Jom* **2000**, 52, 45; c) J. M. Jani, M. Leary, A. Subic, M. A. Gibson, *Materials & Design (1980-2015)* **2014**, 56, 1078; d) H. Rodrigue, W. Wang, M.-W. Han, T. J. Kim, S.-H. Ahn, *Soft robotics* **2017**, 4, 3; e) W. Wang, J.-Y. Lee, H. Rodrigue, S.-H. Song, W.-S. Chu, S.-H. Ahn, *Bioinspiration & biomimetics* **2014**, 9, 046006.
- [162] a) A. Lendlein, S. Kelch, *Angewandte Chemie International Edition* **2002**, 41, 2034; b) T. Xie, *Polymer* **2011**, 52, 4985; c) C. Liu, H. Qin, P. Mather, *Journal of materials*

- chemistry* **2007**, 17, 1543; d) W. Small IV, P. Singhal, T. S. Wilson, D. J. Maitland, *Journal of materials chemistry* **2010**, 20, 3356; e) L. Ionov, *Soft Matter* **2011**, 7, 6786.
- [163] a) R. S. Kularatne, H. Kim, J. M. Boothby, T. H. Ware, *Journal of Polymer Science Part B: Polymer Physics* **2017**, 55, 395; b) M. O. Saed, E. M. Terentjev, *ACS Macro Letters* **2020**, 9, 749; c) M. Wang, Z.-W. Cheng, B. Zuo, X.-M. Chen, S. Huang, H. Yang, *ACS Macro Letters* **2020**, 9, 860; d) C. Zhu, Y. Lu, L. Jiang, Y. Yu, *Advanced Functional Materials* **2021**, 31, 2009835; e) L. Qin, X. Liu, Y. Yu, *Advanced Optical Materials* **2021**, 9, 2001743.
- [164] a) P. Krusic, E. Wasserman, P. Keizer, J. Morton, K. Preston, *Science* **1991**, 254, 1183; b) E. Nakamura, H. Isobe, *Accounts of chemical research* **2003**, 36, 807; c) L. Xiao, H. Aoshima, Y. Saitoh, N. Miwa, *Free Radical Biology and Medicine* **2011**, 51, 1376; d) V. Chistyakov, Y. O. Smirnova, E. Prazdnova, A. Soldatov, *BioMed Research International* **2013**, 2013.
- [165] a) N. S. Sariciftci, A. J. Heeger, *Fullerenes and Photonics II* **1995**, 2530, 76; b) N. S. Sariciftci, L. Smilowitz, A. Heeger, F. Wudl, *Synthetic Metals* **1993**, 59, 333; c) J. R. Heath, *Metal, semiconductor, and carbon cluster studies including the discovery and characterization of carbon-60: Buckminsterfullerene*, Rice University, **1988**.
- [166] M. Klaiber, A. Tschöpe, K. Cu, I. Waibel, S. Heißler, M. Franzreb, J. Lahann, *ACS Applied Engineering Materials* **2022**.
- [167] a) E. Snow, F. Perkins, E. Houser, S. Badescu, T. Reinecke, *Science* **2005**, 307, 1942; b) Z. Chen, S. M. Tabakman, A. P. Goodwin, M. G. Kattah, D. Daranciang, X. Wang, G. Zhang, X. Li, Z. Liu, P. J. Utz, *Nature biotechnology* **2008**, 26, 1285.
- [168] a) B. Li, B. Gil, M. Power, A. Gao, S. Treratanakulchai, S. Anastasova, G.-Z. Yang, *ACS applied materials & interfaces* **2019**, 11, 35577; b) R. Streicher, in *Carbon Nanotubes*, Jenny Stanford Publishing **2019**, p. 61.
- [169] D. A. Heller, S. Baik, T. E. Eurell, M. S. Strano, *Advanced materials* **2005**, 17, 2793.
- [170] A. De La Zerda, C. Zavaleta, S. Keren, S. Vaithilingam, S. Bodapati, Z. Liu, J. Levi, B. R. Smith, T.-J. Ma, O. Oralkan, *Nature nanotechnology* **2008**, 3, 557.
- [171] C. Lee, X. Wei, J. W. Kysar, J. Hone, *science* **2008**, 321, 385.
- [172] J. S. Bunch, S. S. Verbridge, J. S. Alden, A. M. Van Der Zande, J. M. Parpia, H. G. Craighead, P. L. McEuen, *Nano letters* **2008**, 8, 2458.
- [173] a) A. A. Balandin, S. Ghosh, W. Bao, I. Calizo, D. Teweldebrhan, F. Miao, C. N. Lau, *Nano letters* **2008**, 8, 902; b) D. Ghosh, I. Calizo, D. Teweldebrhan, E. P. Pokatilov,

- D. L. Nika, A. A. Balandin, W. Bao, F. Miao, C. N. Lau, *Applied Physics Letters* **2008**, 92, 151911; c) S. Ghosh, W. Bao, D. L. Nika, S. Subrina, E. P. Pokatilov, C. N. Lau, A. A. Balandin, *Nature materials* **2010**, 9, 555; d) S. Ghosh, D. Nika, E. Pokatilov, A. Balandin, *New Journal of Physics* **2009**, 11, 095012.
- [174] a) A. K. Geim, *science* **2009**, 324, 1530; b) A. K. Geim, K. S. Novoselov, *Nature materials* **2007**, 6, 183.
- [175] A. S. Mayorov, R. V. Gorbachev, S. V. Morozov, L. Britnell, R. Jalil, L. A. Ponomarenko, P. Blake, K. S. Novoselov, K. Watanabe, T. Taniguchi, *Nano letters* **2011**, 11, 2396.
- [176] S. Morozov, K. Novoselov, M. Katsnelson, F. Schedin, D. C. Elias, J. A. Jaszczak, A. Geim, *Physical review letters* **2008**, 100, 016602.
- [177] A. A. Griffith, *Philosophical transactions of the royal society of london. Series A, containing papers of a mathematical or physical character* **1921**, 221, 163.
- [178] Z. Chen, U. Gandhi, J. Lee, R. Wagoner, *Journal of Materials Processing Technology* **2016**, 227, 227.
- [179] K. S. Novoselov, A. K. Geim, S. V. Morozov, D.-e. Jiang, Y. Zhang, S. V. Dubonos, I. V. Grigorieva, A. A. Firsov, *science* **2004**, 306, 666.
- [180] C. R. Dean, A. F. Young, I. Meric, C. Lee, L. Wang, S. Sorgenfrei, K. Watanabe, T. Taniguchi, P. Kim, K. L. Shepard, *Nature nanotechnology* **2010**, 5, 722.
- [181] K. S. Novoselov, V. I. Fal'ko, L. Colombo, P. R. Gellert, M. G. Schwab, K. Kim, *nature* **2012**, 490, 192.
- [182] a) P. Blake, P. D. Brimicombe, R. R. Nair, T. J. Booth, D. Jiang, F. Schedin, L. A. Ponomarenko, S. V. Morozov, H. F. Gleeson, E. W. Hill, *Nano letters* **2008**, 8, 1704; b) Y. Hernandez, V. Nicolosi, M. Lotya, F. M. Blighe, Z. Sun, S. De, I. T. McGovern, B. Holland, M. Byrne, Y. K. Gun'Ko, *Nature nanotechnology* **2008**, 3, 563.
- [183] R. Munoz, C. Gómez-Aleixandre, *Chemical Vapor Deposition* **2013**, 19, 297.
- [184] M. Losurdo, M. M. Giangregorio, P. Capezzuto, G. Bruno, *Physical Chemistry Chemical Physics* **2011**, 13, 20836.
- [185] P. Lenz-Solomun, M.-C. Wu, D. W. Goodman, *Catalysis letters* **1994**, 25, 75.
- [186] Y. Zhang, L. Zhang, C. Zhou, *Accounts of chemical research* **2013**, 46, 2329.
- [187] a) M. Acik, G. Lee, C. Mattevi, M. Chhowalla, K. Cho, Y. Chabal, *Nature materials* **2010**, 9, 840; b) J. T. Robinson, S. M. Tabakman, Y. Liang, H. Wang, H. Sanchez

- Casalongue, D. Vinh, H. Dai, *Journal of the American Chemical Society* **2011**, 133, 6825.
- [188] J. Loomis, B. King, T. Burkhead, P. Xu, N. Bessler, E. Terentjev, B. Panchapakesan, *Nanotechnology* **2012**, 23, 045501.
- [189] a) S.-E. Zhu, R. Shabani, J. Rho, Y. Kim, B. H. Hong, J.-H. Ahn, H. J. Cho, *Nano letters* **2011**, 11, 977; b) J. Liang, L. Huang, N. Li, Y. Huang, Y. Wu, S. Fang, J. Oh, M. Kozlov, Y. Ma, F. Li, *ACS nano* **2012**, 6, 4508.
- [190] a) J.-H. Jung, J.-H. Jeon, V. Sridhar, I.-K. Oh, *Carbon* **2011**, 49, 1279; b) W. Yang, H. Choi, S. Choi, M. Jeon, S.-Y. Lee, *Smart Materials and Structures* **2012**, 21, 055012; c) L. Lu, J. Liu, Y. Hu, Y. Zhang, W. Chen, *Advanced materials* **2013**, 25, 1270.
- [191] a) S. Michel, B. T. Chu, S. Grimm, F. A. Nüesch, A. Borgschulte, D. M. Opris, *Journal of Materials Chemistry* **2012**, 22, 20736; b) U. Kim, J. Kang, C. Lee, H. Y. Kwon, S. Hwang, H. Moon, J. C. Koo, J.-D. Nam, B. H. Hong, J.-B. Choi, *Nanotechnology* **2013**, 24, 145501; c) Z. H. Fang, C. Punckt, E. Y. Leung, H. C. Schniepp, I. A. Aksay, *Applied optics* **2010**, 49, 6689.
- [192] a) K.-Y. Shin, J.-Y. Hong, J. Jang, *Chemical communications* **2011**, 47, 8527; b) S. Xu, B. Man, S. Jiang, C. Chen, C. Yang, M. Liu, X. Gao, Z. Sun, C. Zhang, *Applied Physics Letters* **2013**, 102, 151902; c) S.-H. Bae, O. Kahya, B. K. Sharma, J. Kwon, H. J. Cho, B. Ozyilmaz, J.-H. Ahn, *ACS nano* **2013**, 7, 3130.
- [193] a) L. Staudenmaier, *Berichte der deutschen chemischen Gesellschaft* **1898**, 31, 1481; b) W. S. Hummers Jr, R. E. Offeman, *Journal of the American Chemical Society* **1958**, 80, 1339; c) U. Hofmann, E. König, *Zeitschrift für anorganische und allgemeine Chemie* **1937**, 234, 311; d) B. C. Brodie, *Philosophical transactions of the Royal Society of London* **1859**, 249; e) R. Singh, R. Kumar, D. Singh, 2016.
- [194] J. Sturala, J. Luxa, M. Pumera, Z. Sofer, *Chemistry—A European Journal* **2018**, 24, 5992.
- [195] K. Yang, H. Xu, L. Cheng, C. Sun, J. Wang, Z. Liu, *Advanced materials* **2012**, 24, 5586.
- [196] a) F. Duan, W. Li, G. Wang, C. Weng, H. Jin, H. Zhang, Z. Zhang, *Nano Research* **2019**, 12, 1571; b) X. Huang, F. Liu, P. Jiang, T. Tanaka, presented at 2013 IEEE International Conference on Solid Dielectrics (ICSD) **2013**.

- [197] a) Y. Zhu, S. Murali, W. Cai, X. Li, J. W. Suk, J. R. Potts, R. S. Ruoff, *Advanced materials* **2010**, 22, 3906; b) L. Tian, P. Anilkumar, L. Cao, C. Kong, M. Mezziani, H. Qian, L. Veca, T. Thorne, K. Tackett, P. Sun, *ACS Nano* **2011**, 5, 3052; c) C. Y. Kong, W.-L. Song, M. J. Mezziani, K. N. Tackett II, L. Cao, A. J. Farr, A. Anderson, Y.-P. Sun, *The Journal of Supercritical Fluids* **2012**, 61, 206; d) J. D. Renteria, S. Ramirez, H. Malekpour, B. Alonso, A. Centeno, A. Zurutuza, A. I. Cocemasov, D. L. Nika, A. A. Balandin, *Advanced Functional Materials* **2015**, 25, 4664.
- [198] V. B. Mohan, R. Brown, K. Jayaraman, D. Bhattacharyya, *Materials Science and Engineering: B* **2015**, 193, 49.
- [199] Y. Zeng, T. Li, Y. Yao, T. Li, L. Hu, A. Marconnet, *Advanced Functional Materials* **2019**, 29, 1901388.
- [200] R. Tarcan, O. Todor-Boer, I. Petrovai, C. Leordean, S. Astilean, I. Botiz, *Journal of Materials Chemistry C* **2020**, 8, 1198.
- [201] D. Geng, S. Yang, Y. Zhang, J. Yang, J. Liu, R. Li, T.-K. Sham, X. Sun, S. Ye, S. Knights, *Applied Surface Science* **2011**, 257, 9193.
- [202] A. N. Banerjee, *Interface focus* **2018**, 8, 20170056.
- [203] A. Steier, B. Schmieg, Y. Irtel von Brenndorff, M. Meier, H. Nirschl, M. Franzreb, J. Lahann, *Macromolecular bioscience* **2020**, 20, 2000154.
- [204] a) J. Nie, Z.-l. Wang, J.-f. Li, Y. Gong, J.-x. Sun, S.-g. Yang, *Chinese Journal of Polymer Science* **2017**, 35, 1001; b) L. Meng, W. Klinkajon, P. r. K-hasuwan, S. Harkin, P. Supaphol, G. E. Wnek, *Polymer International* **2015**, 64, 42.
- [205] a) L. F. Gudeman, N. A. Peppas, *Journal of membrane science* **1995**, 107, 239; b) M. Fukushima, K. Tatsumi, S. Wada, *Analytical sciences* **1999**, 15, 1153.
- [206] T. Anirudhan, S. Rejeena, *Chemical engineering journal* **2012**, 187, 150.
- [207] a) W. A. Laftah, S. Hashim, *Journal of Composite Materials* **2014**, 48, 555; b) S. J. Kim, K. J. Lee, S. M. Lee, I. Y. Kim, S. I. Kim, *High Performance Polymers* **2004**, 16, 625.
- [208] A. Covington, R. Robinson, *Analytica Chimica Acta* **1975**, 78, 219.
- [209] S. Korten, N. Albet-Torres, F. Paderi, L. ten Siethoff, S. Diez, T. Korten, G. te Kronnie, A. Månsson, *Lab on a Chip* **2013**, 13, 866.
- [210] a) J. Lahann, W. Plüster, D. Klee, H.-G. Gattner, H. Höcker, *Journal of Materials Science: Materials in Medicine* **2001**, 12, 807; b) H. Nandivada, H. Y. Chen, J. Lahann, *Macromolecular rapid communications* **2005**, 26, 1794.

- [211] a) V. A. Kumar, N. L. Taylor, S. Shi, B. K. Wang, A. A. Jalan, M. K. Kang, N. C. Wickremasinghe, J. D. Hartgerink, *ACS nano* **2015**, 9, 860; b) H. Zhao, J. C. Chappell, *Journal of Biological Engineering* **2019**, 13, 1; c) B. Lalan, Sonal, M. Pomerantseva, Irina, M. Vacanti, Joseph P, *World Journal of Surgery* **2001**, 25, 1458.
- [212] a) R. M. Nerem, D. Seliktar, *Annual review of biomedical engineering* **2001**, 3, 225; b) A. C. Thomas, G. R. Campbell, J. H. Campbell, *Cardiovascular pathology* **2003**, 12, 271.
- [213] a) L. Debbi, B. Zohar, M. Shuhmaher, Y. Shandalov, I. Goldfracht, S. Levenberg, *Biomaterials* **2022**, 280, 121286; b) A. Dellaquila, C. Le Bao, D. Letourneur, T. Simon-Yarza, *Advanced Science* **2021**, 8, 2100798.
- [214] a) J. V. Serbo, S. Gerecht, *Stem cell research & therapy* **2013**, 4, 1; b) J. Rouwkema, A. Khademhosseini, *Trends in biotechnology* **2016**, 34, 733.
- [215] a) G. Gurel Pekozer, N. Abay Akar, A. Cumbul, T. Beyzadeoglu, G. Torun Kose, *ACS Biomaterials Science & Engineering* **2021**, 7, 1526; b) M. A. Traore, S. C. George, *Tissue Engineering Part B: Reviews* **2017**, 23, 505.
- [216] a) M. P. Lutolf, J. Hubbell, *Nature biotechnology* **2005**, 23, 47; b) Y. Li, Y. Xiao, C. Liu, *Chemical reviews* **2017**, 117, 4376; c) J. Vajda, M. Milojević, U. Maver, B. Vihar, *Biomedicines* **2021**, 9, 589.
- [217] a) S. Saberianpour, M. Heidarzadeh, M. H. Geranmayeh, H. Hosseinkhani, R. Rahbarghazi, M. Nouri, *Journal of biological engineering* **2018**, 12, 1; b) L. Boldock, C. Wittkowske, C. M. Perrault, *Microcirculation* **2017**, 24, e12361.
- [218] B. Zohar, L. Debbi, M. Machour, N. Nachum, I. Redenski, M. Epshtein, N. Korin, S. Levenberg, *Acta Biomaterialia* **2022**.
- [219] R. Martinez-Duarte, *Micromachines* **2014**, 5, 766.
- [220] a) P. Dan, É. Velot, V. Decot, P. Menu, *Journal of Cell Science* **2015**, 128, 2415; b) N. F. Jufri, A. Mohamedali, A. Avolio, M. S. Baker, *Vascular cell* **2015**, 7, 1.
- [221] S. S. Sheiko, A. V. Dobrynin, *Macromolecules* **2019**, 52, 7531.
- [222] V. Barron, C. Brougham, K. Coghlan, E. McLucas, D. O'Mahoney, C. Stenson-Cox, P. E. McHugh, *Journal of materials science: Materials in medicine* **2007**, 18, 1973.
- [223] a) C. E. Rupert, T. Y. Kim, B.-R. Choi, K. L. Coulombe, *Stem Cells International* **2020**, 2020; b) C. Bearzi, M. Rota, T. Hosoda, J. Tillmanns, A. Nascimbene, A. De Angelis, S. Yasuzawa-Amano, I. Trofimova, R. W. Siggins, N. LeCapitaine, *Proceedings of the National Academy of Sciences* **2007**, 104, 14068; c) K. R. Sipido,

- T. Stankovicova, W. Flameng, J. Vanhaecke, F. Verdonck, *Cardiovascular research* **1998**, 37, 478.
- [224] M. Potente, H. Gerhardt, P. Carmeliet, *Cell* **2011**, 146, 873.
- [225] R. J. Klebe, K. L. Bentley, R. C. Schoen, *Journal of cellular physiology* **1981**, 109, 481.
- [226] a) N. Agarwal, D. Hoagland, R. Farris, *Journal of Applied Polymer Science* **1997**, 63, 401; b) H. Zhang, J. Magoshi, M. Becker, J. Y. Chen, R. Matsunaga, *Journal of applied polymer science* **2002**, 86, 1817.
- [227] a) S. Chakravarty, B. Gogoi, B. B. Mandal, N. Bhardwaj, N. S. Sarma, *Biosensors and Bioelectronics* **2018**, 112, 18; b) R. Wu, L. Ma, X. Y. Liu, *Advanced Science* **2022**, 9, 2103981; c) X. Dong, Q. Liu, S. Liu, R. Wu, L. Ma, *Advanced Fiber Materials* **2022**, 4, 885; d) W. Qiu, A. Patil, F. Hu, X. Y. Liu, *Small* **2019**, 15, 1903948.
- [228] K. Zhang, F. Si, H. Duan, J. Wang, *Acta biomaterialia* **2010**, 6, 2165.
- [229] a) K. Gellynck, P. C. Verdonk, E. Van Nimmen, K. F. Almqvist, T. Gheysens, G. Schoukens, L. Van Langenhove, P. Kiekens, J. Mertens, G. Verbruggen, *Journal of Materials Science: Materials in Medicine* **2008**, 19, 3399; b) G. H. Altman, R. L. Horan, H. H. Lu, J. Moreau, I. Martin, J. C. Richmond, D. L. Kaplan, *Biomaterials* **2002**, 23, 4131.
- [230] a) S.-W. Ha, A. E. Tonelli, S. M. Hudson, *Biomacromolecules* **2005**, 6, 1722; b) B. Zuo, L. Dai, Z. Wu, *Journal of materials science* **2006**, 41, 3357; c) C. Jiang, X. Wang, R. Gunawidjaja, Y. H. Lin, M. K. Gupta, D. L. Kaplan, R. R. Naik, V. V. Tsukruk, *Advanced functional materials* **2007**, 17, 2229.
- [231] a) E. Lepore, F. Bosia, F. Bonaccorso, M. Bruna, S. Taioli, G. Garberoglio, A. C. Ferrari, N. M. Pugno, *2D Materials* **2017**, 4, 031013; b) K. Hu, M. K. Gupta, D. D. Kulkarni, V. V. Tsukruk, *Advanced Materials* **2013**, 25, 2301.
- [232] a) T. Kong, H. A. Stone, L. Wang, H. C. Shum, *Proceedings of the National Academy of Sciences* **2018**, 115, 6159; b) Z. Wang, Q. Kong, B. Li, J. Tian, K. Yu, J. Wang, *Physics of Fluids* **2022**, 34, 123301; c) J. Lee, S. Moon, Y. B. Han, S. J. Yang, J. Lahann, K. J. Lee, *Macromolecular Rapid Communications* **2022**, 43, 2100560.
- [233] a) R. Oldenbourg, *Cold Spring Harbor Protocols* **2013**, 2013, pdb. top078600; b) I. Founda, M. El-Tonsy, *Journal of materials science* **1990**, 25, 4752.
- [234] N. Sreerama, R. W. Woody, *Protein Science* **2003**, 12, 384.

- [235] S. Lee, S. H. Kim, Y. Y. Jo, W. T. Ju, H. B. Kim, H. Kweon, *ChemistrySelect* **2021**, 6, 1735.
- [236] A. T. Tu, *Principles and Applications* **1982**, 1.
- [237] M. Tsukada, Y. Gotoh, M. Nagura, N. Minoura, N. Kasai, G. Freddi, *Journal of Polymer Science Part B: Polymer Physics* **1994**, 32, 961.
- [238] a) M. C. Duch, G. S. Budinger, Y. T. Liang, S. Soberanes, D. Urich, S. E. Chiarella, L. A. Campochiaro, A. Gonzalez, N. S. Chandel, M. C. Hersam, *Nano letters* **2011**, 11, 5201; b) R. J. Young, I. A. Kinloch, L. Gong, K. S. Novoselov, *Composites Science and Technology* **2012**, 72, 1459.
- [239] W. Gao, L. B. Alemany, L. Ci, P. M. Ajayan, *Nature chemistry* **2009**, 1, 403.
- [240] a) S. Stankovich, D. A. Dikin, R. D. Piner, K. A. Kohlhaas, A. Kleinhammes, Y. Jia, Y. Wu, S. T. Nguyen, R. S. Ruoff, *carbon* **2007**, 45, 1558; b) G. Eda, G. Fanchini, M. Chhowalla, *Nature nanotechnology* **2008**, 3, 270; c) D. Yang, A. Velamakanni, G. Bozoklu, S. Park, M. Stoller, R. D. Piner, S. Stankovich, I. Jung, D. A. Field, C. A. Ventrice Jr, *Carbon* **2009**, 47, 145.
- [241] a) Y. Hernandez, M. Lotya, D. Rickard, S. D. Bergin, J. N. Coleman, *Langmuir* **2010**, 26, 3208; b) S. Park, R. S. Ruoff, *Nature nanotechnology* **2009**, 4, 217.
- [242] a) R. F. Faradilla, G. Lee, J. Roberts, P. Martens, M. Stenzel, J. Arcot, *Cellulose* **2018**, 25, 399; b) M. B. Moghaddam, E. K. Goharshadi, M. H. Entezari, P. Nancarrow, *Chemical engineering journal* **2013**, 231, 365.
- [243] W.-W. Liu, B.-Y. Xia, X.-X. Wang, J.-N. Wang, *Frontiers of Materials Science* **2012**, 6, 176.
- [244] a) M. Pykal, K. r. Šafářová, K. n. Machalová Šišková, P. Jurečka, A. B. Bourlinos, R. Zbořil, M. Otyepka, *The Journal of Physical Chemistry C* **2013**, 117, 11800; b) L. Guardia, M. Fernández-Merino, J. Paredes, P. Solís-Fernández, S. Villar-Rodil, A. Martínez-Alonso, J. Tascón, *Carbon* **2011**, 49, 1653; c) M. Poorsargol, M. Alimohammadian, B. Sohrabi, M. Dehestani, *Applied Surface Science* **2019**, 464, 440; d) M. Lotya, P. J. King, U. Khan, S. De, J. N. Coleman, *ACS nano* **2010**, 4, 3155; e) S. Wang, M. Yi, Z. Shen, *RSC advances* **2016**, 6, 56705.
- [245] S. E. Lebo Jr, J. D. Gargulak, T. J. McNally, *Encyclopedia of Polymer Science and Technology* **2002**, 3.
- [246] S. Zheng, G. Li, W. Yao, T. Yu, *Applied spectroscopy* **1989**, 43, 1269.

- [247] N. Johari, L. Moroni, A. Samadikuchaksaraei, *European Polymer Journal* **2020**, 134, 109842.
- [248] P. Jiang, H. Liu, C. Wang, L. Wu, J. Huang, C. Guo, *Materials letters* **2006**, 60, 919.
- [249] a) J. Yao, H. Masuda, C. Zhao, T. Asakura, *Macromolecules* **2002**, 35, 6; b) C. Wu, S. Egawa, T. Kanno, H. Kurita, Z. Wang, E. Iida, F. Narita, *Materials & Design* **2021**, 202, 109537; c) Z. Zhu, K. Ohgo, T. Asakura, *Express Polym Lett* **2008**, 12, 885.
- [250] a) Q. Wang, C. Wang, M. Zhang, M. Jian, Y. Zhang, *Nano Letters* **2016**, 16, 6695; b) S. Ling, Q. Wang, D. Zhang, Y. Zhang, X. Mu, D. L. Kaplan, M. J. Buehler, *Advanced functional materials* **2018**, 28, 1705291.
- [251] a) J. Pérez-Rigueiro, C. Viney, J. Llorca, M. Elices, *Journal of Applied Polymer Science* **1998**, 70, 2439; b) J. Pérez-Rigueiro, C. Viney, J. Llorca, M. Elices, *Journal of applied polymer science* **2000**, 75, 1270; c) R. Rajkhowa, V. Gupta, V. Kothari, *Journal of applied polymer science* **2000**, 77, 2418; d) L.-D. Koh, Y. Cheng, C.-P. Teng, Y.-W. Khin, X.-J. Loh, S.-Y. Tee, M. Low, E. Ye, H.-D. Yu, Y.-W. Zhang, *Progress in Polymer Science* **2015**, 46, 86.
- [252] M. Tsukada, G. Freddi, M. Nagura, H. Ishikawa, N. Kasai, *Journal of applied polymer science* **1992**, 46, 1945.
- [253] a) Y.-W. Chen, Y.-L. Su, S.-H. Hu, S.-Y. Chen, *Advanced drug delivery reviews* **2016**, 105, 190; b) Y. Li, H. Dong, Y. Li, D. Shi, *International journal of nanomedicine* **2015**, 10, 2451; c) P. Gong, F. Wang, F. Guo, J. Liu, B. Wang, X. Ge, S. Li, J. You, Z. Liu, *Journal of Materials Chemistry B* **2018**, 6, 7926.
- [254] K. F. Mak, L. Ju, F. Wang, T. F. Heinz, *Solid State Communications* **2012**, 152, 1341.
- [255] a) J. Kaltenbach, M. H. Kaltenbach, W. Lyons, *Experimental Cell Research* **1958**, 15, 112; b) L. Björndahl, I. Söderlund, U. Kvist, *Human reproduction* **2003**, 18, 813.
- [256] a) M. I. Cotterell, K. Szpek, J. M. Haywood, J. M. Langridge, *Aerosol Science and Technology* **2020**, 54, 1034; b) B. T. Brem, F. C. Mena Gonzalez, S. R. Meyers, T. C. Bond, M. J. Rood, *Aerosol Science and Technology* **2012**, 46, 178.
- [257] S. K. Khalaf, Q. M. Hassan, C. Emsary, H. Sultan, *Journal of Photochemistry and Photobiology A: Chemistry* **2022**, 427, 113809.
- [258] B. Campagne, A. Courjaud, A. Brun, F. Chaput, J.-P. Boilot, *NONLINEAR OPTICS-READING-* **1999**, 21, 201.

-
- [259] a) C. Yang, Y. Li, Y. Yang, R. Tong, L. He, E. Long, L. Liang, L. Cai, *Journal of Biomedical Nanotechnology* **2018**, 14, 1590; b) B. Zhou, Z. Guo, Z. Lin, L. Zhang, B.-P. Jiang, X.-C. Shen, *Inorganic Chemistry Frontiers* **2019**, 6, 1116.
- [260] X. Yang, C. Valenzuela, X. Zhang, Y. Chen, Y. Yang, L. Wang, W. Feng, *Matter* **2023**.
- [261] a) A. Sionkowska, A. Planecka, *Polymer Degradation and Stability* **2011**, 96, 523; b) S. Kaewpirom, S. Boonsang, *RSC advances* **2020**, 10, 15913.

Supporting Information

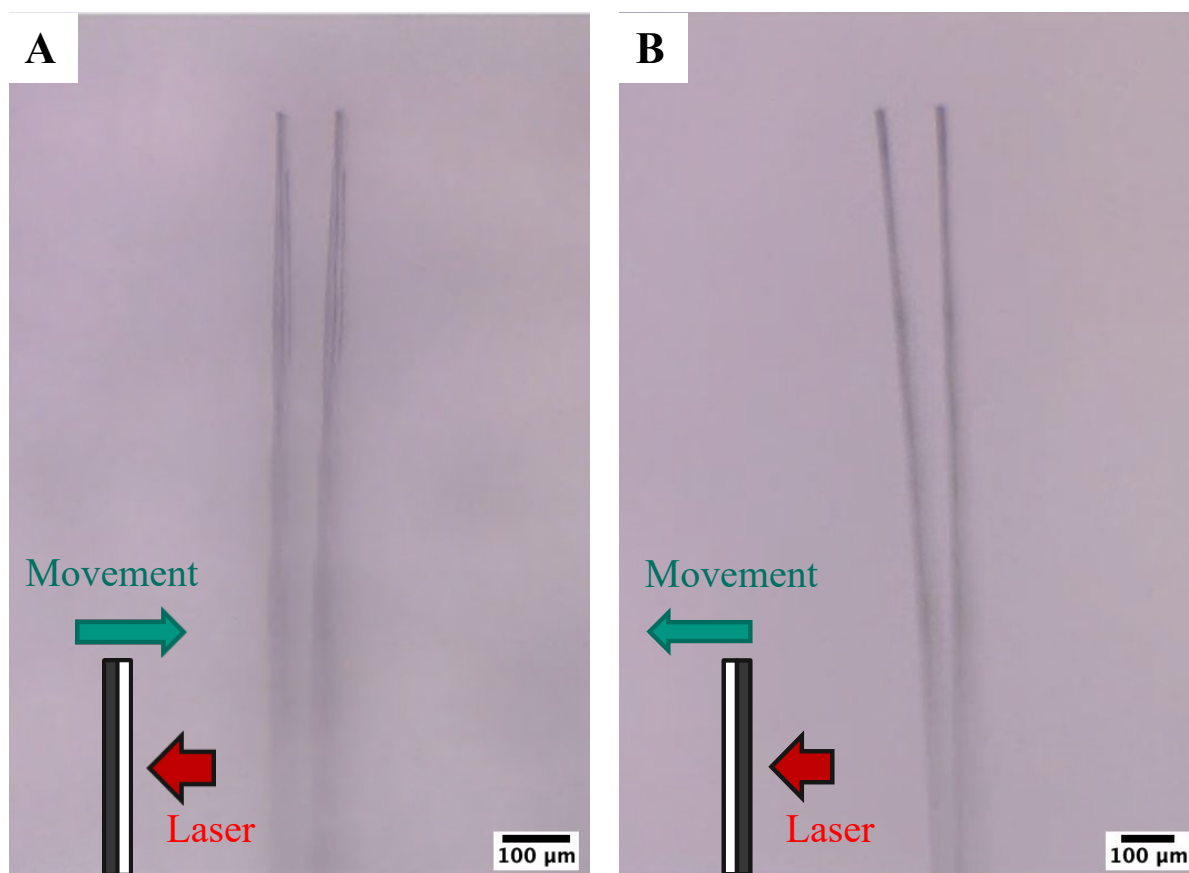


Figure S 1: Expansion of SF-graphene-nigrosine compartment irrespective of irradiated compartment. **A)** Laser irradiation from the right side onto the pristine SF compartment, induces a movement towards the right. **B)** Laser irradiation from the right side onto the SF-graphene-nigrosine compartment, induces a movement towards the left. Scale bars 100 μm .

Publications

Scientific Publications

Klaiber, M., Tschöpe, A., **Cu, K.**, Waibel, I., Heißler, S., Franzreb, M. and Lahann, J., Multifunctional Core–Shell Particle Electrodes for Application in Fluidized Bed Reactors. **ACS Applied Engineering Materials** (2022). DOI: 10.1021/acsaenm.2c00072

Cu, K., Steier, A., Klaiber, M., Franzreb, M., Lahann, J., Directed Particle Transport via Reconfigurable Fiber Networks. **Advanced Functional Materials** (2022). DOI: 10.1002/adfm.202204080

Ukidve, A.*, **Cu, K.***, Kumbhojkar, N.*, Lahann, J. and Mitragotri, S., Overcoming biological barriers to improve solid tumor immunotherapy. **Drug Delivery and Translational Research** (2021). DOI: 10.1007/s13346-021-00923-8

Ukidve, A.*, **Cu, K.***, Goetz, M., Angsantikul, P., Curreri, A., Tanner, E., Lahann, J. and Mitragotri S., Ionic-Liquid-Based Safe Adjuvants. **Advanced Materials** (2020) (*Patent filed*) DOI: 10.1002/adma.202002990

Cu, K., Bansal, R., Mitragotri, S. and Fernandez Rivas, D., Delivery strategies for skin: comparison of nanoliter jets, needles and topical solutions. **Annals of Biomedical Engineering** (2020). DOI: 10.1007/s10439-019-02383-1

Conference Talks

05/2022 **Cu, K.**, Franzreb, M., Lahann, J.:
Biomimetic Microanalytical System for On-Demand Analyte Detection
Materials Research Society (MRS), Honolulu, USA

11/2021 **Cu, K.**, Steier, A., Franzreb, M., Lahann, J.:
Biomimetic Scaffold for Smart Transportation
American Institute of Chemical Engineering (AIChE), Boston, USA

Poster

02/2023 **Cu, K.**, Klaiber, M., Franzreb, M., Lahann, J.:
Directed Particle Transport via Reconfigurable Fiber Networks.
Macromolecular Colloquium Freiburg (MAKRO 2023), Freiburg, Germany

09/2022 **Cu, K.**, Klaiber, M., Franzreb, M., Lahann, J.:
Directed Particle Transport via Reconfigurable Fiber Networks.
Materials Science and Engineering (MSE) Congress, Darmstadt, Germany